November 2017

ASSEMBLY OF PARTICLES ONTO RIGID CYLINDERS AND FLEXIBLE MEMBRANES: PROBING EFFECTS OF SURFACE CURVATURE AND DEFORMATION

Derek Wood

ASSEMBLY OF PARTICLES ONTO RIGID CYLINDERS AND FLEXIBLE MEMBRANES: PROBING EFFECTS OF SURFACE CURVATURE AND DEFORMATION

A Dissertation Presented

by

DEREK A. WOOD

Submitted to the Graduate School of the
University of Massachusetts Amherst in partial fulfillment
of the requirements for the degree of

DOCTOR OF PHILOSOPHY

September 2017

Department of Physics

ASSEMBLY OF PARTICLES ONTO RIGID CYLINDERS AND FLEXIBLE MEMBRANES: PROBING EFFECTS OF SURFACE CURVATURE AND DEFORMATION

A Dissertation Presented

by

DEREK A. WOOD

Approved as to style and content by:

_____
Anthony D. Dinsmore, Chair

_____
Christian D. Santangelo, Member

_____
Jennifer L. Ross, Member

_____
Vincent M. Rotello, Member

_____
Rory Miskimen, Department Head
Department of Physics

ACKNOWLEDGMENTS

I would like to thank my advisor, Tony Dinsmore, for his years of mentorship, guidance, patience, and thoughtful advice. I couldn't have hoped for a better or more supportful advisor, and I surely would not be where I am today without him. I would also like to thank my committee members, Chris Santangelo, Jennifer Ross, and Vince Rotello for their helpful discussions and continual input throughout my time as a graduate student.

Additionally, I would like to thank my peers Jaime Hutchison for her help and training with lipid bilayer membranes, and Ian Torres for his steadfast experimental work helping to understand properties bilayers and vesicle gels. I also thank Arash Manafirad and Sarah Zuraw for thoughtful discussions on membrane mechanics.

Finally, I would like to thank my friends and family for their support during my time as a graduate student. Namely, I would like to thank my wife Caitlin for her constant love and encouragement (and proofreading), without whom I never would have been able to keep it all together and finish. This work is dedicated to my parents, Todd and Nancy Wood.

ABSTRACT

THE ASSEMBLY AND ELASTICITY OF CYLINDRICAL CRYSTALS, AND THE EFFECTS OF NANOPTTICLE ADHESION ON A BILAYER MEMBRANE

SEPTEMBER 2017

DEREK A. WOOD, B.A., STATE UNIVERSITY OF NEW YORK AT GENESEO
Ph.D., UNIVERSITY OF MASSACHUSETTS AMHERST

Directed by: Professor Anthony D. Dinsmore

In this thesis we explore two specific topics within the broad field of particle adhesion. First, we examine the effect of substrate shape and geometry on the self assembly of adsorbed particles, by performing molecular dynamics simulations of interacting particles constrained to the surface of cylinders of varying diameters. We find the diameter of the cylinder imposes a constraint on the shape and crystallographic orientation of the self-assembled lattice, essentially determining the optimal arrangement of particles *a priori*. We propose a simple one-dimensional model to explain the optimal arrangement of particles as a function of the particle interaction potential and the physical size of the constraining cylinder. We next investigate the stiffness of these cylindrical lattices, and find that thin cylindrical crystals are anomalously softer than large ones. We then propose this effect is a consequence of the geometric arrangement of particles in a tight cylindrical shape, and quantify how the stiffness depends on the circumference of the cylinder and on the strength of interaction between the particles.

Second, we explore how adhesion of particles can reshape the substrate, for the purpose of designing novel functional materials. We perform experiments exposing cationic nanoparticles to lipid bilayer vesicles, where we vary the adhesion energy

between the two by adjusting the fraction of anionic lipid (DOPS) in the otherwise zwitterionic lipid (DOPC) bilayer membrane. We find two distinct types of behavior: when the DOPS content of the membrane is 5% or higher, the high adhesion energy causes the nanoparticles to disrupt the vesicles upon adsorption. When the DOPS content is 4% or less, the adhesion of nanoparticles caused the vesicles to adhere to one another and form a rigid liposome gel. We propose that these two behaviors are explained by a transition from a partial wrapping of the nanoparticles to their complete envelopment by the membrane when the DOPS content exceeds 4.5%. We also detail methods for producing large quantities of the vesicle gel using cationic polymers in place of the nanoparticles. These findings could be used to to engineer new solid, semi-permeable materials that can encapsulate cargo, or to create cargo-carrying liposomes with the ability to rupture on trigger.

TABLE OF CONTENTS

Page

LIST OF TABLES

Table Page

LIST OF FIGURES

Figure Page

CHAPTER 1

SPHERICAL PARTICLES BOUND TO SURFACES

When spherical particles bind onto surfaces, it results in a wide range of structures and properties depending on the geometry of the surface and on the interactions between the particles and the surface. In this thesis, we explore two particular facets of this extremely broad topic; the effect of surface shape on the structure and mechanics of particles bound to a rigid surface, and the effect of the strength of particle-surface interactions between rigid particles and a deformable surface.

In part I of this thesis, we explore the case of a rigid surface with a cylindrical shape, which is coated by a monolayer of spheres. In this case, the requirement that a crystal lattice be invariant under a full axial rotation (i.e., that it be commensurate with the substrate circumference) leads to a variety of structures distinct from those found on planar surfaces. The shapes of these crystalline structures were found to depend robustly on the ratio of physical sizes of the cylinder and the bound particles and on the range of the interaction potential. We next explore how these different structures affect the overall bending elasticity of the nanoparticle lattice. These studies utilize simulations to collect results across a wide region of parameter space; intuitive models are proposed that explain our results.

Outcomes of this study include an explanation of the known result that the bending stiffness of a single-wall carbon nanotube is dependent on its diameter,[1-7] and a proposed explanation of the pronounced nonlinear bending response of microtubules.[8-13]

In part II of this thesis, we explore the case of a flexible surface that is initially spherical, in which the particle binding deforms the flexible surface and influences the interactions between nearby bound particles, leading to some surprising and dramatic shape evolution. These studies utilize experiments with lipid bilayers and cationic gold nanoparticles, where the strength of the electrostatic interaction between the two is controlled by adjusting the composition of the lipid bilayer. We find that the shape evolution of the bilayer can be reliably controlled by adjusting this single parameter.

One outcome of these studies is that we learn the 'design rules' for making responsive materials out of vesicles: the spheres are effective at disrupting the surface if the binding energy is strong enough, whereas polymers or weakly-bound spheres do not appreciably deform the surface and instead lead to adhesion between nearby bilayers.

Cylindrical crystals: packing and mechanics

Understanding self-assembly

Self-assembly of a crystal lattice confined to a curved surface exhibits a variety of interesting behaviors that are quite different from the behaviors that arise when it is confined to a planar surface. These differences are a product of the curvature and topology of the surface itself, and appear even at zero temperature.[14] In the case of a cylindrical surface, the requirement that the size of the crystal lattice be commensurate with the substrate circumference leads to a variety of crystalline and non-crystalline structures that are distinct from those found on planar surfaces.

The potential for surface shape and size to affect the lattice structure may be relevant in biological or technological examples of self-assembly such as coating the

surface of fibers, the arrangement of kernels on a corncob,[15] assembly of proteins on membrane tubules,[16] growth of bacterial cell walls,[17] proteins or DNA on microtubules,[18] surfactants on a nanometer-scale cylinder,[19] or proteins around RNA as in helical viral capsids [20].

Previous works have used computer simulations to find the densest packing of hard spheres *inside* a cylinder; these studies found that uniform hexagonal crystals are found only for a discrete set of cylinder radii, between which the spheres form structures with a chiral seam (referred to as a 'line-slip' by Mughal *et al*., Figure 1).[21-24] Experimentally, interior packing has been investigated through soft colloidal spheres confined to cylindrical channels[25] or rigid colloid spheres in rectilinear channels[26], and fullerene nanospheres confined within carbon nanotubes.[27]

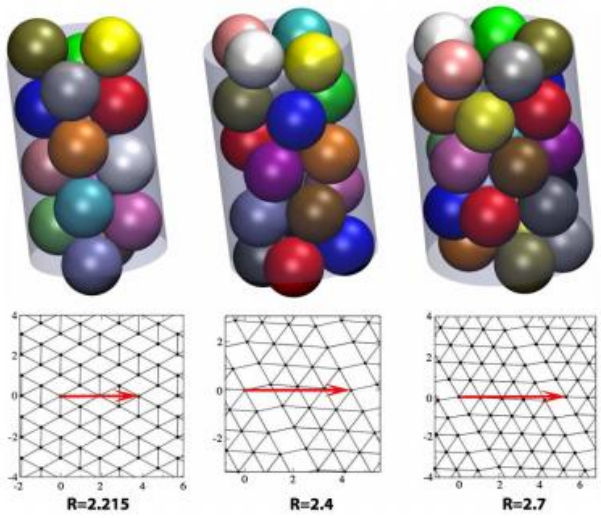

Figure 1. Densest packings of spheres inside a cylinder. The optimal packing structure changes with increasing tube circumference. An image of the overall lattice structure (mapped onto a 2D Surface) is provided below each rendering of the packed tube; a 'line slip' seam is visible in each. Image reproduced from (Mughal *et al.*, 2011).[22]

Confinement to the *surface* of a cylinder, on the other hand, has received comparatively little attention. Mughal et. al make a link between surface packing and interior packing, and predict the maximal packing structures formed by hard spheres on a cylinder.[22,23] However, a maximally packed structure is akin to a system of hard-sphere particles at infinite pressure, which is of limited use in predicting self-assembly. Other authors report on assembly of purely repulsive particles[28-30] or more complex systems with competing species of oppositely charged particles.[18,31] While these studies demonstrate a wide array of possible phases, they leave open the question of assembly of particles with a common class of interaction potential.

Mechanical properties of a cylindrical crystal

In addition to understanding the lattice structure of cylindrical crystals, we also seek to understand how their structure affects their mechanical stiffness. Particularly, many highly-studied and enormously useful objects—such as microtubules and carbon or boron-nitride nanotubes—share the same basic geometric shape of a hollow cylindrical tube. Understanding the physics of crystal cylinders (especially in a very general sense) would help us to build a foundation on which to understand the mechanics of these objects.

To give more direct context to this study, we now explicitly describe the shape, geometry, and mechanics of a few such cylindrical objects (Figure 2). First, a microtubule is a hollow tubular polymer found throughout biological cells; they are involved in maintaining the structure of the cell, and are also implicated in a number of critical biological processes (Figure 2a). Structurally, microtubules are composed of a

repeating chiral lattice of polymerized tubulin dimers, with a single unbroken seam that runs the length of the microtubule and resembles a scar.[32] In eukaryotic cells they have a typical circumference of about 120 nm,[33] containing 13 tubulin subunits repeating around its circumference (microtubules with as low as 11 and as high as 16 subunits have also been reported, though with much lower frequency).[33] The individual tubulin dimers have a diameter of about 10 nm. Some bacterial cells also contain similar microtubules, with a much smaller circumference of about 50 nm and containing only 5 tubulin subunits.[34]

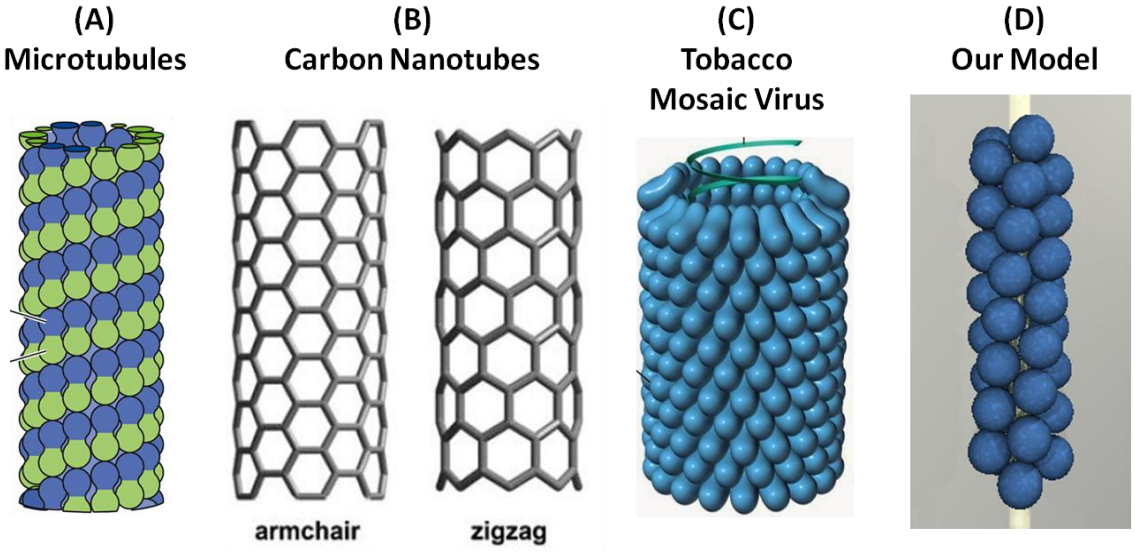

Figure 2. Illustrations of various cylindrical crystals. (A) Structure of a microtubule. Image reproduced from *The Cell*, 4th Edition.[35] (B) Structure of carbon nanotubes, with the "armchair' configuration (left) and the 'zigzag' configuration (right). Image reproduced from (Roham *et al.*, 2014).[36] (C) Structure of the *tobacco mosaic* virus. Image reproduced from (Carsten *et al.*, 2007).[37] (D) Basic structure of our minimalist model.

To our knowledge, a detailed study of the rigidity of a microtubule as a function of its diameter has not been undertaken, nor has the stiffness of bacterial microtubules yet been measured. However, it has previously been noted that the stiffness of a microtubule is dramatically reduced under a large compressive load.[8-13] A rigorous understanding of

this phenomenon has not been established. With our simulations, we would like to develop a better understanding of the way the structure of the microtubule could be connected to its mechanical properties and its function.

A carbon nanotube has a structure that is very different from the structure of a microtubule; a honeycomb lattice of individual carbon atoms. Carbon and boron-nitride nanotubes are routinely fabricated with a variety of different configurations and diameters, and their stiffness has been very accurately mapped out as a function of both of these parameters (Figure 3).

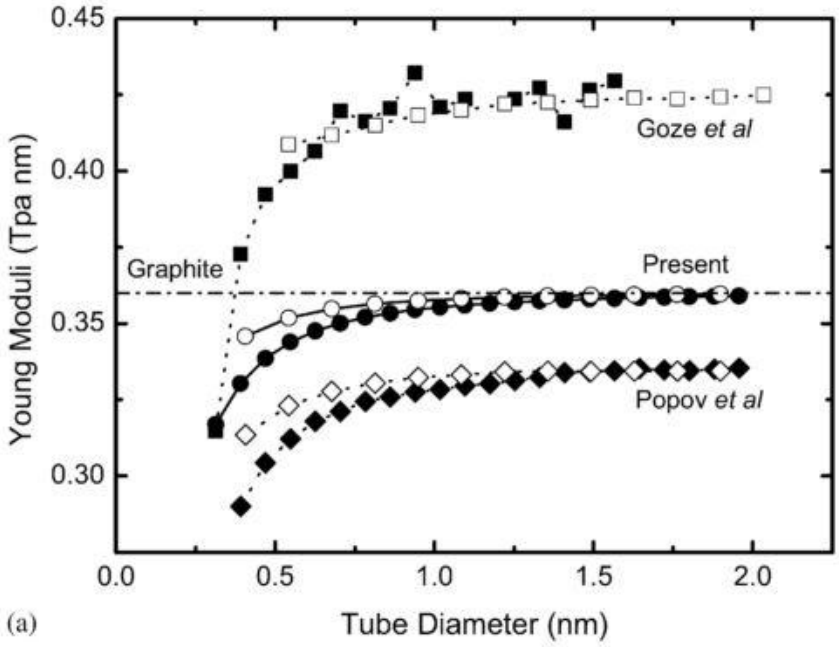

Figure 3. Stiffness of carbon nanotubes as a function of diameter and lattice structure. The open symbols represent 'armchair' lattices and the closed symbols represent 'zigzag' lattices. The data from three separate studies are included. Image reproduced from (Chang *et al.*, 2003).[2]

Interestingly, this stiffness exhibits a clear dependence on the diameter of the nanotube; nanotubes with a smaller diameter are easier to stretch and bend, whereas nanotubes with a very large diameter behave identically to graphene.[1-7] However, Young's modulus is an intrinsic property of a particular material, and in principle ought not to depend on the physical size of the object. A purely continuum mechanical analysis would suggest that the stiffness of any nanotube ought to be identical to the stiffness of a graphene sheet.[38] Furthermore, although the small-diameter softening phenomenon has been reported in many papers,[1-7] the physical origin of the softening has not yet been investigated. We explicitly address this result with our simulation data, and provide a potential explanation for the behavior using a simple geometric argument.

Our Approach

In order to understand the physical rules that govern the shape and structure of a cylindrical crystal, we first set out to understand the related problem of self-assembly of spherical particles confined to a cylindrical geometry. By using simulations to find steady-state, minimal-energy configurations of particles pinned to a cylindrical surface, we were able to explore the phase-space of crystalline structures one might expect to form in a real-world environment.

We next used simulations to study how the structure of a cylindrical lattice impacts its elasticity, especially within the context of the lattice structures identified by our self-assembly simulations above. Of particular interest was identifying how our results might inform an understanding of the stiffness (quantified by Young's modulus) of physical tubular objects, such as the ones detailed in Figure 2a-c.

In order to build as complete an understanding of cylindrical crystals as possible, we used a highly reductionist approach in our investigations; in both cases our model for a crystal cylinder consisted only of a collection of independent spherical particles with isotropically attractive pair-wise interactions, that are constrained to a rigid cylindrical surface (illustrated in Figure 2d). Although in principle carbon nanotubes and microtubules are complex objects with anisotropic interactions, reducing them to such a simplified model may reveal common underlying principles at work.

Our specific approach to this problem was twofold. Firstly, we created a framework using molecular dynamics (MD) simulations in order to determine the range and variety of stable lattices and structures that can self-assemble in a cylindrical geometry. Second, building off of these findings, we created an additional set of simulations to compute the elasticity of each of the different identified structures. From these results, we were able to examine how the shape of the lattice and the interactions between its constituent subunits determine the overall stiffness of the cylinder. Accomplishing these tasks required the reduction of large volumes of data in order to identify important trends, which was then used to develop intuitive and simple models to successfully explain our results.

Lipid bilayer membranes: a novel platform for functional materials

A lipid bilayer membrane is a highly responsive, elastic surface. Our goal is to find new ways to use charged nanoparticles to reshape a membrane surface for the design of novel, functional materials.

The membrane is formed by two parallel sheets of lipid molecules (Figure 4b). Lipid molecules are ampiphilic, having a polar, hydrophilic headgroup and a fatty, nonpolar hydrophobic tail (Figure 4c-d). Within each sheet, the lipids are oriented such that the hydrophilic heads face towards the surrounding water, essentially forming two layers of a smectic liquid crystal. The membrane itself can be formed into a thin closed shell, known as a vesicle. The membrane is about 5 nm thick (depending on its composition), and the diameter of a vesicle can range from 20 nm to over 200 μm.[39] Vesicles between 50 and 500 nm and having a single lamella are referred to as large unilamellar vesicles (LUVs), and vesicles larger than 50 μm are referred to as giant unilamellar vesicles (GUVs). An example image of GUVs is shown in Figure 4a. Multilamellar vesicles are often formed at the same time.

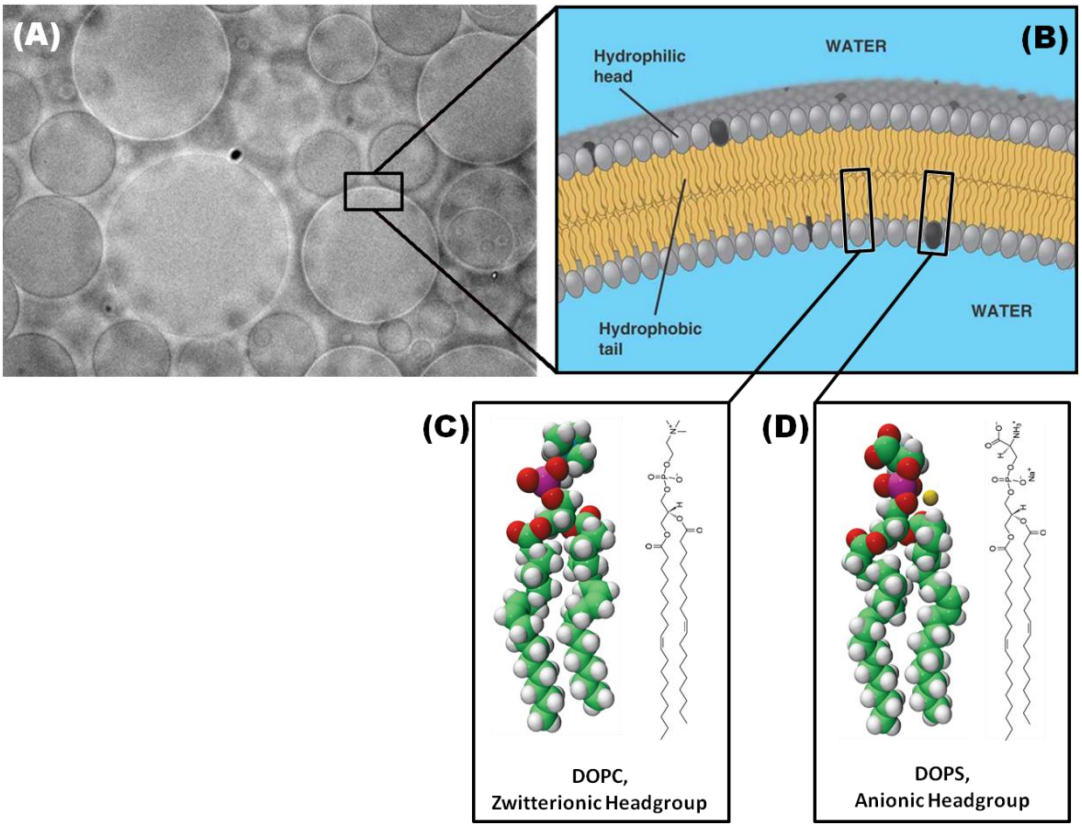

Figure 4. Schematic of vesicle. (A) Microscope image of giant unilamellar vesicles (GUVs) in suspension. These vesicles are composed of 96% DOPC and 4% DOPS by mole fraction. (B) Close-up of a lipid bilayer membrane, illustrating the composition and arrangement of the lipids. The dark gray lipids represent DOPS, and the light gray lipids represent DOPC. Image adapted from *Bio1151.nicerweb.com*. (C) Structure of a single DOPC lipid molecule. Image reproduced from *Avantilipids.com*. (D) Structure of a single DOPS lipid molecule. Image reproduced from *Avantilipids.com*.

The lipid content of a vesicle largely determines its properties; different lipid species can have a different surface charge, preferred curvature, hydrophobicity, affinity for other lipids, and so on. Once formed into a vesicle, these factors contribute to properties such as the vesicle's overall shape, its stiffness, and its stability.[39-41] Biological membranes—such as the cell wall—are typically composed of tens of different lipid species that interact to perform a myriad of biological functions.[42]

Crucially, many of these functions involve dramatically altering the shape or structure of the cell membrane surface on command. These processes include the ability to form long slender filipodi protrusions for cell mobility,[43] the opening of pores for transmission of fluids and ions,[44] or the engulfment and internalization of solid materials through the process of phagocytosis.[45] With our experiments, we seek to mimic this type of functionality.

On-demand reshaping of a membrane surface

We now examine different methods for manipulating the shape of a bilayer membrane; of special interest to us is the ability to selectively and locally tune membrane curvature through surface adhesion of charged proteins or particles. Biologically, processes that reshape the membrane are mostly mediated by the selective binding of specific proteins, such as the proteins in the BAR family. These proteins are capable of

sensing curvature by binding preferentially to curved membranes,[46] as well as altering existing membrane curvature upon adhesion by forcing the membrane to conform to its curved shape.[47] However, the precise nature of many of these interactions are highly nuanced and not yet fully understood.

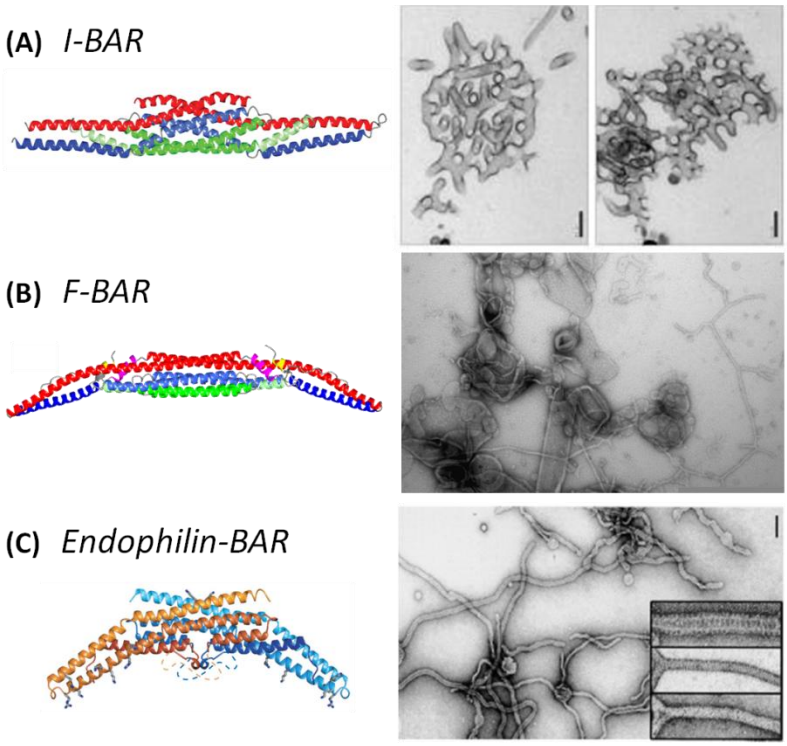

Figure 5. Reshaping of a spherical vesicle caused by adhesion of different proteins, each of which belong to the BAR family of proteins. Images are not to the same scale. (A) Adhesion of I-BAR causes the membrane to assume a saddle-shaped curvature. Image reproduced from (Mattila *et al*., 2007).[48] (B) Adhesion of F-BAR causes the membrane to form tubules. Image reproduced from (Henne *et al*., 2007).[49] (C) Adhesion of Endophilin-BAR causes the membrane to form tubules. Image reproduced from (Farsad *et al*., 2001).[50] Protein renderings reproduced from (endocytosis.org).

The microscope images of the experiments pictured in Figure 5 illustrate the reshaping of a membrane by the adhesion of different species of BAR proteins. In all three cases, the type of deformation imposed on the surface of the membrane is directly

correlated with the shape and curvature of the adhered protein. The convexly shaped I-BAR imposes a negative curvature on the membrane, creating tubules that are directed into the vesicle.[48] The banana-shaped F-BAR imposes a positive curvature on the membrane, leading to formation of approximately 100 nm diameter tubules protruding outwards from the membrane surface.[49,51,52] And, the tightly curved Endophilin-BAR creates smaller 20 nm diameter tubules on the membrane.[50]

Although each of these protein-induced deformations is correlated to the physical shape of the protein, the electrostatics underlying their interactions with the membrane are quite complex. In fact, there are several completely different proposed mechanisms through which the proteins create curvature in the membrane through adhesion.[47] Designing a protein that could interact with a particular species of lipid membrane to produce a particular shape of deformation is still a prohibitively difficult task. Nanoparticles, on the other hand, can be readily fabricated in a laboratory to have a wide range of sizes, shapes, or surface chemistries desired. We therefore focus our efforts to reproducing the kind of membrane reshaping ability found in nature, using nanoparticles as a platform for achieving more customizable results.

Early results in this field have been very encouraging, and both theoretical and experimental work has shown that adhesion of spherical nanoparticles on the interior wall of a GUV can cause tubulation of the vesicle (Figure 6).

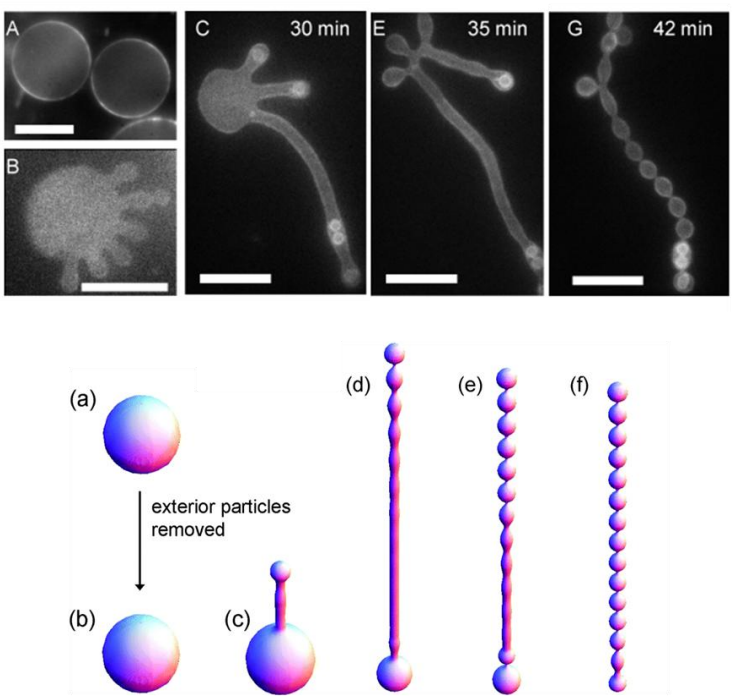

Figure 6. Tubulation caused by adhesion of charged spheres on the interior of a vesicle. *Top row:* DOPC vesicles are formed with 200 nm nanoparticles with a cationic aliphatic amine surface chemistry in the interior volume, causing a surface instability and leading to formation of ~5 μm diameter tubules. Image reproduced from (Yu *et al*., 2009).[53] *Bottom row:* Simulations of particles adhered to an interior membrane surface indicating similar results. Image reproduced from (Yu-Cheng *et al*., 2015)[54].

Experimental work by Y. Yu *et al.* has demonstrated the tubulation of vesicles by nanoparticles (Figure 6, top).[53] In these experiments, vesicles were formed *via* gentle hydration (the protocol for which is detailed in Chapter 6) in a solution containing cationic nanoparticles with a 200 nm diameter, so that nanoparticles were suspended in both the interior and exterior of the GUVs. After formation, the GUVs were centrifuged at high speeds, and the sedimented GUVs were extracted and then re-suspended in a nanoparticle-free, osmotically-matched solution. This effectively removed the nanoparticles from the exterior volume. Interestingly, as soon as the GUVs were re-suspended, they began to develop large tubular protusions—despite the fact that the

vesicles had been in suspension with nanoparticles for a full 24 hours during their formation. The physical mechanism they propose for this behavior is that adhered nanoparticles locally increase the spontaneous curvature of the surrounding lipid molecules, leading to a surface instability. This prediction was tested directly via simulations (Figure 6, bottom), finding similar results.[54] At the very least, the capacity for spherical particles to cause a shape transition in a vesicle through adhesion is effectively demonstrated.

Furthermore, a great deal has been demonstrated about the myriad variety of deformations that can be caused by nanoparticles interacting with membranes. Depending on the type of nanoparticles and the lipid composition of the vesicles, studies have observed a number of different phenomena caused by interactions between particles adsorbed onto a membrane surface, including aggregation into hexagonal clusters,[55,56] linear chain-like formations,[55,57] clustered dimple-like structures,[58,59] and budding of the membrane[60]. A large number of studies have also shown that adsorbed particles can be completely engulfed by a lipid bilayer, in a process that strongly resembles the biological process of endocytosis.[45,61-64] Other work has shown that nanoparticle adhesion can build additional functionality into GUVs as well, including the ability to selectively lyse and release cargo through UV light-induced heating of adsorbed particles.[65]

Interactions between a nanoparticle and a bilayer membrane

To better understand how surface adhesion of many particles can collectively affect the shape of a membrane, we now seek to quantify how a single particle interacts with such a surface. When a charged particle adsorbs onto an oppositely charged

membrane, the two surfaces can reduce electrostatic energy by maximizing the area of contact with one another. To accomplish this, the flexible membrane must deform itself to match the shape of the rigid, curved surface of the colloid particle. This high-curvature deformation by the membrane is energetically costly, and it leads to an energetic competition that ultimately dictates the equilibrium shape of the particle bound to the membrane surface.

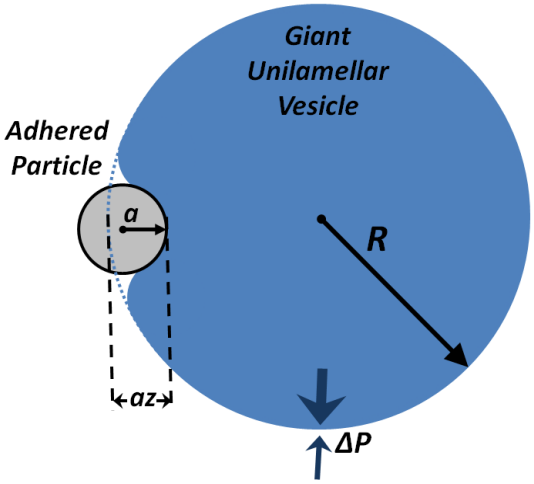

Figure 7. Deformation of a vesicle by surface adhesion of a spherical particle. *R* is the radius of the vesicle, *a* is the radius of the particle, *z* is the amount of penetration of the particle beneath the vesicle surface, and Δ*P* is the osmotic pressure across the membrane.

The exact shape that the membrane assumes is particularly difficult to predict theoretically; it depends nontrivially on many different parameters, including the membrane stretching energy,[66,67] the membrane bending stiffness,[66,67] the ambient temperature k_BT,[55] the surface tension of the membrane,[41] the contact energy between the colloid particle and the membrane surface,[66,67] the rigidity of the colloid particle,[64] the local curvature of the membrane surface,[67,68] the surface shape of the colloid particle,[69,70] the overall volume of the colloid particle,[63] the spontaneous curvature of the

membrane,[66] and how much the spontaneous curvature of the membrane is locally disturbed by the adhesion of the colloid particle.[71,72] (Even still, this may be an incomplete list.)

Despite the inherent complexity, the deformation caused by a single adhered particle can be approximately modeled as the result of a small number of energetic contributions that make the major contributions to the energy (the following analysis is based loosely on calculations made by Deserno *et al*[66]). To do so, we introduce *a* as the diameter of the particle and *z* as the fractional amount of penetration of the particle into the membrane (Figure 7). First, the total contact energy between the membrane and a single particle is

$$E_{contact} = -(2\pi a^2 z)\omega, \quad \text{(Eq. 1)}$$

where ω is the contact energy density between the surfaces. The value of ω depends on the charge densities of the nanoparticle and the lipids or other kinds of interactions, such as van der Waals or specific lock-and-key interactions. Next, the energetic cost required to bend the membrane to meet the tightly curved surface of the particle is

$$E_{bending} = (4\pi z)\kappa, \quad \text{(Eq. 2)}$$

where κ is the bending stiffness of the bilayer, again determined by the lipids composing the bilayer. Finally, the energy required to stretch the membrane and create enough surface area to partially wrap the particle is

$$E_{stretching} = (\pi a^2 z^2)\sigma, \quad \text{(Eq. 3)}$$

where σ is the lateral tension in the membrane. The approximate total energy of the resulting structure is the sum of these three contributions, and hence the equilibrium

penetration of the particle is the value of *z* that minimizes this sum. Combining equations 1, 2 and 3 and minimizing, we find that this equilibrium position is

$$z_{eq} = \frac{\omega a^2 - 2\kappa}{\sigma a^2}. \quad \text{(Eq. 4)}$$

This analysis excludes the deformed area of membrane not in contact with the nanoparticle, however the shape of the membrane surrounding the particle can be assumed to be a smooth wrapping similar to the shape in Figure 7.

We can make a few observations about the nature of nanoparticle adhesion using Equation 4 as a starting point. Assuming σ, κ and ω are constant values, it is energetically favorable for the particle to be fully enveloped by the bilayer (which by our definition, is when $z_{eq} = 2$) if

$$a \geq \sqrt{\frac{2\kappa}{\omega - 2\sigma}}; \quad \text{(Eq. 5)}$$

this is the minimum particle diameter necessary for envelopment to occur.[62] Formally, other factors such as the shape[69] and stiffness[64] of the particle also play a role in determining whether or not envelopment is possible, but in general the above requirement serves as a useful framework that could be adapted to account for the other cases.

Additionally, this line of reasoning also suggests that *any* adhesion at all (i.e., $z_{eq} \geq 0$) is possible only if

$$\sqrt{\frac{2\kappa}{\omega}} \leq a. \quad \text{(Eq. 6)}$$

Together, Equations 5 and 6 show that larger particles should bind to and deform membrane surfaces more easily than very small ones. This is largely due to the large energetic cost involved with bending the lipid bilayer to conform to a high-curvature surface.

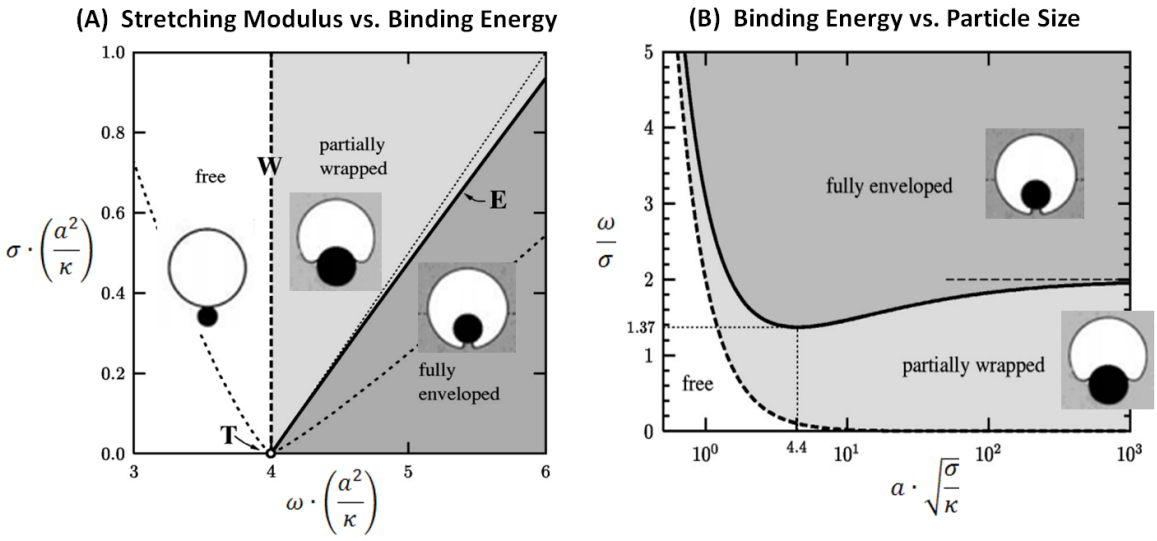

Figure 8. (A) Particle wrapping phase diagram as a function of stretching modulus, σ, and binding energy density, ω. (B) Particle wrapping phase diagram as a function of the effective binding energy, ω/σ, and the particle radius, *a*. Both of these plots are reproduced from (Deserno *et al.*, 2004).[66,73] The membrane/nanoparticle sketches have been inserted for visual context; these calculations did not explicitly include the energetic contributions from the area of the membrane not in contact with the nanoparticle.

The phenomena demonstrated by Equations 5 and 6 were fleshed out with greater accuracy by Deserno *et al.*,[66,73] and a complete phase diagram of particle-wrapping as a function of the important parameters of the problem is illustrated in Figure 8. As these plots demonstrate, the degree of wrapping by a particular lipid bilayer can be increased by using larger or more strongly charged nanoparticles.

When more than one particle adsorbs onto the same membrane, the surface deformations cased by nearby particles overlap one another, leading to interactions between the particles. Although in principle many-body forces contribute heavily to these interactions,[67] we can approximately calculate steady state structures of groups of these particles using the above method. Therefore, for any particular combination of nanoparticles and membranes, the possible 'zoo' of surface structures and deformations

ought to be calculable. This makes it a very exciting platform for study; by tailoring any number of the myriad properties which dictate how the particles interact with the membrane, we can potentially guide assembly into a wide range of possible morphologies. However, there is a great deal that is still not well understood in this field, as well as a lot of gaps in our current knowledge. Experimental data is desperately needed in order to validate (or even merely to examine) the myriad phenomena predicted by the current theory. In particular, we need an experimental system that is reproducible, that has well-defined surface chemistry and tunable interactions.

Our approach

With these experiments, our goal was to form a better understanding of how the diameter and the adhesion strength of adsorbed particles affect the morphology and shape of a bilayer membrane. To accomplish this, we performed experiments exposing a bilayer membrane to particles of different sizes. Additionally, we incrementally adjusted the composition of our membrane to tune the strength of interaction with the particles. Through these experiments, we carefully documented how these two parameters can affect the membrane system.

We also performed experiments intended to quantitatively determine the adhesion energy between a single adsorbed particle and the lipid bilayer membranes used in our experiments. However, these experiments were largely unsuccessful due to the complex nature of the interactions between the nanoparticles and the membrane. This work is described in the Appendix chapter at the end of this manuscript.

Notes

[1] P. A. B. I. Yakobson, Carbon Nanotubes, Topics Appl. Phys **80,** 287 (2001).
[2] T. Chang and H. Gao, Journal of the Mechanics and Physics of Solids **51,** 1059 (2003).
[3] E. Hernández, C. Goze, P. Bernier, and A. Rubio, Applied Physics A **68,** 287 (1999).
[4] L. Jiang and W. Guo, Journal of the Mechanics and Physics of Solids **59,** 1204 (2011).
[5] C. Li and T.-W. Chou, International Journal of Solids and Structures **40,** 2487 (2003).
[6] A. E. Tanur, J. Wang, A. L. Reddy, D. N. Lamont, Y. K. Yap, and G. C. Walker, J Phys Chem B **117,** 4618 (2013).
[7] J. R. Xiao, B. A. Gama, and J. W. Gillespie, International Journal of Solids and Structures **42,** 3075 (2005).
[8] P. J. de Pablo, I. A. T. Schaap, F. C. MacKintosh, and C. F. Schmidt, Physical Review Letters **91,** 098101 (2003).
[9] M. Kikumoto, M. Kurachi, V. Tosa, and H. Tashiro, Biophysical Journal **90,** 1687 (2006).
[10] A. Kis, S. Kasas, B. Babić, A. J. Kulik, W. Benoît, G. A. D. Briggs, C. Schönenberger, S. Catsicas, and L. Forró, Physical Review Letters **89,** 248101 (2002).
[11] L. Liu, E. Tuzel, and J. L. Ross, J Phys Condens Matter **23,** 374104 (2011).
[12] I. A. T. Schaap, C. Carrasco, P. J. de Pablo, F. C. MacKintosh, and C. F. Schmidt, Biophysical Journal **91,** 1521 (2006).
[13] C. P. Brangwynne, F. C. MacKintosh, S. Kumar, N. A. Geisse, J. Talbot, L. Mahadevan, K. K. Parker, D. E. Ingber, and D. A. Weitz, J Cell Biol **173,** 733 (2006).
[14] M. J. Bowick, D. R. Nelson, and A. Travesset, Physical Review B **62,** 8738 (2000).
[15] P. Prusinkiewicz and A. Lindenmayer, in *The Algorithmic Beauty of Plants* (Springer, 1990), p. 109.
[16] A. Frost, V. M. Unger, and P. De Camilli, Cell **137,** 191 (2009).
[17] A. Amir and D. R. Nelson, Proceedings of the National Academy of Sciences **109,** 9833 (2012).
[18] S. Srebnik and J. F. Douglas, Soft Matter **7,** 6897 (2011).
[19] F. Tian, Y. Luo, and X. Zhang, J Chem Phys **133,** 144701 (2010).
[20] A. Klug, Philos Trans R Soc Lond B Biol Sci **354,** 531 (1999).
[21] H.-K. Chan, Physical Review E **84** (2011).
[22] A. Mughal, H. Chan, and D. Weaire, Physical Review Letters **106** (2011).
[23] A. Mughal, H. Chan, D. Weaire, and S. Hutzler, Physical Review E **85** (2012).
[24] G. T. Pickett, M. Gross, and H. Okuyama, Physical Review Letters **85,** 3652 (2000).
[25] M. A. Lohr, A. M. Alsayed, B. G. Chen, Z. Zhang, R. D. Kamien, and A. G. Yodh, Physical Review E **81,** 040401 (2010).
[26] S. A. Vanapalli, C. R. Iacovella, K. E. Sung, D. Mukhija, J. M. Millunchick, M. A. Burns, S. C. Glotzer, and M. J. Solomon, Langmuir **24,** 3661 (2008).
[27] A. N. Khlobystov, D. A. Britz, and G. A. D. Briggs, Accounts of Chemical Research **38,** 901 (2005).
[28] K. L. Kohlstedt, G. Vernizzi, and M. Olvera de la Cruz, Physical Review E **80,** 051503 (2009).
[29] E. C. Oğuz, R. Messina, and H. Löwen, EPL (Europhysics Letters) **94,** 28005 (2011).
[30] F. J. Solis, G. Vernizzi, and M. Olvera de la Cruz, Soft Matter **7,** 1456 (2011).
[31] K. L. Kohlstedt, G. Vernizzi, and M. Olvera de la Cruz, J Phys Condens Matter **21,** 424114 (2009).
[32] G. Margolin, I. V. Gregoretti, T. M. Cickovski, C. Li, W. Shi, M. S. Alber, and H. V. Goodson, Molecular Biology of the Cell **23,** 642 (2012).
[33] H. Sui and K. H. Downing, Structure **18,** 1022.

[34] M. Pilhofer, M. S. Ladinsky, A. W. McDowall, G. Petroni, and G. J. Jensen, PLOS Biology **9,** e1001213 (2011).
[35] B. Alberts, *Molecular biology of the cell*, 4th ed. (Garland Science, New York, 2002).
[36] R. Rafiee and R. Pourazizi, Materials Research **17,** 758 (2014).
[37] C. Sachse, J. Z. Chen, P.-D. Coureux, M. E. Stroupe, M. Fändrich, and N. Grigorieff, Journal of Molecular Biology **371,** 812 (2007).
[38] S. Govindjee and J. L. Sackman, Solid State Communications **110,** 227 (1999).
[39] S. Tristram-Nagle and J. F. Nagle, Chemistry and Physics of Lipids **127,** 3 (2004).
[40] D. Marsh, Chem Phys Lipids **144,** 146 (2006).
[41] A. S. Reddy, D. T. Warshaviak, and M. Chachisvilis, Biochim Biophys Acta **1818,** 2271 (2012).
[42] G. van Meer, D. R. Voelker, and G. W. Feigenson, Nature reviews. Molecular cell biology **9,** 112 (2008).
[43] H. Mellor, Biochimica et Biophysica Acta (BBA) - Molecular Cell Research **1803,** 191 (2010).
[44] D. C. Camerino, D. Tricarico, and J.-F. Desaphy, Neurotherapeutics **4,** 184 (2007).
[45] T. Ruiz-Herrero, E. Velasco, and M. F. Hagan, J Phys Chem B **116,** 9595 (2012).
[46] J. B. Hutchison, A. P. K. K. Karunanayake Mudiyanselage, R. M. Weis, and A. D. Dinsmore, Soft Matter **12,** 2465 (2016).
[47] J. Zimmerberg and M. M. Kozlov, Nat Rev Mol Cell Biol **7,** 9 (2006).
[48] P. K. Mattila, A. Pykalainen, J. Saarikangas, V. O. Paavilainen, H. Vihinen, E. Jokitalo, and P. Lappalainen, J Cell Biol **176,** 953 (2007).
[49] W. M. Henne, H. M. Kent, M. G. Ford, B. G. Hegde, O. Daumke, P. J. Butler, R. Mittal, R. Langen, P. R. Evans, and H. T. McMahon, Structure **15,** 839 (2007).
[50] K. Farsad, N. Ringstad, K. Takei, S. R. Floyd, K. Rose, and P. De Camilli, J Cell Biol **155,** 193 (2001).
[51] A. N. Becalska, C. F. Kelley, C. Berciu, T. B. Stanishneva-Konovalova, X. Fu, S. Wang, O. S. Sokolova, D. Nicastro, and A. A. Rodal, Mol Biol Cell **24,** 2406 (2013).
[52] J. B. Hutchison, R. M. Weis, and A. D. Dinsmore, Langmuir **28,** 5176 (2012).
[53] Y. Yu and S. Granick, J Am Chem Soc **131,** 14158 (2009).
[54] Y.-C. Su and J. Z. Y. Chen, Soft Matter **11,** 4054 (2015).
[55] A. Šarić and A. Cacciuto, Physical Review Letters **108** (2012).
[56] L. Ramos, Science **286,** 2325 (1999).
[57] I. Koltover, J. O. Rädler, and C. R. Safinya, Physical Review Letters **82,** 1991 (1999).
[58] B. J. Reynwar, G. Illya, V. A. Harmandaris, M. M. Muller, K. Kremer, and M. Deserno, Nature **447,** 461 (2007).
[59] S. C. Hayden, G. Zhao, K. Saha, R. L. Phillips, X. Li, O. R. Miranda, V. M. Rotello, M. A. El-Sayed, I. Schmidt-Krey, and U. H. Bunz, J Am Chem Soc **134,** 6920 (2012).
[60] X. Chen, F. Tian, X. Zhang, and W. Wang, Soft Matter **9,** 7592 (2013).
[61] A. Chaudhuri, G. Battaglia, and R. Golestanian, Phys Biol **8,** 046002 (2011).
[62] M. Deserno, Journal of Physics: Condensed Matter **16,** S2061 (2004).
[63] A. Xu, M. Yao, G. Xu, J. Ying, W. Ma, B. Li, and Y. Jin, Int J Nanomedicine **7,** 3547 (2012).
[64] X. Yi, X. Shi, and H. Gao, Physical Review Letters **107** (2011).
[65] L. Paasonen, T. Laaksonen, C. Johans, M. Yliperttula, K. Kontturi, and A. Urtti, J Control Release **122,** 86 (2007).
[66] M. Deserno, Physical Review E **69** (2004).
[67] B. J. Reynwar and M. Deserno, Soft Matter **7,** 8567 (2011).
[68] M. M. Müller, M. Deserno, and J. Guven, Europhysics Letters (EPL) **69,** 482 (2005).
[69] J. A. Champion and S. Mitragotri, Proc Natl Acad Sci U S A **103,** 4930 (2006).

[70] Y. Zhang, S. Tekobo, Y. Tu, Q. Zhou, X. Jin, S. A. Dergunov, E. Pinkhassik, and B. Yan, ACS Appl Mater Interfaces **4,** 4099 (2012).
[71] B. Wang, L. Zhang, S. C. Bae, and S. Granick, Proc Natl Acad Sci U S A **105,** 18171 (2008).
[72] R. N. Frese, J. C. Pamies, J. D. Olsen, S. Bahatyrova, C. D. van der Weij-de Wit, T. J. Aartsma, C. Otto, C. N. Hunter, D. Frenkel, and R. van Grondelle, Biophys J **94,** 640 (2008).
[73] M. Deserno and W. M. Gelbart, The Journal of Physical Chemistry B **106,** 5543 (2002).

CHAPTER 2

MOLECULAR DYNAMICS SIMULATION TECHNIQUES

In this chapter, we describe the simulation techniques used to find the steady-state structures of cylindrical crystals, as well as the techniques used to determine the bending stiffness of cylindrical crystals. All of our simulations utilized a molecular dynamics (MD) simulation scheme, and were performed using the LAMMPS software package developed at Sandia National Laboratory (*lammps.sandia.gov*).[1]

Conceptually speaking, a molecular dynamics simulation is one that uses Newton's equations of motion to determine the trajectories of a system of many interacting particles. By using purely numerical methods to integrate Newton's equations over a fixed interval of time, these simulations provide us to a comprehensive picture of the dynamical evolution of a large system of particles that would be prohibitively complex to investigate analytically. Such numerical calculations entail calculating the forces between pairs of particles using their inter-atomic interaction potentials, as well as calculating mechanical forces on particles caused by external force fields.

The use of Langevin dynamics is an MD approach that explicitly includes friction and viscosity into simulations through the use of an implicit solvent; it also allows for control over the temperature of the particles in the simulation, thereby approximating the canonical ensemble. Our simulations utilized Langevin dynamics to evolve the system via simulated annealing, which allowed us to indirectly control the system's temperature over the course of each simulation. Further details on this procedure can be found in (Goga *et al*., 2012).[2] One distinct advantage of using simulated annealing as opposed to

strictly minimizing energies or solving the equations analytically is that it allows us to capture intermediate metastable configurations.

To examine a wide range of different particle interactions, two different inter-atomic potentials were used throughout our simulations: the Lennard-Jones potential, which we define as

$$V_{LJ}(r) = \epsilon\left[\left(\frac{d}{r}\right)^{12} - 2\left(\frac{d}{r}\right)^{6}\right], \quad \text{(Eq. 7)}$$

and the Morse potential, which is defined as

$$V_{Morse}(r) = \epsilon\left[e^{-2\gamma d\left(\frac{r}{d}-1\right)} - 2e^{-\gamma d\left(\frac{r}{d}-1\right)}\right], \quad \text{(Eq. 8)}$$

where ϵ controls the interaction strength and the dimensionless parameter γd controls the range of attraction (a large γd corresponds to a short-range potential). In both cases, d represents the location of the potential minima. For reference, the Lennard-Jones potential has been plotted in Figure 9 alongside the Morse potential for $\gamma d = 10$ and $\gamma d = 30$, two of the values used in our simulations.

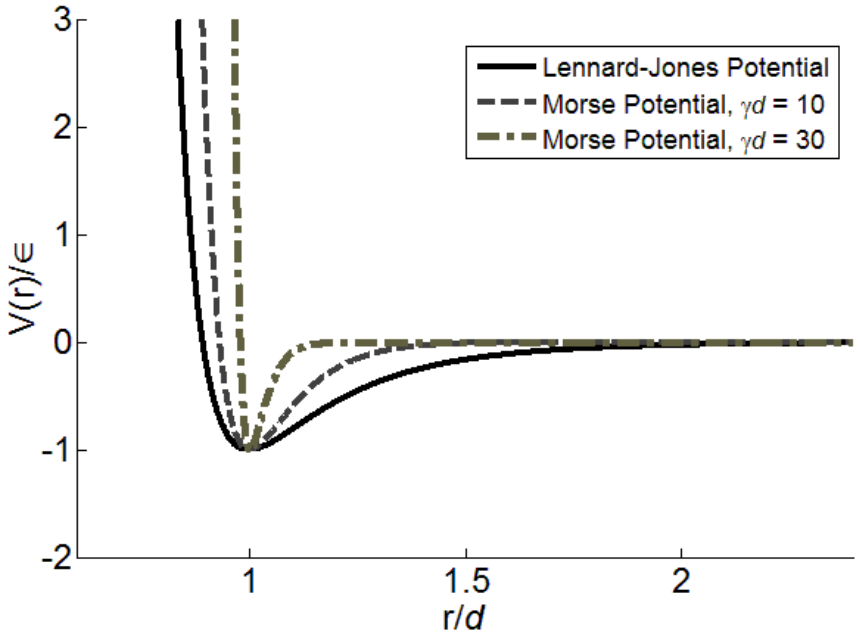

Figure 5. The pairwise potential as a function of particle separation for both Lennard-Jones and Morse potentials. The γd=10 and γd=30 Morse potentials have a shorter ranged attraction and a steeper core repulsion than the Lennard-Jones potential.

2D simulations of particles on a straight cylinder

We employed computer simulations to find the steady state structures that appear using different pair-wise interaction potentials (Figure 9) and a range of different cylinder circumferences, C. The purpose of these particular simulations was to learn what steady state structures are favorable as a function of these two parameters.

To accomplish this, we first determined how to calculate forces between nearby particles on the cylinder, and then hard-coded these interactions into our simulations. Starting with particles at high temperatures, we slowly lowered the temperature until they formed into a stable crystal; this data could then be analyzed.

Calculating interactions between particles

Although this problem is three-dimensional because the interactions are defined by separation in 3D space, the requirement that the particles lie on the surface of a cylinder allows us to translate it into a two-dimensional equivalent. More precisely, we represented the cylinder's surface in planar Cartesian space by letting $[C\varphi/2\pi\,, \mathrm{z}] \rightarrow [x, y]$, where C is the circumference of the cylinder and φ is the azimuthal angle in cylindrical coordinates. In this representation, the x-axis necessarily has periodic boundary conditions and the y-axis does not. This method was a computationally convenient way to confine the spheres to the surface of the cylinder (Figure 10).

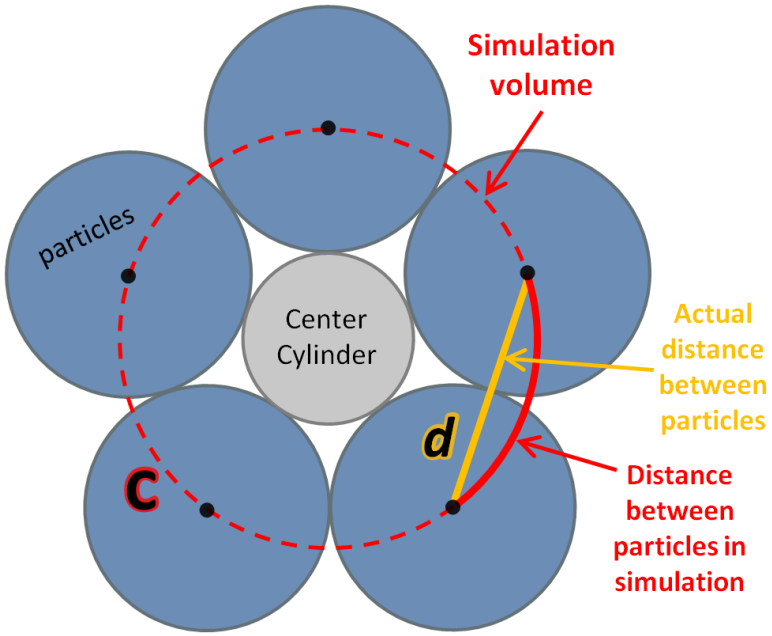

Figure 6. Cross-sectional diagram of the simulation space. This schematic demonstrates the difference between the inner cylinder circumference (which belongs to the physical rod), and the outer cylinder circumference C (which intersects the centers of mass of the particles) where the actual simulation takes place. It also illustrates the necessary adjustment to the way that distances between particles are calculated in this two-dimensional mapping, in order to correctly compute the forces between particles.

The chosen interaction potential also needed be adjusted as part of this two-dimensional mapping; interactions between particles must depend on their separation in Euclidean space, whereas the simulation coordinates are measured along the surface of the cylinder (Figure 10). This difference leads to a distortion along the $\hat{x}$ (or $\hat{\varphi}$) direction, which we accounted for in the simulations. For any two particles separated by Δx and Δy on the planar surface, the true Euclidean separation, *r*, was computed via

$$r = \sqrt{(C/\pi)^2 \cdot \sin^2(\Delta x \cdot \pi/C) + \Delta y^2} \ . \qquad \text{(Eq. 9)}$$

For these two particles, the magnitude of the interaction force, $\left|\vec{F}\right|$, was obtained from the force-distance curves appropriate for the Lennard-Jones or Morse cases. The component of the force along the circumferential axis ($\hat{x}$) was computed as

$$F_x = \left|\vec{F}\right| \cdot (C/2\pi r) \cdot \sin(\Delta x \cdot 2\pi/C) \ , \qquad \text{(Eq. 10a)}$$

and the force along the cylinder axis ($\hat{y}$) was computed as

$$F_y = \left|\vec{F}\right| \cdot (\Delta y/r) \ . \qquad \text{(Eq. 10b)}$$

Therefore, the 2D projection of the pairwise potentials onto the (*x*,*y*) plane is slightly anisotropic. All of our simulations were coded to include Equations 9 and 10 explicitly.

Simulated annealing parameters

Since the purpose of these simulations was to find all possible steady-state configurations of the particles, we needed to implement an annealing schedule that gradually increased and decreased repeatedly over time in order to carefully search out the phase space of configurations of particles for metastable states. In all of the simulations described in this section, the particles were cooled from $T_i = 8\epsilon/k_B$ to

$T_f=0.01\epsilon/k_B$ *via* a simulated annealing schedule over a period of $5x10^5$ iterations. A typical annealing schedule from these simulations is shown below in Figure 11.

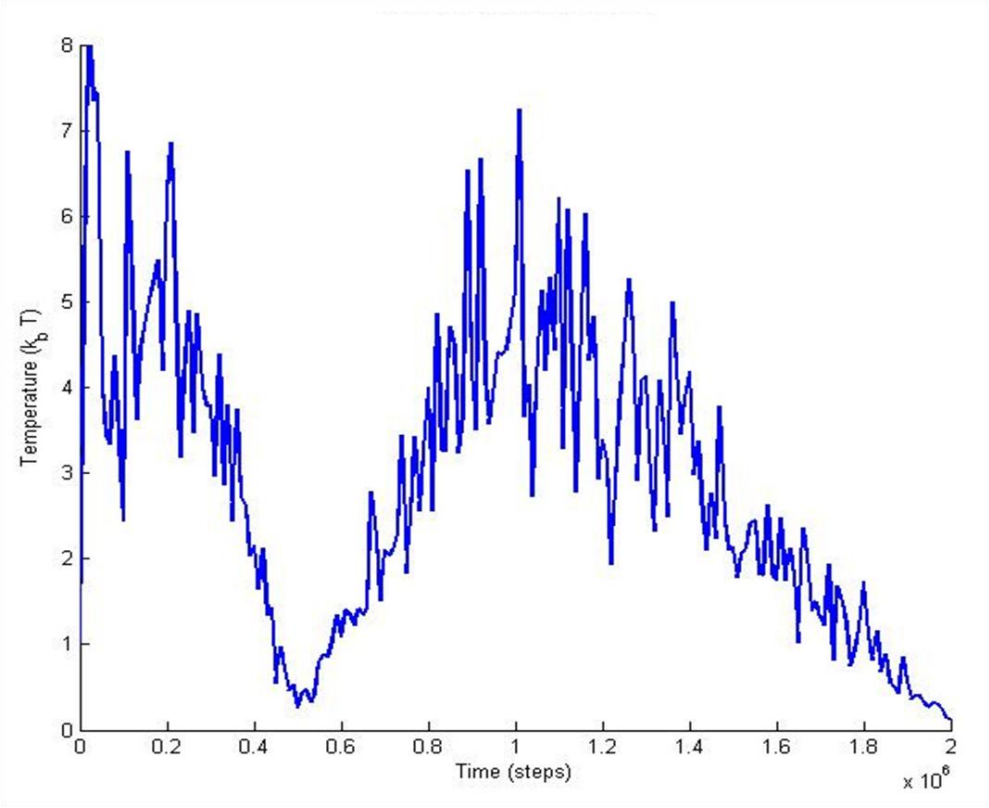

Figure 7. Typical annealing schedule. The particles start at 8, and the temperature is alternately raised and lowered until the overall temperature reaches 0.01.

Prior to the start of each simulation, the total number of particles was chosen such that the area fraction of the system was equal to 0.7; both the volume and number of particles in the system were then kept fixed throughout the annealing process. Each iteration of the algorithm represented a time step of 0.02 s and computed only the interactions between pairs of particles within 2*d* of each other. The mean squared displacement of an individual particle during each time step was $(2^{-1/3}x10^{-2}\, k_BT/\epsilon)d^2$. At

the beginning of this process, particles were randomized at high temperatures, then allowed to diffuse freely in a medium with an effective viscosity of η=0.95 mPa/s (similar to water at room temperature). Once the particles were cooled into a stable crystal and the annealing was complete, the coordinates of each sphere were recorded. This process was then repeated with a new value of *C* and with a new arrangement of particles.

3D simulations of particles on a bent rod

We next asked whether bending the rod (and thereby imposing a nonzero Gaussian curvature) leads to interesting new surface structures, and whether these structures alter the bending stiffness. Because the introduction of Gaussian curvature leads to a curved surface with a nontrivial shape, simulating the particles in two dimensions was not practical in this case. Instead, we simulated the particles in three dimensions, and artificially added a force field which bound the particles to the surface of a bent cylinder.

3D Force Field

All our simulations used a force field to pin the particles into the surface of the cylinder. By design, this field acts perpendicular to the surface of the bent cylinder; it has a nontrivial shape and hence is outlined here. We first defined a set of 'bent' cylindrical coordinates, with $\hat{z}_b$ parallel to the axis of the bent cylinder, and $\hat{r}_b$ as perpendicular to the plane defined by $\hat{z}_b$ (Figure 12).

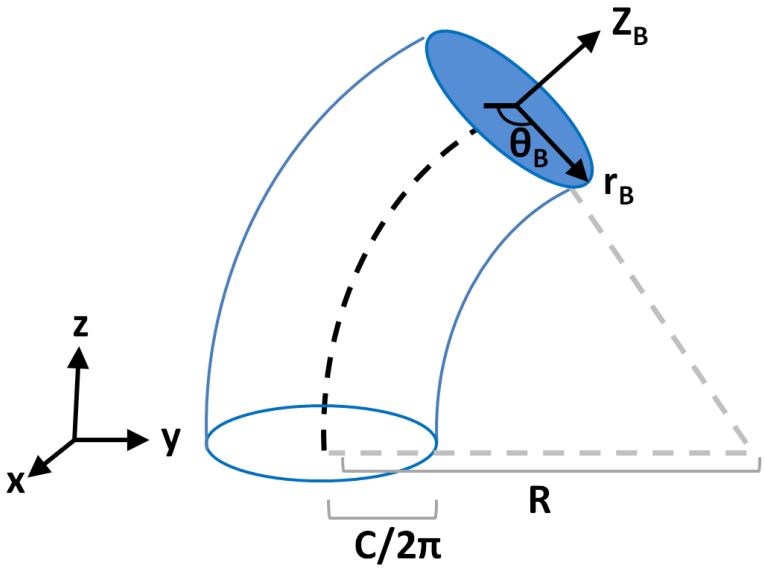

Figure 8. The 'bent cylinder' coordinate system we used to define the force field keeping the particles confined onto the cylinder.

Using this new coordinate system, we next wrote the force field confining the particles onto the cylinder as a harmonic spring force;

$$\vec{F}(\vec{r}) = -k\left(\vec{r}\cdot\hat{r}_b - \frac{C}{2\pi}\right)\cdot\hat{r}_b \qquad \text{(Eq. 11)}$$

where *k* is the spring constant pinning particles to the curved cylinder surface. Writing the force field next required computing $\vec{r}\cdot\hat{r}_b$, which was done by first defining the quantities

$$x_b = x, \qquad \text{(Eq. 12a)}$$

$$y_b = (y-R)\cdot\left[1 - R/\sqrt{z^2+(y-R)^2}\right], \qquad \text{(Eq. 12b)}$$

$$z_b = z\cdot\left[1 - R/\sqrt{z^2+(y-R)^2}\right]. \qquad \text{(Eq. 12c)}$$

We could then write the quantity $\vec{r}\cdot\hat{r}_b$ as

$$\vec{r}\cdot\hat{r}_b = r_b = \sqrt{{x_b}^2+{y_b}^2+{z_b}^2}, \qquad \text{(Eq. 13)}$$

and the force field thus becomes

$$\vec{F}(\vec{r}) = -k\left(r_b - \frac{C}{2\pi}\right)\cdot\left[\frac{x_b}{r_b}\hat{x} + \frac{y_b}{r_b}\hat{y} + \frac{z_b}{r_b}\hat{z}\right]. \qquad \text{(Eq. 14)}$$

This derived forced field was used in each of our simulations to keep the particles confined to our bent cylindrical surface. At every iteration and for each particle in our simulation, we computed the vector components of the force field and applied it to each separate particle accordingly.

The validity of this force-field can easily be checked by simply plotting a vector field for a few values of *R* (Figure 13). This reveals the force field derived above is numerically stable in the limit $R \rightarrow \infty$, and also for small *R*. Additionally, the vector field points perfectly normal to the surface of the cylinder at all positions in space. This is a critical feature of the field; were it not true, the in-plane components of the field would push the particles around on the surface of the cylinder during the simulations.

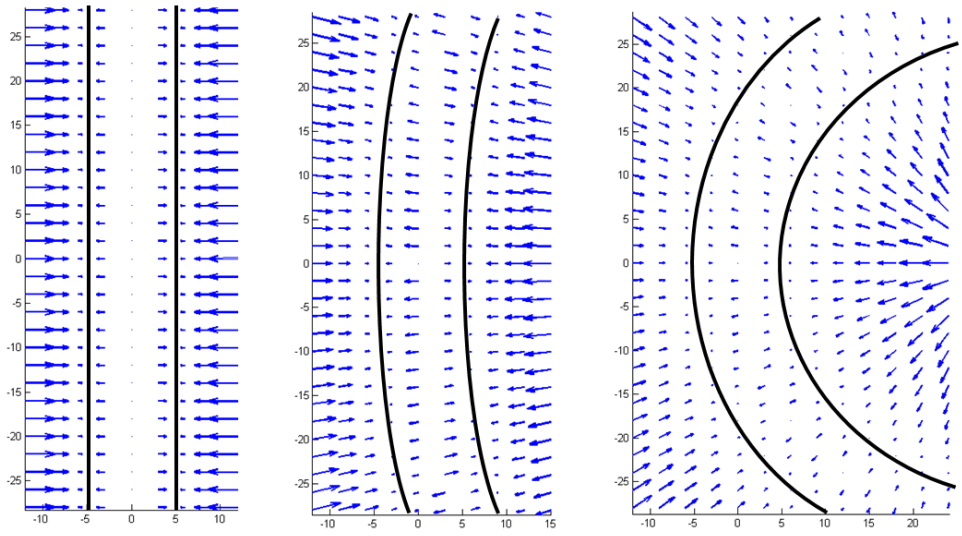

R = 1000000000 **R = 100** **R = 30**

Figure 9. Illustration of the force field confining the particles onto the surface of the bent cylinder. It acts normal to the surface regardless of the position of the particle.

Using this method, we could effectively pin the particles to the surface by applying a field with a spring constant (k/d) >> k_bT and also (k/d) >> ϵ. Since these simulations were computed in three dimensions, no corrections to the interactions forces between the particles were necessary.

Simulation procedure

Each of our simulations utilized a similar annealing scheme to the 2D simulations described previously (Figure 11). The 3D simulations began at a temperature of $T=2k_B/\epsilon$ with particles at randomized positions within the 3D simulation volume, and then a large spring force was incrementally applied to the particles to confine them to the surface of an unbent cylinder. The particles were then annealed into a steady-state crystalline structure; starting at an initial temperature of $T_i=2k_B/\epsilon$, the particles were cooled to $T_f= 0.1k_B/\epsilon$ over a period of 10^6 iterations, and the positions of the particles were then recorded. We defined the length L as the total length along the curved axis of the cylinder. For the simulations reported here, L ranged from $20d$ to $100d$, and the number of spheres in each simulation was chosen such that the total length of the annealed crystal was at least $L=20d$.

At the start of each simulation, the curvature (1/R) was set to a value of $\alpha/10000$, with $\alpha=1$. (The initial configuration was thus a very slightly curved cylinder, though it is approximately straight.) Each iteration, α was incremented by a value of 0.2, and the particles were allowed to reach a new steady configuration on this new surface during a

period of 10^4 iterations. We found that this provided sufficient time for the particles to reach steady state; decreasing the size of each increment of α and allowing more iterations to reach a new steady state configuration did not measurably change the outcome of the simulation. This process was repeated until the curvature reached $L/2\pi$, which is the maximum curvature that can be applied to a cylinder of length L. The steady-state positions of the particles were recorded at each iteration of curvature, which were then analyzed to determine the stiffness of the cylinder.

It is also worth noting that, using this method, the crystal lattice must not have any vacancies or defects prior to bending in order for the data to be trustworthy. The existence of a vacancy may affect the energy landscape, and is a very undesirable feature. Determining the structure of the crystal is also a relatively tricky task considering its constituent particles lie on a curved surface; this analysis will be examined in greater detail in Chapter 4.

Notes

[1] S. Plimpton, Journal of Computational Physics **117,** 1 (1995).

[2] N. Goga, A. J. Rzepiela, A. H. de Vries, S. J. Marrink, and H. J. C. Berendsen, Journal of Chemical Theory and Computation **8,** 3637 (2012).

CHAPTER 3

SELF-ASSEMBLY ON A CYLINDER

In this chapter, we discuss MD simulations of systems of Lennard-Jones and Morse particles that were used to identify steady-state configurations of these particles confined to a cylindrical lattice. We then propose a simple 1-dimensional model based on geometry to explain the range of stability of each of these configurations, and compare with the results from our MD simulations. We then discuss implications of these results for further studies.

A crystal lattice, when confined to the surface of a cylinder, must have a periodic structure that is commensurate with the cylinder circumference.[1,2] This constraint can frustrate the system, leading to oblique crystal lattices or to structures with a chiral seam known as a 'line slip' phase, neither of which are stable for isotropic particles in equilibrium on flat surfaces. In this study, we use molecular dynamics simulations to find the steady-state structure of spherical particles with short-range repulsion and long-range attraction far below the melting temperature. We vary the range of attraction using the Lennard-Jones and Morse potentials and find that a shorter-range attraction favors the line-slip. We develop a simple model based only on geometry and bond energy to predict when the crystal or line-slip phases should appear, and find reasonable agreement with the simulations. The simplicity of this model allows us to understand the influence of the commensurability constraint, an understanding that might be extended into the more general problem of self-assembling particles in strongly confined spaces.

Sphere packing in a cylindrical geometry

We begin by considering the example of a perfect hexagonal lattice that is wrapped onto the surface of a cylinder (Fig. 14). This example provides a useful reference for our later discussion of the structures found in simulations. In this problem, the fact that the Gaussian curvature is zero everywhere avoids curvature-induced defects. Instead, the structure is subject to the constraint that it be invariant under a 2π rotation about the cylinder axis. This discrete rotational symmetry leads directly to the conclusion that only a discrete set of cylinder circumferences can accommodate a perfect hexagonal lattice. Below, we refer to this discrete set of configurations with the subscript 0.

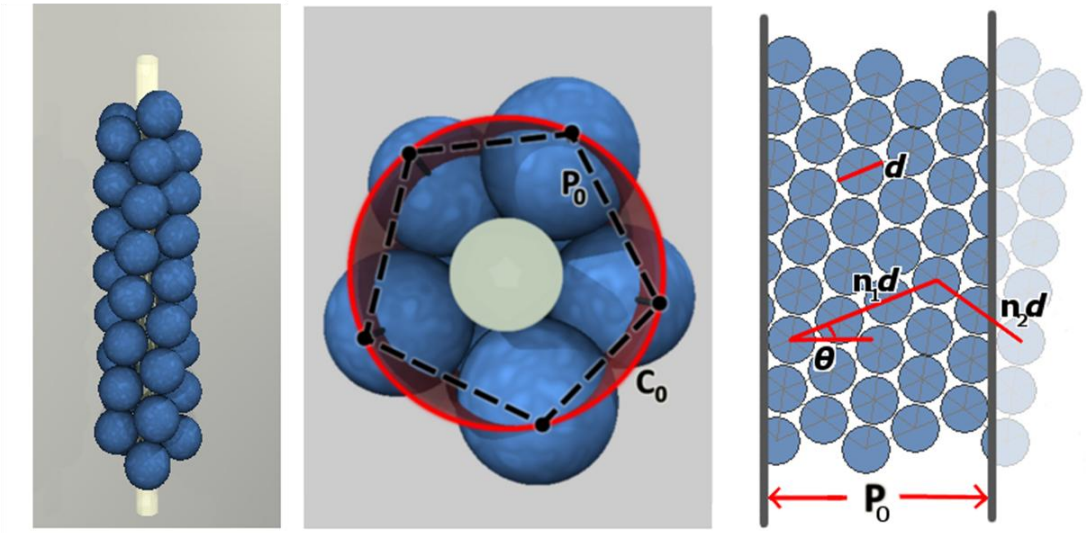

Figure 10. Illustrations of the particle-and-cylinder system. (a) Spheres are attached to the cylinder surface in a perfect hexagonal lattice. (b) A top view of this lattice, projected onto a plane perpendicular to the cylinder axis. Here, C_0 is the circumference of the circle that intersects the centers of the particles, and P_0 is the perimeter of the corresponding inscribed polyhedron. (c) The same lattice, projected into a plane created by slicing the crystal vertically and laying it on a flat surface. Note that this is not the plane defined by the surface of C_0 (which would distort the metric). The angle θ and the lattice constants n_1 and n_2 have been labeled.

To define the geometry, we consider a cylinder of circumference C, whose surface contains the center of mass of each particle (rather than the cylinder whose surface lies tangent to each sphere). The unit vector $\hat{z}$ lies along the cylinder axis and $\hat{\varphi}$ lies in the circumferential direction. To express the 2π rotation symmetry, we first define two lattice translation vectors $\boldsymbol{a}_1$ and $\boldsymbol{a}_2$. For convenience, we further define $\boldsymbol{a}_1$ as the lattice vector that lies closest to the $\hat{\varphi}$ direction. Because we are interested in the packing of three-dimensional spheres, we define $\boldsymbol{a}_{1,2}$ as the nearest-neighbor spacing in three-dimensional Euclidean space. Perhaps the most straightforward way to write the rotational symmetry condition is to require that the pathway defined by n_1 steps along $\boldsymbol{a}_1$ and n_2 steps along $\boldsymbol{a}_2$ form a simple polygon enclosing the cylinder. The projection of the perimeter of this polygon along $\hat{\varphi}$ (Fig. 14b) is a useful parameter for defining the commensurability constraint. We label this projected polygon P.

For the case of a perfect hexagonal crystal, $|\boldsymbol{a}_{1,2}| = d$ (the particle diameter) and $\boldsymbol{a}_{1,2}$ are separated by an angle of π/6. The 2π-rotational symmetry then reduces to the requirement that the perimeter of the polygon be given by P_0, which is defined by [3-6]

$$P_0(n_1,n_2) = d\,(n_1^2 + n_2^2 + n_1 n_2)^{1/2}. \qquad \text{(Eq. 15)}$$

Likewise, maintaining perfect hexagonal symmetry also requires the circumference C (Figure 14b) to be expressible in terms of n_1 and n_2. This relationship may be found from

basic geometry, and the result is a transcendental equation that defines the allowed circumferences $C_0(n_1,n_2)$ for a hexagonal lattice:

$$n_1 \cdot \sin^{-1}\left[\left(\frac{\pi d}{2C_0}\right)\cdot\frac{2n_1+n_2}{\sqrt{{n_1}^2+n_1n_2+{n_2}^2}}\right] \;+\; n_2 \cdot \sin^{-1}\left[\left(\frac{\pi d}{2C_0}\right)\cdot\frac{2n_2+n_1}{\sqrt{{n_1}^2+n_1n_2+{n_2}^2}}\right] \;=\; \pi\,. \qquad \text{(Eq. 16)}$$

For each (n_1,n_2), there is also a fixed orientation of the lattice, θ_0, which we define as the angle between $\boldsymbol{a}_1$ and $\hat{\varphi}$ (Figure 14c):

$$\theta_0(n_1,n_2) = \tan^{-1}\left(\frac{\sqrt{3}\,n_2}{2n_1+n_2}\right). \qquad \text{(Eq. 17)}$$

For each value of C_0, there are in general two distinct values of θ_0, which correspond to permuted values of n_1 and n_2. These two structures have opposite chirality and are physically indistinguishable.

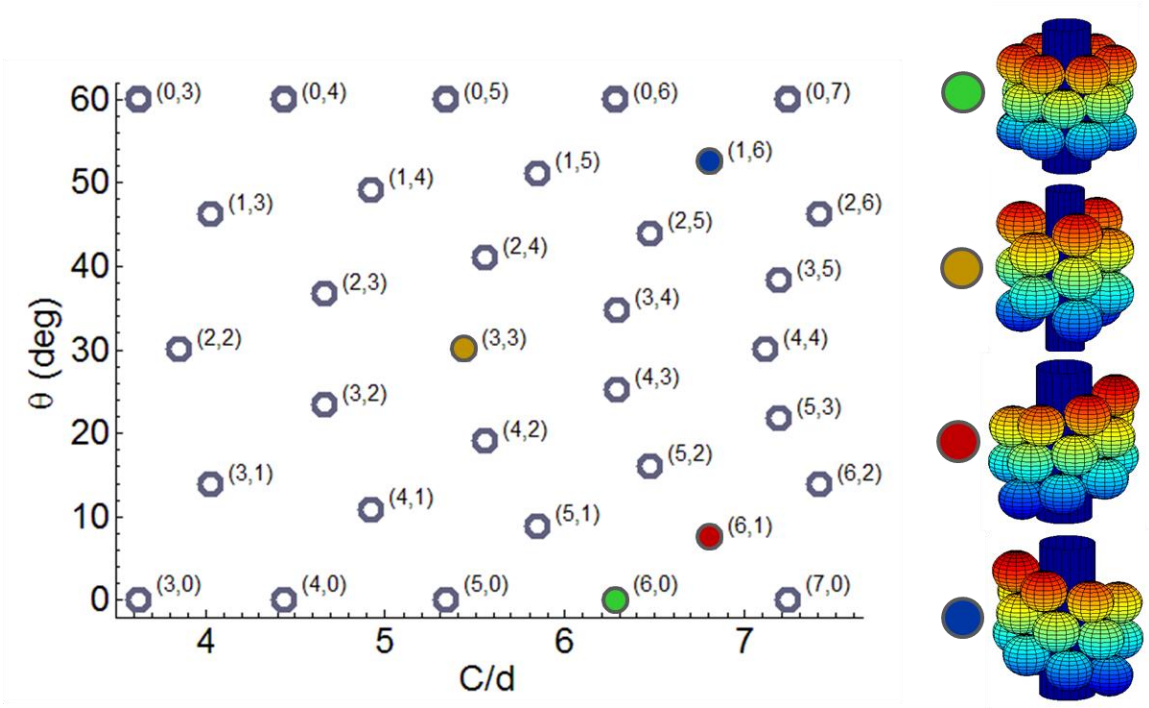

Figure 11. The values of $C_0(n_1,n_2)$ are plotted alongside their corresponding set of integers (n_1,n_2). These points mark locations where a defect-free hexagonal crystal fits on the cylinder surface. Exchanging n_1 and n_2 results in a reflection across $\theta=30°$.The two values correspond to equivalent configurations (a chiral pair).

In Figure 15, the open circles show $(C_0(n_1,n_2), \theta_0(n_1,n_2))$: these are the configurations that are allowed for perfect hexagonal lattices as defined by equations 16 and 17. Each point is labeled by the corresponding set of integers (n_1,n_2). Note that configurations with $\theta_0 \geq 60^o$ are identical to configurations with $0 \leq \theta_0 < 60^o$ because of the 6-fold rotational symmetry of the lattice.

The question that we now address with our simulations is how the set of configurations is altered when there is a finite interaction potential and the spheres can move freely along the cylinder's surface. Or, more to the point, what structures appear when $C \neq C_0$?

Simulations and analysis

We used MD simulations (as described in Chapter 2) to determine the steady state structures that appear under conditions of different interaction potentials (Figure 9) and across a range of cylinder circumferences. We also developed an algorithm to detect the crystallographic orientation of the particles with respect to the cylinder axis, θ, to use as our principal measure of the structure of each annealed crystal.

Annealing Parameters

Prior to the start of each simulation, the total number of particles is the system was chosen such that the area fraction of the system was equal to 0.7; both the volume

and number of particles in the system were then kept fixed throughout the annealing process. Each iteration of the algorithm represented a time step of 0.02s and computed only the interactions between pairs of particles within 2*d* of each other. The mean squared displacement of an individual particle during each time step was $(2^{-1/3}x10^{-2}$ $k_BT/\epsilon)d^2$. At the beginning of this process, particles were randomized at high temperatures, then allowed to diffuse freely in a medium with an effective viscosity of η=0.95 mPa/s (similar to water at room temperature). Once the particles were cooled into a stable crystal and the annealing was complete, the coordinates of each sphere were recorded. This process was then repeated with a new value of *C* and with a new arrangement of particles.

To verify that the obtained structures reflected the low-temperature limit, a few simulations were instead cooled to a lower temperature of $T_f=10^{-4}\epsilon/k_B$ over a period of $5x10^7$ iterations; the values of θ measured in these cases was identical to the values measured in our previous simulations. This indicated that the reduced temperature did not make an appreciable impact on our data. We also performed several spatially large simulations, where the y-axis boundaries were separated by a distance of several hundred particle diameters. In these cases, the system was large enough to form crystalline domain boundaries, but we found the structure of each individual domain to be no different from those observed in smaller crystals at the same circumference. In other words, we found that the distance between the x-axis boundaries (the cylinder circumference) is the only important dimension of the system.

The annealing process was completed using the Lennard-Jones and Morse interaction potentials (Eq. 7 and Eq. 8), and across several thousand cylinder circumferences between C/d=3.6 and C/d=7.6.

Detecting the configuration angle θ of the particles

For each of these simulations, we used the sphere positions to measure the average crystallographic angle, θ, between the crystal lattice and the cylinder (Figure 14a and 14c). This was accomplished through the following algorithm: first, the neighbors of each particle were calculated, which was done by finding the Delaunay triangulation of the positions of all the particles (pairs of particles connected by an edge in the Delaunay map were considered neighbors). We discounted any neighbor pairs separated by a distance greater than 1.5d away from one another, and then every particle with six neighbors was indexed. Next, we recorded the angles defined by the $\hat{\varphi}$ axis and the bonds between each of the indexed spheres and each of its neighbors.

Using this data, we created a histogram of all angles, which necessarily has six distinct peaks. If two or more sets of six peaks were found, a polycrystalline structure was likely present (an inference confirmed by visual inspection of several such cases), and the data was rejected. The angles comprising the peak closest to 0° were then averaged. This average value, denoted as θ, could then be plotted as a function of C/d.

Note, however, that this definition of θ measures the structure of the crystal in a way that is slightly different (though physically more meaningful) from the one used in Eq. 17, and this difference leads to a very small discrepancy between our theory and our data that vanishes for large values of C/d. Briefly put, the discrepancy in the measured

values of θ is caused by a subtle difference in the way that distances between particles are measured in Eq. 17 and in our analysis. In both of these cases, the separation vector ***r*** is two-dimensional because the spheres' positions are parameterized along some surface. However, Eq. 17 constrains the particles to exist on a slightly different surface than our simulations do (Figure 16).

Indeed, in Eq. 17 the component of ***r*** that is perpendicular to the $\hat{\varphi}$ axis is only approximately parallel with the cylinder axis; this is due to the difficulty in defining θ_0 with respect to a fixed axis. Because of this error, Eq. 17 slightly over-estimates θ_0 for small values of C/d. At the very least, the discrepancy between these two coordinate systems is somewhat mitigated by the use of Eq. 9 in the analysis of our simulations.

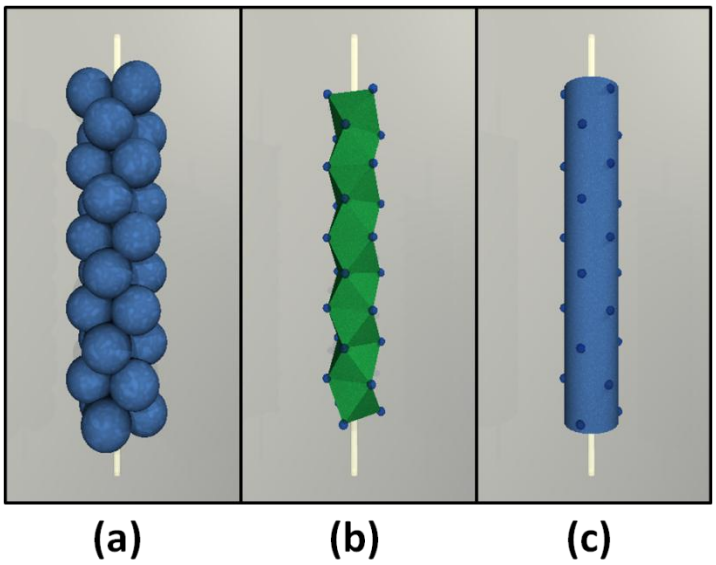

Figure 12. (A) A prototypical arrangement of particles for some C_0/d. Here, (B) depicts the surface connecting these particles as parameterized by Eq. 17, whereas (C) depicts the surface connecting the particles as parameterized in the analysis of the data from our simulations. This slight geometric difference causes the small discrepancy manifested in our data.

Results

Lennard-Jones particle interactions

We represent the steady-state configurations of the spheres by plots of (C/d, θ). This data, for systems of Lennard-Jones particles, is presented in Figure 17. The pale grey bars in the background of this plot correspond to the theory derived in the next section. As expected, we find the uniform crystal phases (shown in blue/black) at the discrete values of (C_0/d, θ_0) associated with a perfect hexagonal lattice. We note, however, that for small C/d the values of θ_0 with $n_2 > n_1$ are slightly different from the values of θ extracted from our simulations. As stated in the previous section, this is due to a subtle difference in the way the two angles are defined, which becomes small as C/d increases.

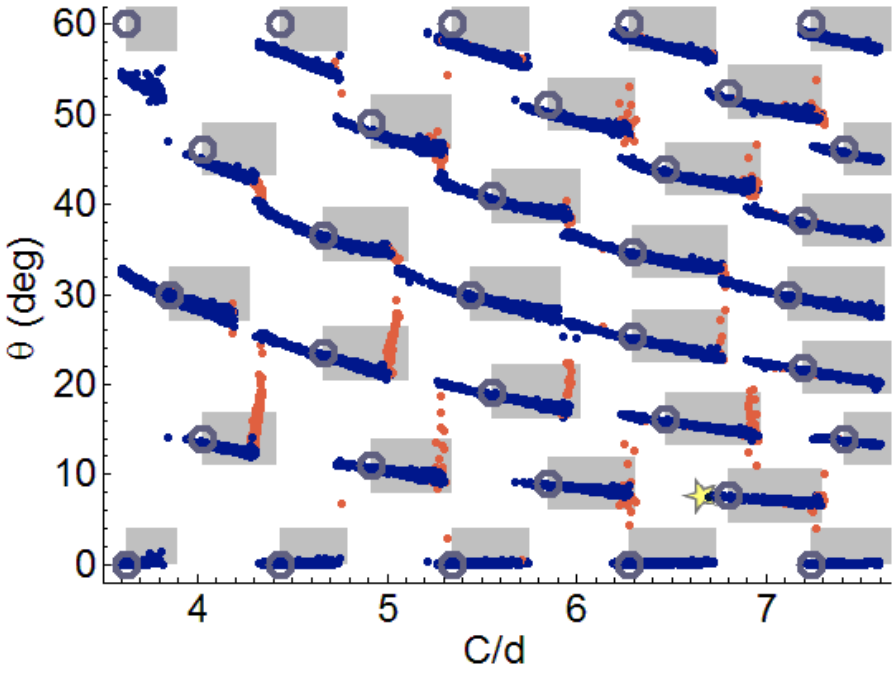

Figure 13. Steady state configurations observed in computer simulations with Lennard-Jones interactions, plotted as θ vs C/d. Red/gray data points indicate the existence of a

line-slip phase, and blue/black data points indicate a continuous uniform crystal. The large circles label the same analytically determined values for C_0 as in Figure 15, and the gray blocks show defect-free regions as predicted by Eq. 19 and Eq. 21. The plot's axes span from θ=0 to θ=60^o because of the six-fold symmetry of the lattice. The star at (C/d,θ)=(6.76,7.45^o) indicates the location of the simulation examined in greater detail in Figure 22.

In contrast to the hard-sphere case, uniform lattices persist across islands of parameter space surrounding each (C_0/d, θ_0). Between these islands of uniform lattices, we find narrow regions of parameter space that have structures with a chiral defect (orange/gray points); these correspond to the line-slip phases reported for hard spheres.[7] One (perhaps unexpected) feature of this graph is its asymmetry: an expansion of C away from C_0 systematically leads to a reduction of θ. This is due to the fact that, when a perfect hexagonal lattice cannot assemble on the cylinder at any angle, it becomes preferential to form an oblique lattice instead by stretching along the $\hat{\varphi}$ axis– a feature examined in greater detail in the following paragraphs. Chiral pairs in this state are no longer similar under rotation, but are instead similar only by reflection across θ = 0°. The redundant data was omitted from the plot.

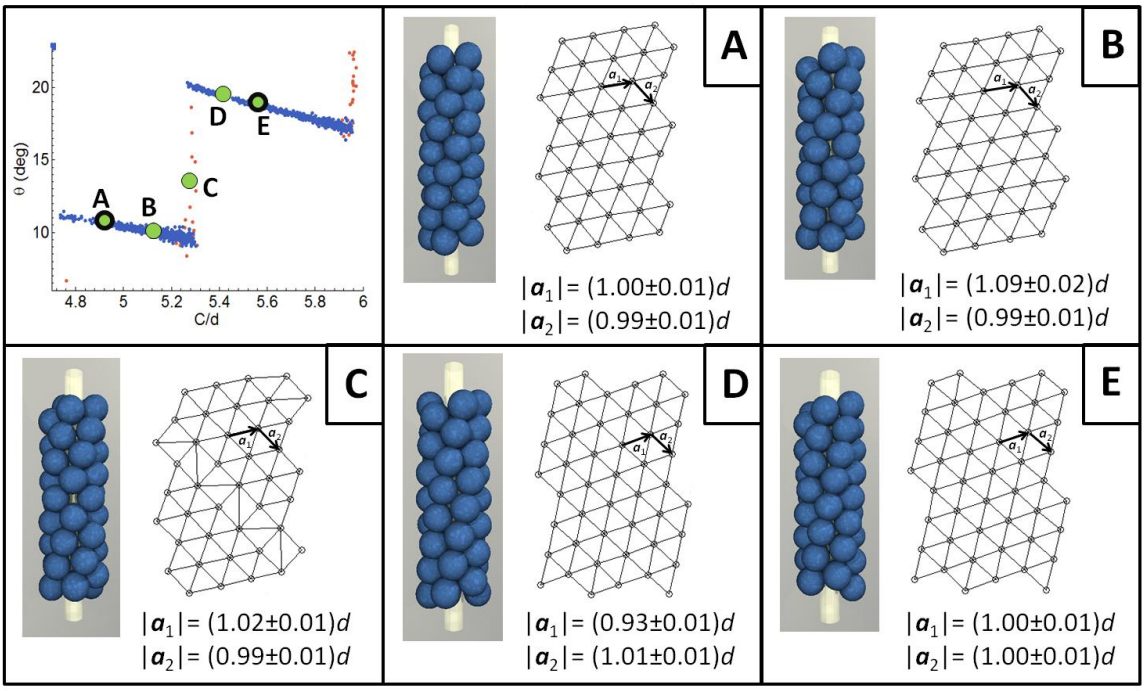

Figure 14. Steady-state configurations obtained from the simulations are shown for a range of values of C/d to better illustrate the structures found in Figure 17. In each case, the average magnitude of the lattice vectors, $\boldsymbol{a}_1$ and $\boldsymbol{a}_2$, are provided alongside their standard deviation. The line segments show the Delaunay triangulation of the lattice, on top of which $\boldsymbol{a}_1$ and $\boldsymbol{a}_2$ have also been drawn. (A) A hexagonal lattice appears at the value of C_0 for $(n_1,n_2) = (4,1)$. (B) The lattice stretches along $\boldsymbol{a}_1$ as C/d increases. (C) A 'line slip' structure with a helical defect emerges in response to the strain placed on the crystal lattice. This is manifested in alternating pairs of 5-7 disclinations which span the length of the lattice. (D) The crystal, arranged at a new angle, is slightly compressed along $\boldsymbol{a}_1$. (E) The lattice is again hexagonal at C_0 corresponding to $(n_1,n_2) = (4,2)$.

In Figure 18, we show the real structure at selected points in the (C, θ) plane. Figure 18a shows the structure of a hexagonal lattice observed at the (C_0, θ_0) corresponding to $(n_1,n_2) = (4,1)$. As one increases the circumference of the cylinder away from some particular value of C_0, the preferred state becomes an oblique lattice, where the lattice unit vector nearest to the circumferential axis of the cylinder ($\boldsymbol{a}_1$) is slightly increased and the other lattice vector ($\boldsymbol{a}_2$) remains unchanged within uncertainty (Figure

18b). Hence, we find that the cylinder stabilizes a new oblique crystal symmetry, which is not found on planar surfaces.

When the circumference is increased further, the strain proves to be too large and an oblique lattice at this orientation is no longer viable. The lattice then develops a chiral defect, which is the line-slip structure reported earlier.[8] This structure is shown in Figure 18c. The line-slip defect itself consists of a line of 5-fold and 7-fold disclinations, as shown by the Delaunay triangulation of Figure 18c. Although the structure seems to resemble a single dislocation line (of the sort that might be found in a polycrystalline structure on a planar surface), it actually consists of *two* adjacent dislocation lines. Here, the lines have zero net Burgers vector, separating two crystal phases that have the same symmetry and orientation.

With still greater expansion of C, the observed structure shifts to a new crystal; this lattice is also slightly oblique, but is compressed along $\boldsymbol{a}_1$ rather than stretched (Figure 18). This lattice corresponds to a distortion of the hexagonal lattice with (n_1,n_2) = (4,2). As the circumference is increased, the lattice compression steadily decreases until the crystal is once again hexagonal (Figure 18e). The rest of the plot in Figure 17 behaves in much the same manner as described above.

We emphasize that the transitions that occur between Figure 18b and Figure 18d are sharp. In fact, at no point do the lattices in Fig. 18b and Figure 18d both appear simultaneously. Hence the line slip phase does not correspond to a coexistence of two crystals of differing orientation, but instead appears to be a distinct, stable structure. Indeed, we found helical defects identical to the one in Figure 18c in simulations with y-axis boundaries separated by several hundred particle diameters, as well as in simulations

with annealing schedules several orders of magnitude longer than those shown here. This observation suggests that the line slip phase is a minimum-free-energy state that is stabilized by the frustration. We re-examine this idea in the next section, where we develop a model to compare the energies of the line-slip and crystal phases.

Morse Potentials

We now turn to the results obtained with interaction potentials with shorter-range attraction. These results allow us to separate the roles of the commensurability constraint from those of the interaction potential assigned to the particles. Figure 19 shows the structures observed with the Morse potential with $\gamma d = 10$. The results are represented in the same (C/d, θ) plane as Figure 17. As in the Lennard-Jones case, we find regions of uniform crystal that correspond, in general, to oblique distortions of the hexagonal lattice indexed by (n_1, n_2). Transitions between crystalline and line-slip structures are as sharp here as in the Lennard-Jones case.

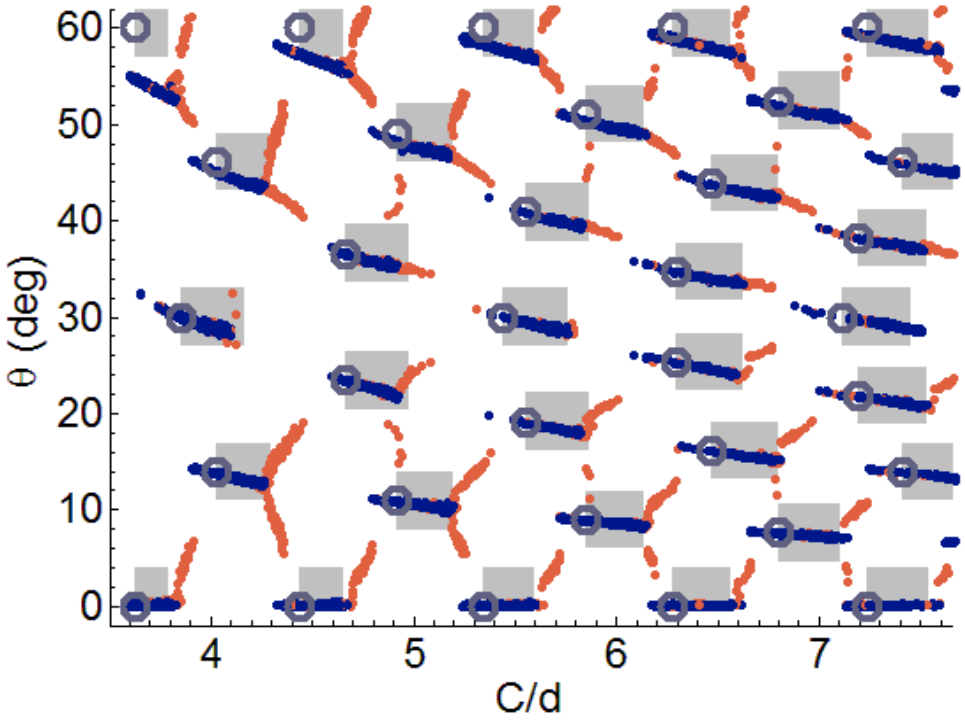

Figure 15. Steady state configurations observed in computer simulations using the Morse potential with γd=10. Red/gray data points represent a line-slip phase; blue/black data points represent continuous uniform crystals. The large circles label the analytically determined vales for C_0 as in Figure 15, and the gray blocks show defect-free regions as predicted by Eq. 19 and Eq. 21.

Unlike the Lennard-Jones case, however, we find that the line-slip structure supplants the crystal phase over a much broader region in parameter space. The reduced range of existence of a uniform crystal when $C < C_0$ might arise from the steeper repulsion of the Morse potential, as shown in Figure 9. Similarly, the reduced range of uniform crystals when $C > C_0$ may be caused by the shorter range of attraction. We return to this point below in the context of our model. Also note that, for the case of $C > C_0$, the defect regions branch off the islands of uniform crystals in opposite directions along the θ

axis. This effect is caused by the additional chirality of the line-slip seam (see Figure 18c), which is independent of the chirality of the lattice as a whole.

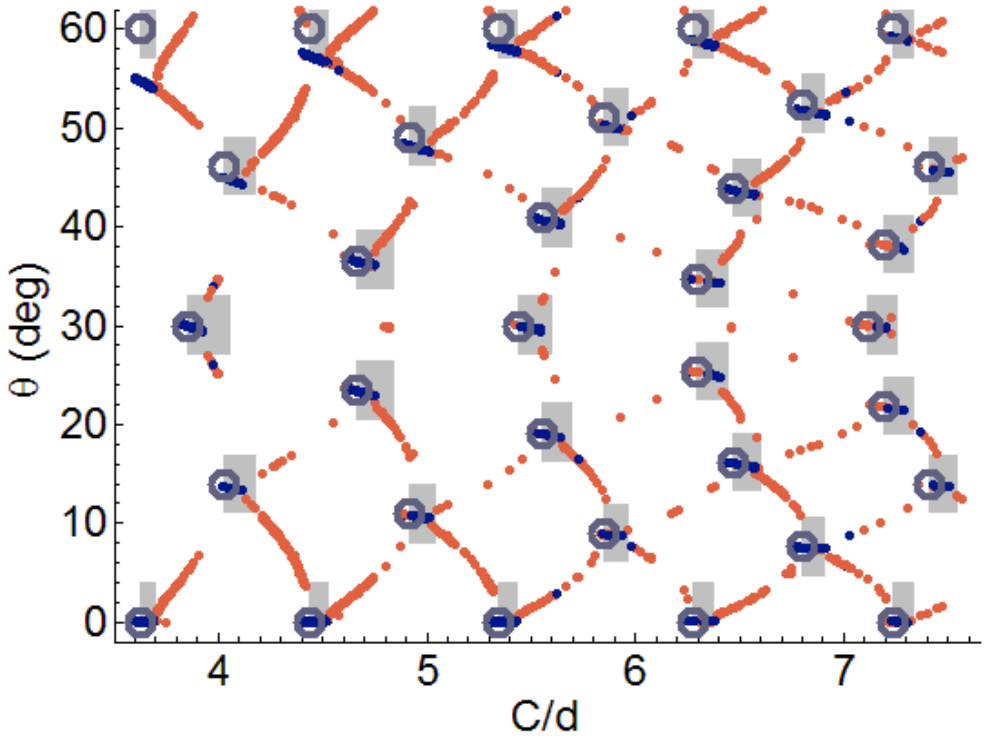

Figure 16. Steady state configurations observed in computer simulations using the Morse potential with γd=30. Red/gray data points represent a line-slip phase, and blue/black data points represent continuous uniform crystals. Here, the line-slip phase predominates.

For the still shorter-range attraction, we find a continued trend toward increased prevalence of the line-slip structure. Figure 20 shows the observed structures for the Morse potential with $\gamma d = 30$. Here, the line-slip states dominate the graph almost entirely and the uniform crystal phase is found only within narrow regions near $(C_0/d, \theta_0)$. More precisely, the range of circumferences for which we find either a compressed or dilated oblique lattice has been dramatically reduced from the $\gamma d = 10$ case. In order to

better explain this phenomenon, we now seek to develop a model that can predict where these transitions occur.

1-Dimensional model

We propose a simplified model that succeeds in describing the major findings of the simulations. Let us first consider some C_0/d for which the preferred lattice angle, θ_0, is 0° (i.e. $n_2 = 0$ and the particles are stacked in rings around the cylinder, as in Figure 21c). To further simplify the model, we will consider only a single one-dimensional ring of particles along $\boldsymbol{a}_1$ and work in the low-temperature limit where entropy is not dominant. If the ring's circumference is increased beyond C_0 and the particles are then allowed to rearrange themselves, one can imagine two possible configurations emerging: (a) all the particles are spread uniformly along the ring and share the extra distance, or (b) the particles cluster and move all of the added strain to a single pair (Fig. 21).

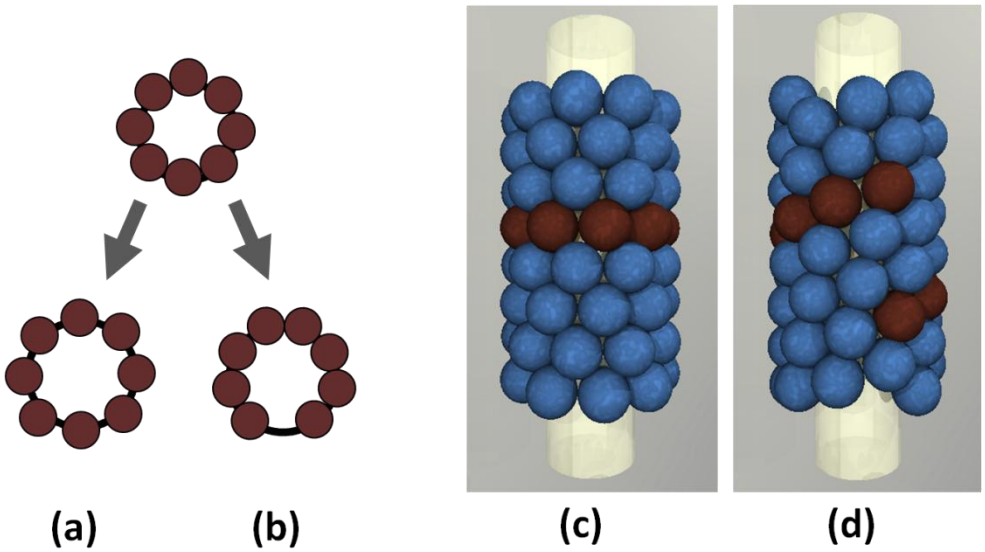

Figure 17. Explanation of the 1D model. Two plausible stable configurations occur when the densely packed particle ring (top) is expanded and extra space is introduced: either (a) the extra space is shared among all the particles equally, or (b) the extra space is focused into a single pair of particles and the rest remain touching. (c) A single 'ring' of particles is highlighted in red/black. (d) A single helical coil of particles is highlighted in red.

Ignoring all but nearest-neighbor interactions, we can write the total energy of these two configurations generically for some arbitrary short-range attractive potential $V(r)$;

$$E_{uniform} = N \cdot V(P/N) \quad \text{(Eq. 18a)}$$

$$E_{defect} = (N-1) \cdot V(d) + V(P - Nd + d) \quad \text{(Eq. 18b)}$$

where N is the number of particles in the ring, P is the perimeter of the polyhedron connecting the centers of the particles (defined above and in Figure 14c), and d is (as before) the location of the potential minima. When $E_{uniform}$ exceeds E_{defect}, each ring of particles on the cylinder will prefer to have a seam, and a uniform crystal lattice will no longer be stable. The critical P for which this transition occurs can be found by simply equating these two energies.

We can extend this approach to any value of θ by generalizing the ring to a segment of a helix that extends 2π along $\hat{\varphi}$ (Fig. 21d). This can be done approximately by replacing P with $P/\cos\theta_0$ and letting $N = P_0/(d\cos\theta_0)$, with P_0 and θ_0 being the un-stretched values. Using these substitutions, we equate Eqs. 18a and 18b, and rearrange slightly to find

$$\left(\frac{P_0/d}{cos\,\theta_0} - 1\right) \cdot V(d) = \frac{P_0/d}{cos\,\theta_0} \cdot V\left(\frac{P}{P_0}d\right) - V\left(\frac{P}{cos\,\theta_0} - \frac{P_0}{cos\,\theta_0} + d\right), \quad \text{(Eq. 19)}$$

where

$$\cos\theta_0 = (n_1 + n_2/2)/\sqrt{{n_1}^2 + n_1 n_2 + {n_2}^2} \ . \qquad \text{(Eq. 20)}$$

As the left side of Eq. 19 is a constant, the critical distance P can be solved computationally for any generic attractive potential $V(r)$, and the circumference C can be subsequently approximated from P via the relation

$$C \approx \pi d/\sin(\pi d/P). \qquad \text{(Eq. 21)}$$

This approximation is derived using the assumption that P is a regular polygon, and hence it is accurate when $\theta = 0°$ or 60° and when $P >> d$. It is also worth noting that, in the case of the Morse potential (Eq. 8), the critical value of C is determined by the parameter γd (which sets the range of the potential) in addition to (n_1,n_2).

The results of these calculations are represented by the grey bars in the backgrounds of Figs. 18, 19, and 20. Calculated for all relevant combinations of n_1 and n_2, these bars each begin at C_0 (found via Eq. 16), and terminate at the C that marks the expected onset of line-slip defects. A comparison with the simulation data shows good agreement. When C/d is expanded beyond the ideal hexagonal value (C_0/d), in almost all cases the line-slip phases appear where Eq. 19 predicts. Additionally, much of the error in these predictions for low values of C/d is a product of the approximation used in Eq. 21; future work could improve the accuracy by instead numerically finding C from P using an exact trigonometric relation. When C/d is compressed *below* the perfect hexagonal value, however, the model predicts a line-slip phase for the Lennard-Jones potential, whereas simulations indicate that a crystal phase is stable under these conditions. This discrepancy is small when θ is close to 0° or 60°, but becomes significant when $\theta \approx 30°$. The source of the disagreement stems from a difficulty in applying our model to the type of transition in these regions; such a calculation requires an energetic comparison

between particles in the line-slip phase and particles in the compressed oblique phase, which are two configurations with different values of N and θ. For this reason, correctly predicting the critical values of C that correspond to the onset of a compressed oblique lattice may be more straightforward using a two-dimensional model instead.

Our model makes clear that as the range of attraction is decreased, the energy required to stretch the crystal lattice grows very quickly, and thus the line-slip phase is present within a greater percentage of the parameter space. As was stated previously, the extremely short-ranged $\gamma d = 30$ Morse potential exists almost solely in the line-slip regime. We further infer that the steepness of the core repulsion in the chosen interaction potential governs where in parameter space the line-slip phases terminate; that is, the point where a compressed oblique lattice becomes favorable energetically to the line-slip phase. Once again, however, this transition is poorly described by our model.

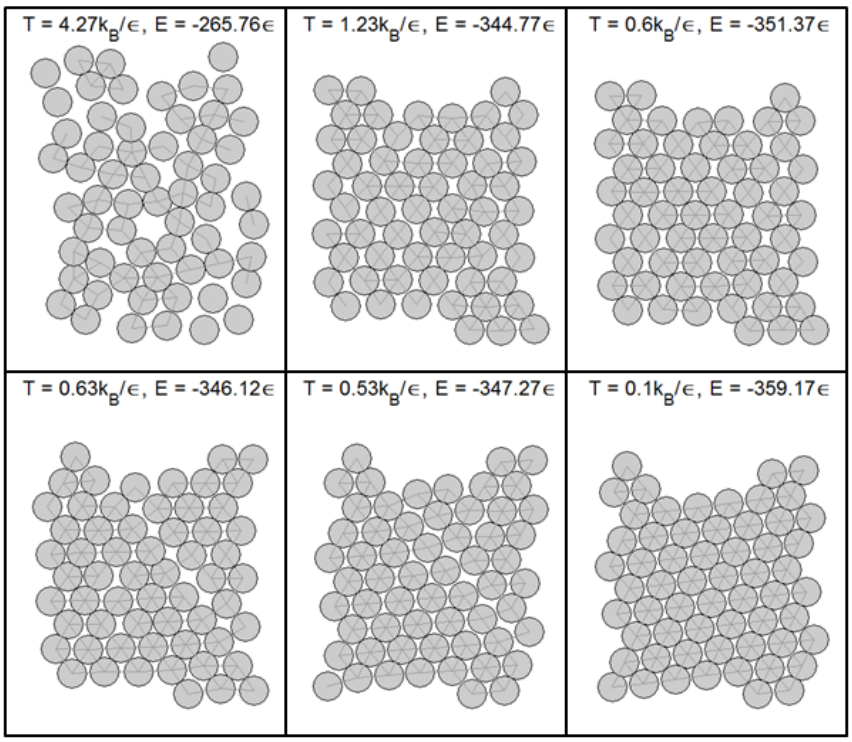

Figure 18. Cooling of Lennard-Jones particles at C/d=6.76 (the location of which is indicated by a star in Figure 17) into a stable crystal. The temperature and the energy, computed only from pairwise interactions, are indicated in each frame. Neighboring particles that are touching have been indicated with a bond. For clarity, bonds that cross the branch cut at $\phi=2\pi$ have not been added. As T is lowered, we find a (6,0) phase, a line-slip phase, and finally the steady-state (6,1) phase.

Lastly, we note that the presence of crystalline and line-slip phases in parameter space can affect the dynamics of crystallization as the system is cooled. As an example, Figure 22 shows images of one Lennard-Jones system undergoing freezing as the temperature is lowered. Here, the system first freezes into the (n_1,n_2) = (6,0) crystal with $\theta = 0^\circ$, but it is very highly stretched. As temperature is decreased, this crystal structure becomes unstable and is spontaneously replaced by the line-slip phase. At still lower temperatures, the line-slip transitions into a lower-energy crystalline configuration with (n_1,n_2) = (6,1), as indicated in Fig. 18 with a star. This sequence of phases may be in accord with Ostwald's rule of stages, which postulates that crystallization proceeds with multiple metastable crystalline states in order of decreasing free energy barrier.[9-11]

Conclusions

We have shown that, due to the constraints of the cylindrical geometry, at temperatures well below the planar-surface melting points (i.e. $k_BT << \epsilon$) an oblique crystal symmetry arises that is unstable on planar surfaces. We also find that a stable line-slip phase can form spontaneously within finite ranges of the cylinder circumference C, and that the regions in parameter space where line-slip phases are preferred broaden as the range of attraction is decreased. As direct evidence of this trend, our results indicate that the Lennard-Jones system favors the formation of oblique crystals, whereas the

comparatively short ranged Morse potential with $\gamma d = 30$ almost exclusively forms line-slip structures.

The primary features of this behavior are predicted by our straightforward one-dimensional model with reasonable accuracy. In particular, our results suggest that a line-slip phase can be energetically favorable for a variety of interaction potentials. It seems likely that more accurate analytical models of this problem could be developed, but the simplicity and transparency of our method allow it to be applied to other surface geometries and potentials.

In its current form, this model cannot be used to predict the behavior of purely repulsive or electrostatic interactions in this geometry without modification. One might assume, given the construction of Eq. 19, that a line-slip phase might never be energetically favorable for a repulsive potential. However, such a potential also has no inherent or preferred inter-particle spacing, and thus the optimal distance between the spheres should depend on the area fraction of spheres covering the cylinder surface. This complicates the problem since both $|\boldsymbol{a}_1|$ and $|\boldsymbol{a}_2|$ now vary, unlike the cases reported here where $|\boldsymbol{a}_2|/d \approx 1$ throughout. In the purely repulsive case, the area fraction provides a constraint that again reduces the problem to a single dimension if the lattice structure is known.

Our results may have broad implications for understanding the way tubular crystals assemble in nature. In particular, it has been pointed out that many biological materials exhibit the type of structure described here, and therefore the same commensurability constraint.[3,5,12] Because capsid proteins in helical viruses (*tobacco mosaic virus*, for example) are constrained to bind to the surface of a RNA strand, the

situation described here might be informative in understanding their structure. Microtubules also are capable of self-assembling with a seam–although in their case this seam is both purely longitudinal and achiral.[13] Nevertheless, such similarities are tantalizing enough to warrant further study. The straightforwardness of our predictions also suggest a practical application of these results as a novel method for producing crystalline media of desired symmetry and orientation on cylindrical surfaces. Specifically, one should be able to tune both the structure and orientation of a developing crystal lattice by adjusting the ratio C/d. Such crystals might spontaneously assemble more readily due to the existence of the line-slip phase, through which crystals that nucleate in a metastable structure can reorganize into a more stable configuration.

Finally, we note that the bending rigidity of the crystal along the cylinder axis may depend on the structure. Understanding how each of the different types of structures affect the stiffness of the overall material could be quite valuable, and will be the focus of study in the next chapter.

Notes

[1] The text in this chapter is based on a previous publication by Wood et al., which is listed in Note #2 below.

[2] D. A. Wood, C. D. Santangelo, and A. D. Dinsmore, Soft Matter **9,** 10016 (2013).

[3] R. O. Erickson, Science **181,** 705 (1973).

[4] K. L. Kohlstedt, G. Vernizzi, and M. Olvera de la Cruz, Physical Review E **80,** 051503 (2009).

[5] A. Luque and D. Reguera, Biophys J **98,** 2993 (2010).

[6] P. Prusinkiewicz and A. Lindenmayer, in *The Algorithmic Beauty of Plants* (Springer, 1990), p. 109.

[7] A. Mughal, H. Chan, D. Weaire, and S. Hutzler, Physical Review E **85** (2012).

[8] A. Mughal, H. Chan, and D. Weaire, Physical Review Letters **106** (2011).

[9] V. J. Anderson and H. N. W. Lekkerkerker, Nature **416,** 811 (2002).

[10] J. W. Cahn, Journal of the American Ceramic Society **52,** 118 (1969).

[11] P. Rein ten Wolde and D. Frenkel, Physical Chemistry Chemical Physics **1,** 2191 (1999).

[12] W. F. Harris and R. O. Erickson, J Theor Biol **83,** 215 (1980).

[13] M. Kikkawa, T. Ishikawa, T. Nakata, T. Wakabayashi, and N. Hirokawa, J Cell Biol **127,** 1965 (1994).

CHAPTER 4

STIFFNESS OF CYLINDRICAL CRYSTALS

Having demonstrated that the crystalline structure of a crystal on a cylinder is largely determined by the circumference *C* of the underlying crystal, we now seek to understand the mechanical properties of these different structures. We used MD simulations to map the way that the bending elasticity of a cylindrical crystal depends on the circumference, the interactions between the particles, the crystallographic angle θ, and the overall type of crystal lattice (i.e. hexagonal, stretched oblique, line-slip).

Notably, we found that thin cylindrical crystals have a lower Young's Modulus than large ones; this is unusual because material properties typically do not depend on the physical size of the object. We showed that the increase in elastic modulus is an intuitive consequence of the geometric arrangement of the particles in the crystal. We also provide evidence suggesting this phenomenon occurs in physically realized cylindrical crystals, such as carbon nanotubes.

In this chapter, we first give an overview of our MD simulations, then detail the results for perfect hexagonal lattices ($C = C_0$). We then derive a simple model for the stiffness of a cylinder that provides excellent agreement with our simulations, and comment on the range for which our theory is applicable. Next, we give an overview of the stiffness of cylindrical crystals with oblique and line-slip lattice structures; we found that the stiffness of these crystals is largely determined by the same geometric factors that contribute to the stiffness of lattices in a hexagonal configuration. We then give a brief explanation of the nonlinear phenomena observed when bending a line-slip lattice.

Theory and simulations

Calculating the stiffness of a cylinder

We first seek to define an expression relating the stiffness (or Youngs Modulus, $Y^{(2D)}$) with measurable quantities such as the shape or energy of the configuration of particles that can be extracted from simulations. The first step in this process is to derive the displacement field u_i, which is a vector field used to describe the effects of deformation on a solid body. In our case, the displacement field vector specifies the coordinates of each point on the bent cylinder, $[x_{bent}, y_{bent}, z_{bent}]$, in reference to its original position on the unbent cylinder, $[x, y, z]$. Or in other words, $[x_{bent}, y_{bent}, z_{bent}] = [u_x+x, u_{y+}y, u_z+z]$.

For a simple rod that has been deformed via pure bending, the components of the displacement field (u_i) of a cylinder of radius r bent axially to a curvature of $1/R$ are

$$u_x = \sigma \frac{xy}{R}, \qquad \text{(Eq. 22a)}$$

$$u_y = (R - y)\left(1 - \cos\frac{z}{R}\right) - \sigma \frac{x^2 - y^2}{2R}, \qquad \text{(Eq. 22b)}$$

$$u_z = (R - y)\left(\sin\frac{z}{R}\right). \qquad \text{(Eq. 22c)}$$

where σ is Poisson's ratio of the cylinder material. (A more approximate derivation of this function is contained in Landau *et al.*,[1] pg 65.) Indeed, the cross sectional area of the cylinder –one of the only parameters which dictate the structure of the lattice– varies with σ.

We are interested only in pure bending, and not on the properties of the underlying rod. Also, we would prefer not to conflate the effects of bending with radial stretching in these experiments, purely for reasons of clarity in identifying the role of particle structure on the bending stiffness. We can achieve both of these goals by setting the Poisson ratio of the rod equal to zero, meaning the axial stress due to bending causes no radial strain. In addition to isolating the physical mechanism we are interested in studying, this assumption vastly simplifies both the problem and our analysis; it maintains the cylinder radius during bending, and also avoids any buckling in regions of the cylinder with high Gaussian curvature: the cross section of the surface remains perfectly circular.

Applying continuum mechanical analysis, we next solve for the energy of an ideal cylindrical shell as a function of the curvature $1/R$ using the displacement field defined above (Eq. 22) and assuming $\sigma = 0$. We find that the energy per unit area at a given point on the bent cylinder surface, e, is

$$e = \frac{1}{2} Y^{(2D)} \left(\frac{y^2}{2R^2} - \frac{y}{R} \right)^2 . \qquad \text{(Eq. 23)}$$

Integrating this result around the circumference of the cylinder, we find that the average total energy per unit area on the lattice is

$$E/CL = Y^{2D} \left[\frac{C^2}{(4\pi R)^2} + \frac{3}{4} \frac{C^4}{(4\pi R)^4} \right] \qquad \text{(Eq. 24)}$$

This expression, along with our simulation data, can be used to solve for the bending energy of the lattice. Finding the steady-state energy of the crystal lattice on the surface of a cylinder requires knowing the energy as a function of the curvature of the cylinder.

Thus, in our simulations, we applied a curvature $1/R$ to a cylindrical lattice of particles, and then calculated the total energy of the resulting configuration. With this data, we applied Eq. 24 to solve for the Young's modulus of the material. To compute the total energy of the material, we sum the interaction energies of each pair of particles; $E = \frac{1}{2}\sum_{i \neq j} V\left(\left|\vec{r}_i - \vec{r}_j\right|\right)$.

Additionally, since $(C/R)^4$ will be extremely small compared to $(C/R)^2$ in virtually all of our simulations, we can essentially plot the energy vs. $1/R^2$, and the derivative of this plot will be proportional to the bending modulus $Y^{(2D)}$, the quantity we care about.

MD Simulations

Using molecular dynamics (MD) simulations in LAMMPS,[2] we consider the problem of spherical particles of diameter *d*, which are constrained to lie on the surface of a bent cylinder of fixed circumference *C*. Here we provide a brief summary of the simulation protocols; details may be found in Chapter 2. The particles interact with one another *via* isotropic interactions, either the Lennard-Jones (LJ) or Morse potentials (Figure 9). Again, for both potentials, the energy reaches a minimum of $-\epsilon$ when $r = d$, so that *d* is the effective particle diameter (Eq. 7-8).

Simulations begin at temperature $T=2k_B/\epsilon$ with particles at randomized positions within the 3D simulation volume, and then a large spring force was applied to the particles to confine them to the surface of a cylinder while allowing them to move freely on the surface (explained in detail in Chapter 2). The system is then cooled to $T = 0.1k_B/\epsilon$ over a period of 10^6 iterations, and the positions of the particles are then recorded. We

define the length L as the total length along the curved axis of the cylinder. For the simulations reported here, L ranged from 20d to 200d.

We then deform the cylindrical rod into an arc of radius R (curvature 1/R) while maintaining a perfectly circular cross section without buckling. The curvature of the rod is set to 10^{-6} at the start of each simulation, then incremented slightly, and the particles are allowed to reach a new steady configuration. The steady-state particle positions are then recorded and the total energy (E) of the bonds is calculated.

Using the calculated energy E and curvature 1/R, we can use Equation 24 to solve for the stiffness $Y^{(2D)}$ of the cylindrical crystal in our simulation. By finding the stiffness for a wide variety of crystals with different interactions, circumferences, and lattice structures we can use this method to map out how the elasticity is determined by these properties.

Triangulating Neighbors

In order to analyze the 3-dimensional data generated by the simulations, it was useful to reduce the dimensionality of the problem by projecting our data onto a 2-dimensional manifold. Triangulating neighbors is difficult to do on a curved 2D surface embedded in 3D space, but this information is quite useful for locating defects in the crystal and calculating configurational energies. To perform this projection, the 3D coordinates of the particles were projected into the coordinates represented by the surface of the cylinder, $[x, y, z] \rightarrow [r_b, \vartheta_b, z_b]$. These coordinates are identical to the ones used to calculate the force-field constraining the particles onto the cylinder outlined in Chapter 2 (Figure 12). Because the value of r_b is the same for every particle (and is equal to the

radius of the cylinder), it does not contain useful information and can be ignored, effectively reducing the dimensionality of the coordinates from 3D to 2D. The projection was done using the following mathematical transformation:

$$b = (z^2+(R-y)^2)^{1/2} \quad \text{(Eq. 25a)}$$

$$z_b = (y-R*z/b)^2 \quad \text{(Eq. 25b)}$$

$$y_b = (y-R*(1-(R-y/b))*\text{sign}(R-y), \quad \text{(Eq. 25c)}$$

and then

$$r_b = (x^2+y_b^2+z_b^2)^{1/2} \quad \text{(Eq. 26a)}$$

$$z_b = R*\arctan(z/(R-y)) \quad \text{(Eq. 26b)}$$

$$\vartheta_b = (C/2\pi)*\arccos(x/r_b)*\text{sign}(y_b) + C/2 \quad \text{(Eq. 26c)}$$

where R is the radius of curvature of the cylinder, and C is the circumference of the cylinder. Additionally, sign(x) is a function that returns 1 when x is positive and -1 when x is negative. Once projected onto the 2D manifold, neighbors were found by using a Delaunay triangulation.

Results: Hexagonal Lattices

We show first the energy *vs*. curvature of hexagonal lattices where one crystal lattice vector lies along the azimuthal direction of the cylinder, denoted as [n,0] configuration using the phylotactic indexing described in Chapter 3 (this arrangement is also referred to as an "armchair" configuration in nanotube-related literature). These lattices appear when an integer number (n) of spheres exactly fits around the circumference, which occurs when $C = C_0$, or in other words when $C/d = \pi/\sin(\pi/n)$.[3]

Dependence of stiffness on *C* and V(r)

Figure 23 shows the results for the case of n=5 and a Morse potential with γd = 20. The energy E is divided by the surface area of the crystal ($L \times C$). For small curvature, the bending energy increases linearly with $(1/R)^2$. Moreover, we find that the bending energy is indistinguishable for increasing or decreasing curvature: the process is reversible. Hence this regime corresponds to a linear response, as expected from the fact that the displacements of the particles are << d, so that the interactions between the particles are approximately Hookean.

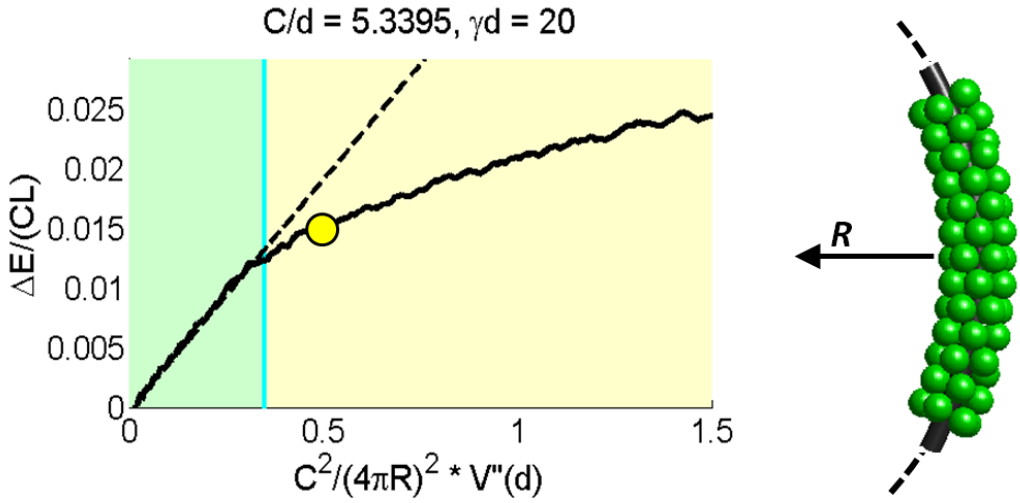

Figure 19. Bending energy (Eq. 27) versus curvature for a cylinder with n=5, and a Morse potential with γd = 20. The slope of this plot is the stiffness of the cylinder, $Y^{(2D)}$. For low curvatures, bending energy increases linearly with curvature and the stiffness is constant (teal region); for high curvatures the stiffness slowly decreases with increasing curvature (yellow region). The highlighted point is rendered on the right, and the radius of curvature is labeled.

In the small-deformation limit of continuum elasticity theory, the elastic energy of a uniformly bent cylindrical shell (Equation 24) reduces to [1]

$$E/CL = Y^{(2D)} [C^2/(4\pi R)^2 + O(R^{-4})], \quad \text{(Eq. 27)}$$

where E/CL is the elastic energy per surface area of the crystal and $Y^{(2D)}$ is the Young's modulus of the 2D material. (The three-dimensional quantity is ill-defined for a monolayer[4].)

Guided by the continuum theory, we obtained $Y^{(2D)}$ for each cylindrical crystal by a linear fit to obtain the slope of E/CL vs. $C^2/(4\pi R)^2$. In order to find the most accurate fit to this data, we used the following procedure. To find the best-fit slope to the linear region of the $E/(CL)$ plots, we started by finding the best linear fit to the first 100 data points, and recorded the mean squared error in this fit. We then incrementally added more data points to the fit, continuing to record the new slope of the fit and the mean-squared error. As more data points were added, eventually data points from the nonlinear regime were included in the fit, and the error in each fit increased dramatically. Once the cumulative error in any fit exceeded 5%, the process was terminated; then, the linear fit that included the most number of data points without exceeding a cumulative error of 0.01% was chosen as the best.

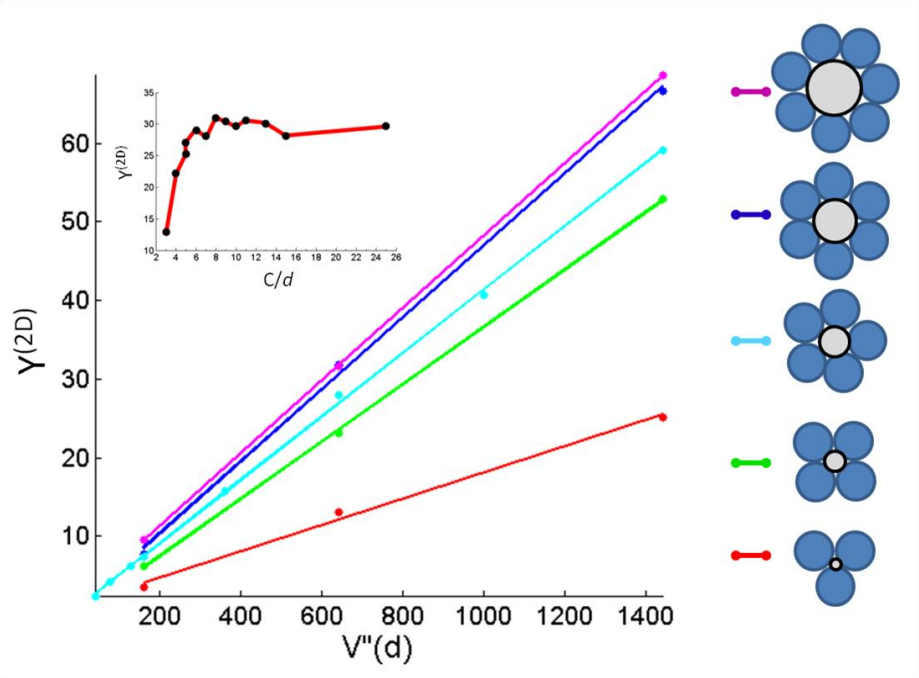

Figure 20. The 2D Young's modulus $Y^{(2D)}$ vs. $V''(d)$ in the $[n,0]$ configuration and for various circumferences C, obtained from bending simulations. We also plot $Y^{(2D)}$ versus C/d for the case of Morse particles with $\gamma d = 20$ (inset).

To improve and examine the accuracy of our data, we also used a purely numerical approach to determine $Y^{(2D)}$ in this linear elastic regime: the initial particle positions (at zero curvature) were numerically projected onto a rod with an infinitesimally higher curvature, the energy E was calculated, and the process was repeated for larger curvature. The dashed line in Figure 23 was computed using this method and it agrees with the best-fit slope to the linear region of our simulation within 5% error. Figure 24 shows the resulting $Y^{(2D)}$ against $V''(d)$ for several different interaction potentials and circumferences C (inset). For any given C, the modulus scales with $V''(d)$ as expected for small deformations.

Following the same procedure but starting instead with a perfect hexagonal lattice (removing thermal fluctuations entirely) reveals the underlying trend in the data. The numeric data in Figure 25 was computed using this method.

We next seek to quantify the diameter dependence of the stiffness on the crystal. Figure 25 shows how the measured $Y^{(2D)}$ varies with C/d. For large C, $Y^{(2D)}$ approaches the continuum limit of a 2D sheet, which is approximately given by $Y^{(2D)} = \frac{3\sqrt{3}}{4} V''(d)$.[4]

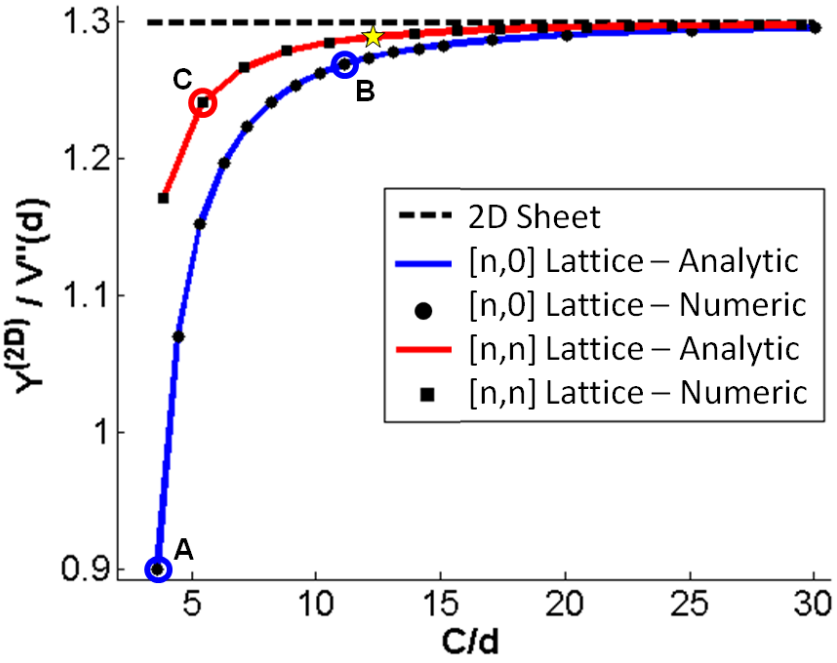

Figure 21. $Y^{(2D)}/V''(d)$ vs. C/d for two different crystal orientations. These data were extracted from numerical calculations of bending. The highlighted data points correspond to the configurations illustrated in Figure 26, and the location of the gold star approximately corresponds to the lattice structure of a microtubule.

Surprisingly, the data show that $Y^{(2D)}$ decreases sharply as C/d approaches 1. We emphasize that this is not simply the expected reduction of bending stiffness of a cylinder

as its circumference is reduced; that effect is accounted for by the C^2 scaling in Equation 27. On the contrary, continuum elasticity generally assumes that the modulus is independent of sample size and shape. Evidently, the small cylinder circumference reduces the bending stiffness much more than predicted by continuum mechanics. The modulus is reduced by as much as 30% when n = 4 and remains noticeably less than the continuum value even when n = 20. This reduction of $Y^{(2D)}$ is robust: we find the same results for particles interacting under Morse potentials with γd=[1-100] as well as the Lennard-Jones potential.

Interestingly, a similar result has been found for carbon nanotubes. As indicated in Figure 3, single-walled carbon nanotubes have repeatedly been demonstrated to possess the same decrease in Young's modulus as the diameter of the nanotubes is reduced. The high degree of similarity between our results in Figure 25 and the results found from detailed simulations of carbon nanotubes in Figure 3 suggests that the physical mechanism behind the softening phenomenon may be the same for both of these cases. Thus, forming a better understanding of our simulation data may illuminate the cause of the same softening behavior in nanotubes.

Harmonic model for $Y^{(2D)}$

Since the continuum model cannot explain how $Y^{(2D)}$ values with C, we turn to a model with discrete particles connected by harmonic springs of stiffness $V''(d)$. One can show that for a cylindrical crystal

$$Y^{(2D)} = \frac{1}{2} V''(d) \left(\frac{Nd^2}{CL}\right) \sum_{i=N.N.} (\hat{r}_i \cdot \hat{z})^4, \qquad \text{(Eq. 27)}$$

where N is the total number of particles in the crystal and CL is the total surface area of the crystal. The index i extends over all nearest neighbors of any particle in the lattice, with $\hat{r}_i$ being the unit vector between the particle and its i^{th} neighbor and $\hat{z}$ being the unit vector along the axis of the cylinder.

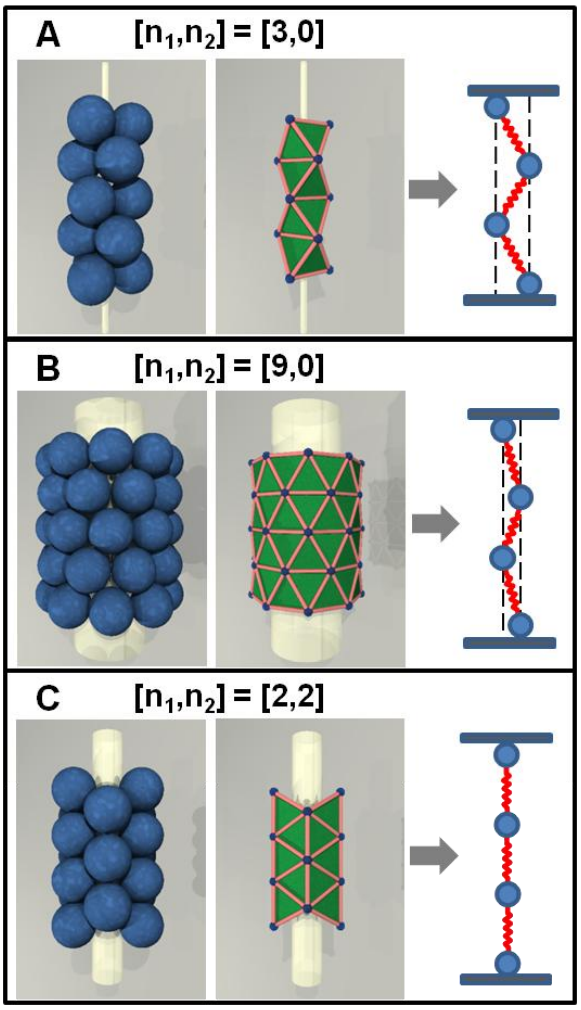

Figure 22. Image sequence showing the particle configuration, network of inter-particle bonds, and an approximate 1D ball-and-spring model of the profile of the crystal. Shown for two [*n*,0] crystals with different radii (*n*=3 and *n*=9), it illustrates that the strain on the inter-particle bonds is not equal to the strain along the cylinder axis. In a [*n*,*n*] configuration, however, the vertical component of the bonds between neighboring particles have no diameter dependence, and thus the axial strain is the same regardless of the size of the crystal.

Equation 22 predicts two mechanisms for the softening of $Y^{(2D)}$. The first contribution is the factor Nd^2/CL, which accounts for the ratio of surface area of the discrete triangular facets defined by the inter-particle bonds and the area of the smooth cylindrical surface (Figure 26a,e). This ratio is $2/\sqrt{3}$ in the large-*C* limit, regardless of the crystallographic orientation. The second mechanism for the reduction of $Y^{(2D)}$ is a consequence of the geometric arrangement of the inter-particle springs in the small-*C* limit. For example, in the [*n*,0] lattices, the axial springs lie at an angle from the cylinder's surface (Figure 26a,b, center and right-hand columns). When considering a fixed displacement *dz* along the cylinder axis with a fixed azimuthal separation between particles (enforced by *C*), the change in spring length is less than *dz* and the effective spring constant is reduced. Accounting exactly for the known particle positions in the [*n*,0] configuration, eq. 22 becomes

$$Y^{(2D)} = \frac{2n}{\pi} V''(d) \cdot \sin\left(\frac{\pi}{n}\right)\left(1 - \frac{sin^2(\pi/2n)}{sin^2(\pi/n)}\right)^{3/2}, \qquad \text{(Eq. 28a)}$$

where $C_{n,0} = \pi d/\sin(\pi/n)$ and *n* is any integer ≥ 3. This equation is shown by the blue curve in Figure 25.

On the other hand, the [*n*,*n*] configurations have one lattice vector along the cylinder axis and the small circumference has less of an effect on $Y^{(2D)}$. For this case, the exact form of Eq. 27 is

$$Y^{(2D)} = \frac{3\sqrt{3}\,n}{2\pi}\, V''(d) \cdot \sin\left(\frac{\pi}{2n}\right) \qquad \text{(Eq. 28b)}$$

and $C_{n,n} = (\sqrt{3}/2)\,\pi d/\sin(\pi/2n)$, where n is any integer ≥ 2. This equation is shown by the red curve in Figure 25. For both [n,0] and [n,n] crystallographic orientations, the analytical result is indistinguishable from the numerical results. The stiffness of a cylinder with any other crystallographic orientation [n_1,n_2] can thus be deduced in the same manner.

The limit of linear response

In every cylindrical crystal that we have investigated, the energy density increases linearly with $1/R^2$ for a finite range, beyond which the energy increases more slowly. For each system, we define a crossover value of curvature radius R_C, where E/L is no longer linear with R^{-2}. The measured value of R_C varies with C and with the form of the potential and the magnitude ϵ.

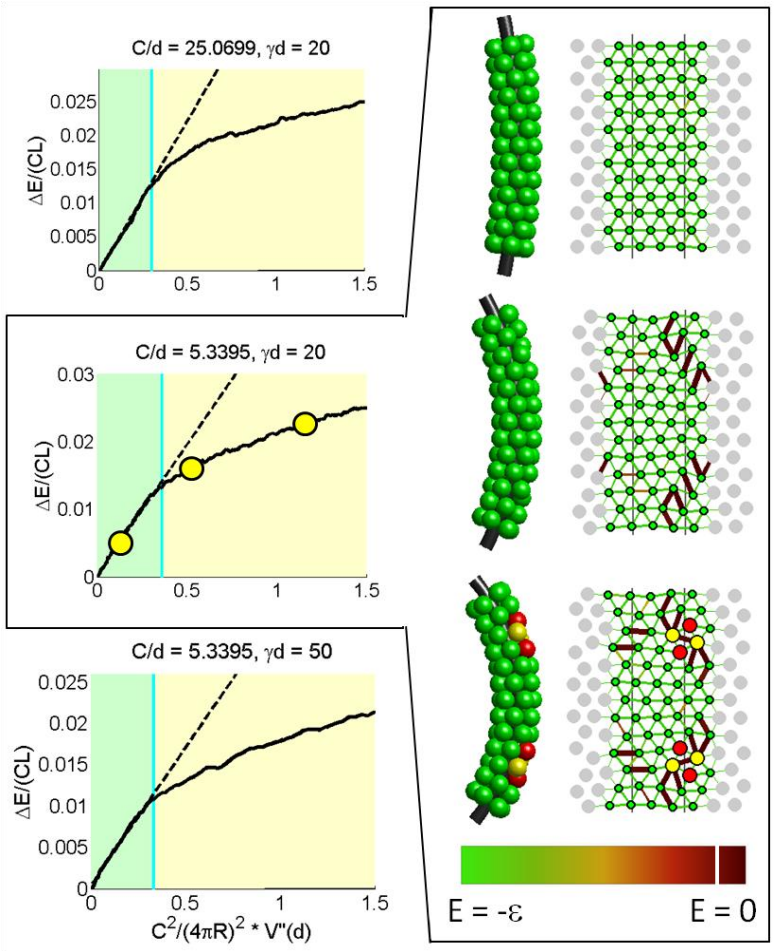

Figure 23. On the left, energy density is plotted as a function of the curvature squared for three different systems. In each of these plots, the linear regime ($R<R_c$) is indicated in green and the nonlinear bending regime ($R>R_c$) is indicated in yellow; the crossover between these two regimes is represented by a teal line. Though the circumference and interaction potential of these three systems are highly dissimilar, the response to bending in each scales identically. On the right, configurations of three different states of the center left plot are highlighted; in each, a 3D representation of the bent cylinder is shown alongside a Delaunay map of the particles. (The gray circles indicate particles on either side of the seam, which are copies of a colored particle.) The energy of each neighbor bond is indicated by its color according to the scale bar at the bottom of the figure; bonds exceeding an energy of 0.1ε are shown in bold. The appearance of regions of particles with these highly strained bonds coincide with the crossover curvature R_c. Dislocations (shown as red/yellow particles) do not appear until the system has reached a much higher curvature.

Remarkably, we find that the crossover to nonlinear response occurs at a consistent value of $[C^2d^2/R_c^2\, V''(d)/\epsilon]$ for every system we have simulated. Figure 27 shows the bending-energy curves for three examples that show a cross-over when $[C^2d^2/R_c^2\, V''(d)/\epsilon] = 8.5$. In these plots, a dashed line at this value separates the linear regions (green) from the nonlinear regions (yellow).

In all of these three cases, the crossover to nonlinear response coincides with the appearance of local regions of highly strained bonds on the outer surface of the curved cylinder (where the Gaussian curvature is most positive). We define highly-strained bonds as those whose energy exceeds -0.1ϵ, they are indicated in dark brown in Figure 27. If the curvature is then reduced, these defects disappear at the same crossover R_c.

Topological defects (dislocations) generally appear at higher curvature, especially for the shorter-range potentials, and therefore are not the cause of the nonlinear response. As long as no dislocations have appeared the structure returns to the original one when R_c^{-1} is returned to zero and the E/L curve is indistinguishable for increasing and decreasing curvatures. Hence, the cross-over to nonlinear behavior is apparently still within the regime of elastic response.

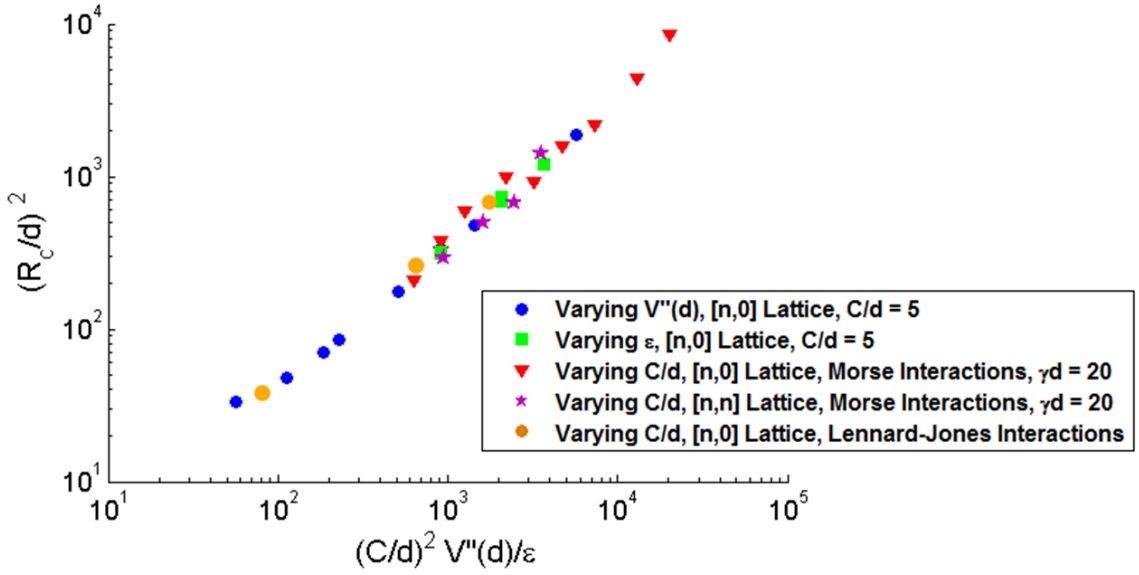

Figure 24. The curvature associated with the onset of nonlinear response, R_c, varies with the stiffness of the interaction potential, the strength of the interaction and the temperature of the simulation, the crystallographic orientation of the lattice, the diameter of the particles, and the size of the cylinder.

For a more comprehensive study of the crossover to nonlinear behavior, we defined the curvature at which we see a cross-over into nonlinear response, R_c, as the smallest curvature for which the simulation data deviates from the linear fit by more than 0.5%. Figure 28 shows the scaling of R_c when we vary either C, the range (V''(d)) or magnitude (ϵ) of the potential, or the lattice orientation. Although the numerical value of $[C^2d^2/R_c^2\, V''(d)/\epsilon] = 8.5$ is not understood, the scaling exponents are apparent from the geometry.

We next conjecture on the underlying cause of the nonlinear softening behavior. To do so, we first performed MD bending simulations on a [n,0] cylinder where the interactions between particles were perfectly harmonic; particles interacted only with their nearest-neighbors, and behaved as though they were bound by Hookean springs;

$$V(r) = \frac{\epsilon}{2} \cdot \left(\frac{r}{d} - 1\right)^2. \quad \text{(Eq. 30)}$$

This system is essentially identical to the ball-and-spring model used to calculate the analytical form of $Y^{(2D)}$. Interestingly, we found that although the stiffness of this cylinder matched the prediction from Equation 29a in the low-curvature limit, it did not exhibit any nonlinear softening behavior at higher curvatures. In other words, there was no crossover curvature R_c, and $Y^{(2D)}$ was constant throughout the simulation. This result is not entirely surprising, given that an identical model was used to derive our expression for $Y^{(2D)}$ in Equation 28; however, its complete lack of nonlinear behavior does imply that the shape of the interaction potential plays a key role in determining the crossover curvature R_c.

In particular, a key difference between harmonic interactions and the interaction potentials used in our simulations (Figure 9) is an infinite range, since Equation 30 has a positive curvature V"(r) > 0 for all r. Conversely, Equations 7 and 8 both possess an inflection point at V"(r_c) = 0; when r < r_c, V(r) curves upwards and is similar in shape to the harmonic potential, but when r > r_c, V(r) has negative curvature and approaches an asymptote of 0 rather than increasing infinitely. We propose that the appearance of localized strain (and, by extension, the decrease in $Y^{(2D)}$ at R_c) occurs when the average separation distance between particles in the lattice is greater than r_c.

Results: Oblique lattices and line-slip

We now examine the stiffness of cylindrical crystals with different types of lattice structures. Because of the commensurability constraint imposed by the cylindrical

geometry, the ultimate structure of the lattice is highly dependent on both C and the form of $V(r)$ (Figure 18). As explained in Chapter 3, a perfect hexagonal lattice is only achievable for discrete C; between these values exists a continuum of reduced-symmetry lattices, where the azimuthal crystal axis is uniformly lengthened or shortened in order to allow particles to fit evenly along the non-optimal circumference. Such a structure is not an unlikely configuration to find in nature— for example, due to the chemistry of C-C bonds in a carbon nanotube, the azimuthal strain in an unbent nanotube depends on its diameter.[5] Therefore, to build a more complete understanding of the stiffness of cylinders, we now seek to understand how the shape and structure of these lattices impact the stiffness of the overall colloidal crystal.

Linear elastic regime

Figure 29a shows the free energy of each of these types of lattices as a function of bending curvature squared. This data is representative of the stiffness of oblique and line-slip lattices regardless of the other parameters of the system. For different $V(r)$ or C, the found that the stiffness curve of a particular lattice structure varies in an identical manner to the trends reported in Figure 24 and Figure 25; the important parameter is the lattice spacing of the crystal along the azimuthal (stretched) axis.

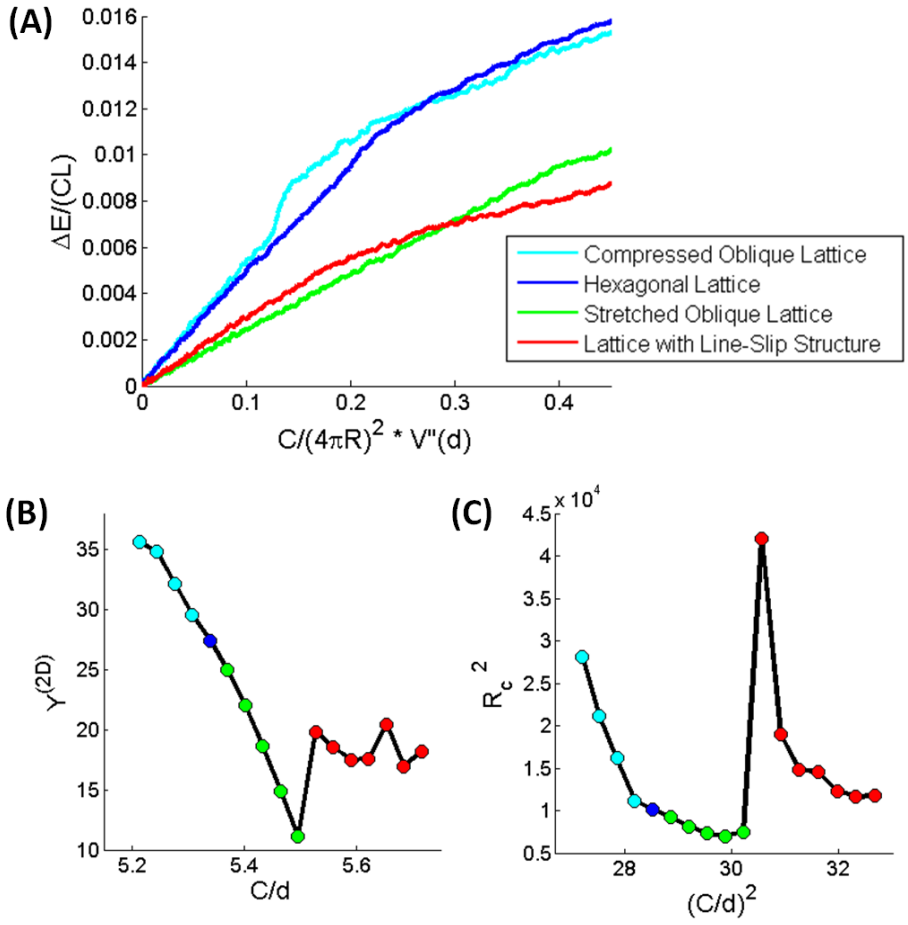

Figure 25. (A) Bending energy versus curvature for 4 different types of lattice structures, using a Morse potential with $\gamma d = 20$. (B) Bending stiffness $Y^{(2D)}$ as a function of the cylinder circumference. The different types of structures are colored identically to the curves in part A. (C) Crossover curvature R_c as a function of the cylinder circumference.

Figure 29b shows the modulus $Y^{(2D)}$ of the material as a function of C, with points being colored in the same manner as in Figure 29a. Starting with $C < C_0$, the particles form an oblique lattice that is compressed in the azimuthal direction. With increasing C, the lattice approaches the perfect hexagonal case and $Y^{(2D)}$ decreases. When the lattice becomes dilated in the azimuthal direction and $C > C_0$, the lattice continues to soften in a smooth trend. We then find a discontinuous increase in $Y^{(2D)}$ when the particles form a

line-slip structure. Here $Y^{(2D)}$ is approximately independent of C, which we attribute to the fact that expanding the rod changes only the packing within the helical defect, not the structure as a whole.

The softening of $Y^{(2D)}$ with fine changes in C is markedly different from the trend reported in Figure 25; the difference is because Figure 25 refers only to hexagonal lattices while Figure 29 shows the effect of distortions of the hexagonal lattice. The cause of these differences in $Y^{(2D)}$ originates from the structure of the material itself; the expression for the stiffness does not contain the C^2 dependence of the bending energy (as expected from continuum elasticity), and therefore exposes the effect due to the altered structure of the lattice.

To better understand this behavior, we returned to our harmonic ball-and-spring model for $Y^{(2D)}$ from the previous section (Equation 28). Once again, because $Y^{(2D)}$ is a constant as long as $R < R_c$, we can find $Y^{(2D)}$ by examining the region where the dimensionless curvature (C/R) is infinitesimally small; in this regime, pure bending is approximately equivalent to axisymmetric stretching, making our analysis much simpler.

According to Equation 28, the most significant contribution to $Y^{(2D)}$ is the axial component of the bonds between neighboring particles. As C/d is incrementally increased, the orientation of these bonds change slightly as the spacing of the lattice structure shifts to accommodate the increased surface area. We modified Equation X24 to account for these shifts in a [n,0] lattice, and found

$$Y^{(2D)} = \frac{2n}{\pi} V''(d) \cdot \sin\left(\frac{\pi}{n}\right)\left[1 - \left(\frac{sin^2(\pi/2n)}{\pi d}\right)\left(\frac{\pi d}{sin(\pi/n)} - \Delta\right)^2\right]^{3/2}, \qquad \text{(Eq. 31)}$$

where Δ is the change in the circumference, such that $C = C_0+\Delta$. A plot of this equation is below in Figure 30a. Hence, the softening effect from the oblique lattice can be explained

as a product of the same basic feature as the small-C_0 softening in Figure 25. Note, however, that the analytic result in Figure 30a is difficult to directly compare to the MD data in Figure 29b; Equation 31 essentially represents a zero-temperature limit, since it assumes the particles occupy a perfect lattice with perfect azimuthal symmetry.

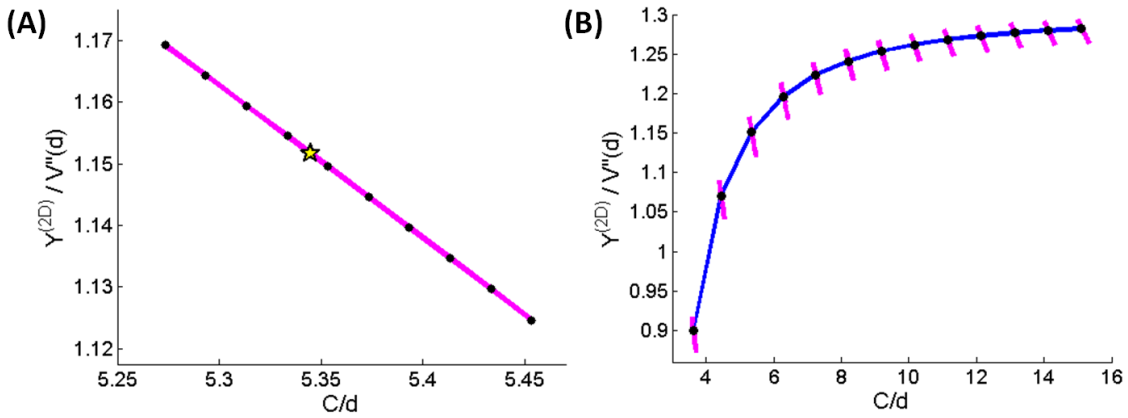

Figure 26. (A) The stiffness of oblique lattices around [5,0], over the range of circumferences found from Equation 19. The location of C_0 is indicated with a star. (B) Plot of $Y^{(2D)}$ for [n,0] lattice like Figure 25 (blue curve), but with the stiffness of oblique lattices at each circumference added (purple lines).

Considering that the range of each type of lattice was mapped out in the previous chapter (Figures 17-20), this provides a nearly complete picture of the linear elastic regime for all types of cylinders—which we calculated numerically for a [n,0] lattice and plotted in Figure 30b. These same calculations can be made for an arbitrary [n_1,n_2] lattice, and in principle the stiffness of virtually any allowable crystal lattice can be calculated.

Applying the same line of reasoning to the line-slip lattice, our bond-angle approach suggests that the stiffness should be essentially independent of the circumference, supporting our findings from Figure 29b. This is because the line-slip

phase resembles a perfect hexagonal lattice everywhere but the line-slip structure (regardless of C), and thus slightly increasing or decreasing the circumference does not appreciably change the average angles between neighboring bonds in the lattice. Note, however, that an exact analytical calculation of line-slip phases is likely to be prohibitively complex, since these lattices do not have azimuthal symmetry. Additionally, the line-slip phase exhibits an interesting phenomenon when it is bent which cannot be explained using our bond-angle analysis, which will be explained in the following section.

Line-slip migration

In the line-slip phase, the action at the crossover regime is particularly interesting, as the line-slip defect apparently interacts with the curvature of the bent rod; Figure 31 shows how the line slip structure is affected by bending in greater detail. In this figure, since the bonds between neighbors within the line-slip structure are necessarily stressed, the location of the structure is quite obvious.

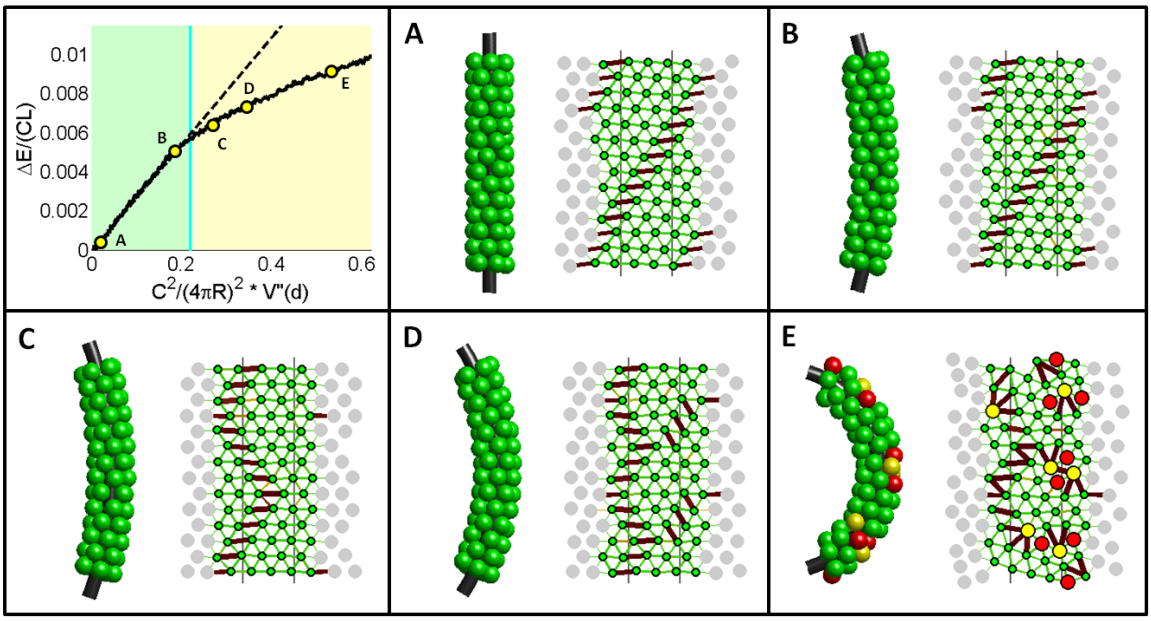

Figure 27. Migration of the line-slip structure towards the inner bend of the cylinder.

Figure 31b shows the configuration near the end of the linear elastic region, and Figure 31c shows the configuration near the beginning of the nonlinear elastic region. Once the applied curvature reaches a threshold value, the line-slip structure unwinds, forming a seam along the inner bend of the cylinder where the Gaussian curvature is the lowest. This transition decreases the bending elasticity of the cylinder, and occurs precisely at the crossover curvature that marks the end of the linear elastic region. As the curvature of the rod is increased, the seam tightens along the inner bend of the cylinder, and the 'wavelength' of the triangular pattern produced by the line-slip phase decreases. These structures are quite robust, repeating without error along even extremely long cylinders. This trend strongly indicates that the line-slip structure interacts with the Gaussian curvature of the curved rod.

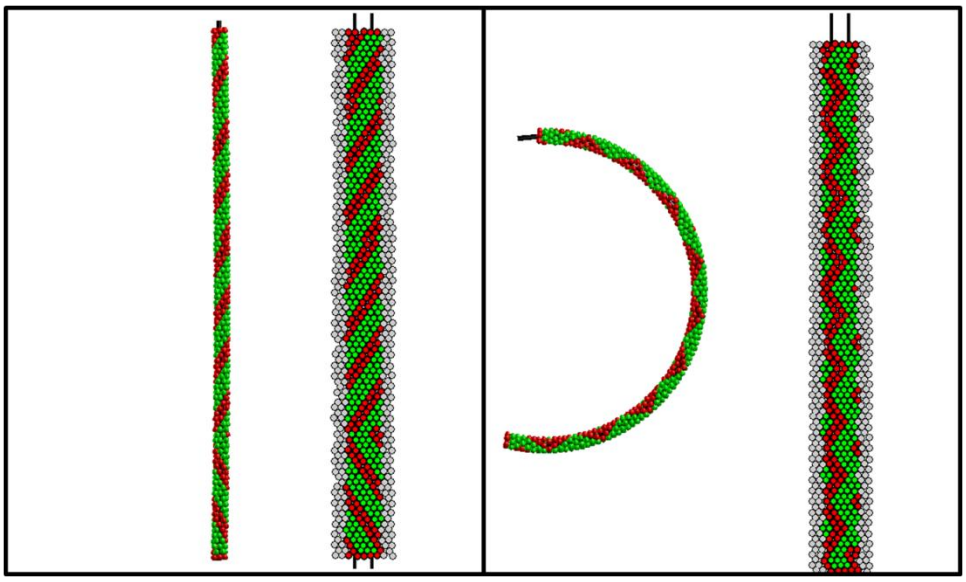

Figure 28. Line-slip migration on an extremely long cylinder. For clarity, the Delaunay map of the particles has not been added, and instead particles with azimuthally stressed bonds (i.e. particles included in the line-slip) have been colored red.

Conclusions

We have examined the relationship between the structure of a cylindrical crystal and its stiffness, $Y^{(2D)}$, and shown that this value is directly related to the geometric arrangement of particles in the constituent lattice.

We find that the relationship between $Y^{(2D)}$ and the circumference of the cylinder (Figure 25) directly parallels previous findings for the diameter-dependent stiffness of carbon nanotubes (Figure 3). Though formally the lattice of a carbon nanotube is a honeycomb configuration rather than hexagonal, the geometric arrangement of the bonds between neighboring particles in the lattice is identical, and the observed trend is the same. Though the source of this behavior has not been directly referenced in current

literature,[5-11] it seems likely that the physical origin of this phenomenon has a similar (if not identical) geometric explanation.

We next compare our results with the structure of a eukaryotic microtubule (Figure 2a). Formally, in terms of its lattice vectors, a microtubule has $[n_1, n_2] = [13, 3]$ structure,[12] which is very close to an $[n,0]$ arrangement (similar to Figure 26b). However, the structure of a microtubule lattice is not perfectly hexagonal, and also contains an achiral seam spanning the length of the tubule. Since each dimer is oriented parallel with the axis of the tubule, the lattice structure is ultimately much closer to a $[n,n]$ lattice (similar to Figure 26c); for context, this approximate structure is marked on Figure 25 with a gold star. This observation is actually quite interesting, since its configuration appears to be minimally affected by the softening effects outlined in this paper despite having a relatively small value for C/d. (Though it does not actually optimally minimize the ratio between $Y^{(2D)}$ and C/d.)

Additionally, although the stiffness of the smaller bacterial microtubules ($C/d \approx 5$) has not yet been measured, the data in this work suggests that these tubules should have a Young's modulus that is roughly 7% lower than the modulus of eukaryotic microtubules. Whether or not this difference in stiffness is biologically relevant is unclear at this point.

We next use our findings above to predict the threshold bending radius, R_c, for a microtubule. Since our above analysis suggests that $R_c = [C^2d^2/8.5\, V''(d)/\epsilon]^{1/2}$, and $C \approx$ 25 nm for a microtubule, we can compute R_c using the interaction potential $V(r)$ between individual tubulin dimers in the lattice. Several sources model this interaction as a Hookean spring potential (equivalent to the one used in Equation 24),[13,14] in which case $V''(d)/\epsilon = 1$, and $R_c = 42$ nm—a curvature so small that the tubule would surely buckle

before it could be bent so tightly. Other sources model these interactions as non-analytic protein-protein interactions,[15-17] in which case $V''(d)/\epsilon$ is very difficult to calculate. For the sake of comparison, if we imagine that $V''(d)/\epsilon \approx 300$ (a value that roughly corresponds to the stiffest potential we investigated in Chapter 3, a Morse potential with $\Upsilon d = 36$, as in Figure 20), then even still $R_c = 0.75$ μm.

Still, it may be possible to estimate reasonable upper bounds for R_c using the microtubule persistence length, which is well-known experimentally and directly related to Young's modulus, *Y*. The persistence length of a polymer is defined as the critical length at which the energy of thermal fluctuations match the bending energy of the material; for a microtubule this length is roughly 6 mm.[18,19] Thus we can set $E = k_BT$ in Eq. 27 when the microtubule length L = 6 mm, the radius of curvature is approximately R ≈ 5 mm, and its circumference is C = 25 nm, in order to find a rough approximation of $Y^{(2D)}$. Additionally, our results in Figure 25 suggest that the 2D Young's modulus for a microtubule is very close to the limiting value of $Y^{(2D)} = 3\sqrt{3}/4 \cdot V''(d)$, and thus we find that V"(d) is roughly equal to 300 J/m^2. From the scaling phenomenon illustrated in Figure 28, we estimate that the critical curvature where we expect nonlinear E/L scaling for a microtubule is about 20 μm. Notably, this value is an order of magnitude larger than the average radius of curvature of microtubule-loops observed by L. Liu *et al.*[20]

Notes

[1] L. D. Landau, E. M. Lifshit͡s, A. d. M. Kosevich, and L. P. Pitaevskiĭ, *Theory of elasticity*, 3rd English ed. (Pergamon Press, Oxford Oxfordshire ; New York, 1986).

[2] S. Plimpton, Journal of Computational Physics 117, 1 (1995).

[3] D. A. Wood, C. D. Santangelo, and A. D. Dinsmore, Soft Matter 9, 10016 (2013).

[4] M.-Q. Le, International Journal of Mechanics and Materials in Design 11, 15 (2014).

[5] E. Hernández, C. Goze, P. Bernier, and A. Rubio, Applied Physics A 68, 287 (1999).

[6] P. A. B. I. Yakobson, Carbon Nanotubes, Topics Appl. Phys 80, 287 (2001).

[7] T. Chang and H. Gao, Journal of the Mechanics and Physics of Solids 51, 1059 (2003).

[8] L. Jiang and W. Guo, Journal of the Mechanics and Physics of Solids 59, 1204 (2011).

[9] C. Li and T.-W. Chou, International Journal of Solids and Structures 40, 2487 (2003).

[10] A. E. Tanur, J. Wang, A. L. Reddy, D. N. Lamont, Y. K. Yap, and G. C. Walker, J Phys Chem B 117, 4618 (2013).

[11] J. R. Xiao, B. A. Gama, and J. W. Gillespie, International Journal of Solids and Structures 42, 3075 (2005).

[12] H. Sui and K. H. Downing, Structure 18, 1022.

[13] M. A. Deriu, S. Enemark, M. Soncini, F. M. Montevecchi, and A. Redaelli, Journal of Materials Science 42, 8864 (2007).

[14] V. VanBuren, L. Cassimeris, and D. J. Odde, Biophysical Journal 89, 2911 (2005).

[15] D. Sept and F. C. MacKintosh, Physical Review Letters 104 (2010).

[16] L. Jiang, Y. Gao, F. Mao, Z. Liu, and L. Lai, Proteins: Structure, Function, and Bioinformatics 46, 190 (2002).

[17] M. I. Molodtsov, E. A. Ermakova, E. E. Shnol, E. L. Grishchuk, J. R. McIntosh, and F. I. Ataullakhanov, Biophys J 88, 3167 (2005).

[18] M. Elbaum, D. Kuchnir Fygenson, and A. Libchaber, Physical Review Letters 76, 4078 (1996).

[19] M. Kikumoto, M. Kurachi, V. Tosa, and H. Tashiro, Biophysical Journal 90, 1687 (2006).

[20] L. Liu, E. Tuzel, and J. L. Ross, J Phys Condens Matter 23, 374104 (2011).

CHAPTER 5

VESICLE PREPARATION AND ANALYSIS TECHNIQUES

We now change the focus of this document to our work examining the effects of the adhesion of nanoparticles onto lipid bilayer vesicles. In this chapter, several methods for producing vesicles of are discussed in detail. This includes the electroformation method, which produces vesicles roughly 100 μm in diameter; the extrusion method, which produces vesicles roughly 100 nm in diameter; and the gentle hydration method, which produces a very high yield of vesicles. Additionally, methods for analyzing samples used throughout these experiments are detailed.

Vesicle Preparation

We chose lipids with unsaturated tails so that they remained in the liquid-disordered phase, and with different charges on the polar groups so that the average charge density could be tuned by composition. The majority lipid used in these experiments were 1,2-dioleoyl-*sn*-glycero-3-phosphocholine (DOPC), which has a nominally zwitterionic head group. However, measurements by Needham and co-workers showed that DOPC vesicles are slightly negative in charge (zeta potential –9 mV in 0.1 mM NaCl[1]), which is consistent with the nanoparticle-binding results reported in this thesis. To add a controlled amount of negative charge, we used 1,2-dioleoyl-*sn*-glycero-3-phospho-L-serine **(**DOPS), which has an anionic head group. Both types of lipid were purchased from Avanti Polar Lipids pre-dissolved in chloroform in ampoules, which were then diluted and stored under nitrogen in a -20º freezer for later use. Some

experiments used lipids derived from soy lecithin powder (Phospholipon 85G), which was ordered from the American Lecithin Company. These lipids have a phosphatidylcholine (PC) head group, but the fatty acid chains vary from one lipid to another.

Electroformation

This method produces giant unilamellar vesicles (GUVs) around 50-200 μm in diameter. This technique was first described by Angelova *et al*.,[2] and later adapted and studied in great detail by Herold et al.[3] First, glass microscope slides coated in indium tin oxide (ITO, from Delta Technologies, Part # CB-50IN-S111) are washed completely with acetone using a Kimwipe. Then, conductive copper tape (from 3M, sold by SPI, Part # 5012-AB) is placed along one edge of the conductive glass.

Next, the lipids being used to form the liposomes are mixed together in a small glass test tube. Each type of lipid being used is carefully added together in the vial; this mixture is then diluted with chloroform such that the total volume of liquid is around 50 μl. The vial is then mixed very thoroughly to ensure homogeneity of the resulting vesicles. Using a glass syringe, 25 μl of lipid solution is quickly and evenly spread out onto the conductive side of each glass slide. These slides are then placed under vacuum for at least two hours to remove all chloroform solvent from the ITO glass, leaving only lipids.

Next, a non-ionic solution must be prepared as a medium for electroformation of the liposomes. The experiments detailed in this document use a 175 mOsm sucrose solution and a 180 mM glucose solution. These concentrations were found to reliably

produce high-quality vesicles, but the relative concentration of these two solutions can be adjusted to tailor the osmotic pressure of the vesicles formed by this method.

Once the ITO glass slides have finished drying in the vacuum chamber, they can be removed. A layer of vacuum grease is applied to both sides of a Teflon spacer designed to fit between two ITO glass slides (custom made). This Teflon spacer has two holes opposite one another, designed to fit a 22 gauge needle tip. The ITO slides are pressed on opposite sides of the grease-lined Teflon spacer, with the lipid-covered sides of the ITO slides facing inwards. Binder clips are then placed around the slides to secure the cell. Using a 22 gauge syringe, 2 ml of 175 mOsm sucrose solution should be used to completely fill the interior of the cell with liquid, leaving no bubbles. Finally, a small bit of vacuum grease is then used to seal the 22 gauge holes in the Teflon spacer (Figure 33).

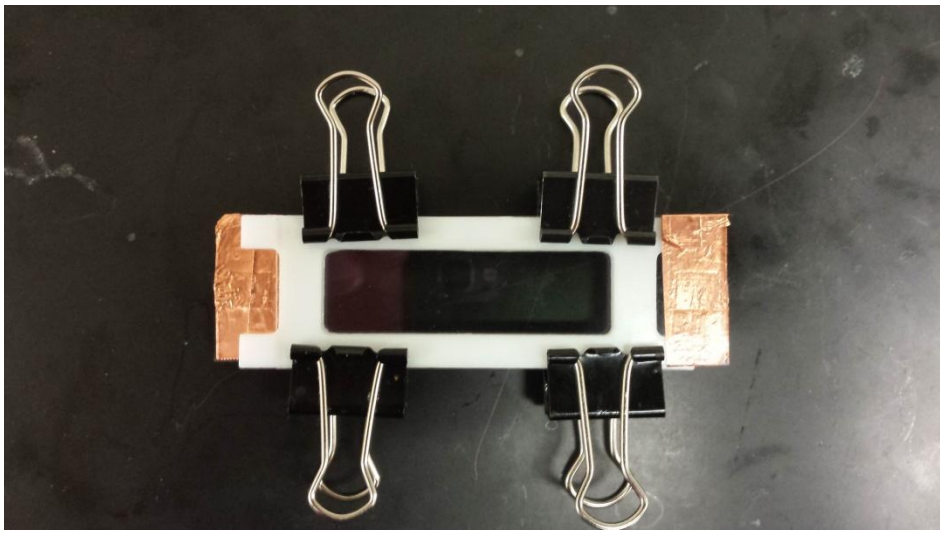

Figure 29. ITO glass slides with Teflon spacer, in completed configuration forming the electroformation cell.

Throughout this procedure, care should be taken to minimize exposure of the dried lipids on the ITO glass slide with air, in order to avoid oxidation of the lipids and ensure the highest quality of vesicles.

Once the cell has been sealed, it is placed in a 30-40ºC oven. Inside the oven, the copper adhesive should be used to connect the cell to a function generator using alligator clips; the function generator should be set at 2.4V peak-to-peak voltage, with a sine-wave oscillation at 10Hz. Vesicles are grown in solution in the cell over the course of two hours, at which point the cell must be removed from the oven. (Further time in the oven reduces the quality of vesicles.) The solution is then removed from the cell using a glass syringe, and the total volume of extracted liquid in the syringe is marked with sharpie once everything has been removed. The vesicle solution is then transferred to a glass vial.

To improve the visibility of the GUVs, make them heavy enough to sink to the bottom of the vial, and also to adjust the osmotic pressure (which is a desirable feature in our experiments, since the osmotic pressure affects nanoparticle binding), a 180 mOsm glucose solution is added to the sucrose vesicle solution extracted from the cell with a 1:1 ratio. This is done by filling the syringe to the point marked by sharpie in the previous step. The vesicles will remain stable for about a week, after which point more should be produced.

Finally, the ITO glass slides are cleaned by sonicating them in acetone for ten minutes, and then rinsing them with de-ionized H_2O.

Extrusion

This method produces large unilamellar vesicles (LUVs), of size 10-50 nm in diameter.[4]

First, a 25mL round-bottom flask should be rinsed with acetone and then quickly dried. Next, the lipids being used to form the liposomes are mixed together in chloroform solution inside the flask. Each type of lipid is carefully added to the flask, and then is diluted with chloroform such that the total volume of liquid is around 100 μL. The liquid in the flask is then mixed very thoroughly to ensure homogeneity of the resulting vesicles. Using a nitrogen tank, nitrogen gas is blown into the flask to evenly dry off the chloroform, while the flask is being gently turned by hand. The lipids should form an even film on the bottom of the flask. The flask is then placed under vacuum for at least two hours to ensure the complete removal of all the chloroform solvent.

After removal from vacuum, 1mL of 200 mOsm glucose solution is added to the flask, and the flask is then vortexed until the liquid appears milky white. This process forms a large quantity of multi-lamellar vesicles (MLVs), which can be forced through an extremely fine mesh filter to create unilamellar vesicles; the spacing of the mesh in the filter being used will determine the average diameter of the vesicles.

An extruder assembly (Avanti Polar Lipids) is prepared, with a polycarbonate membrane with 10 nm pores. The membrane is then placed between four filter supports (with two filters on each side), and two 1 mL syringes (one containing the MLVs) are attached opposite ends of the extruder assembly. The MLV suspension is passed back and forth through the membrane at least 15 times, at which point the liquid contains only

LUVs in suspension, and ought to look significantly less opaque than the initial MLV suspension.

The LUVs should then be placed in a glass vial, and kept in a 40º oven for 24 hours. Once removed, the LUVs will remain stable for up to two weeks. The size should be checked by dynamic light scattering. The procedure above generally results in LUVs with a diameter of 105 nm.[5]

Gentle Hydration

This method can be used to make very large quantities of GUVs using the lecithin-derived PC lipids, and was adapted from the methods described by Rodriguez et al.[6] First, 100 μL of PC lipid solution should be added into to a test tube. Then nitrogen gas is blown into the tube to evenly dry off the chloroform, while the tube is being gently turned by hand. The lipids should form an even film on the bottom of the tube. This entire process can then be repeated for multiple test tubes in order to increase the production of GUVs as needed.

The test tubes are then placed under vacuum for at least two hours to ensure the complete removal of all the chloroform solvent. Afterwards, 5 mL of 175 mOsm sucrose solution is then added to each individual test tube. These test tubes are then placed into a 35º oven for at least 24 hours. Make sure that the oven is sealed to avoid excessive evaporation.

Afterwards, when the tubes are removed, each one should contain a cloudy white formation suspended in the liquid (this is the vesicle suspension). The cloudy formation should be very gently removed from each test tube and deposited into a glass vial. Next, a

180 mOsm glucose solution is added to the extracted sucrose vesicle solution with a 1:1 ratio. The lecithin-derived GUVs should remain stable for about 4 days.

Vesicle Analysis Techniques

Throughout all of our experiments, the vesicles described above were exposed to cationic nanoparticles made by YiWei Lee and Li-Sheng Wang in Vincent Rotello's group. These nanoparticles have a 2 nm-diameter gold core, and are coated with cationic ligands. The ligands consist of a tetraethylene glycol linker with a cationic tetramethyl amine group; we refer to these ligands as TTMA for shorthand (Figure 34). The overall diameter of each nanoparticle is 7nm, and the stock nanoparticle solution was 10 mM of nanoparticles suspended in water. Several different specialized techniques were used to analyze the vesicle-nanoparticle complexes, and are detailed in this section.

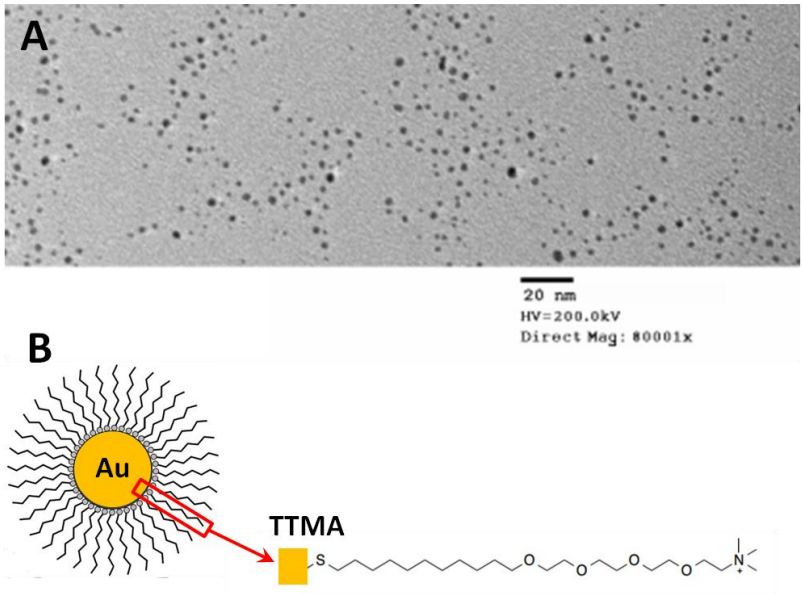

Figure 30. Illustration of the cationic Au-TTMA nanoparticles which will be used throughout the experiments in this chapter and the next. (A) An electron micrograph illustrating the size and uniformity of the nanoparticles. Only the gold cores of the nanoparticles are visible. Image taken by YiWei Lee. (B) A schematic of an individual nanoparticle, including an explicit illustration of the TTMA ligand.

LUV Sedimentation

LUVs with bound nanoparticles are both large and heavy, and easily sediment under centrifugation. First, a few microliters of 10 mM Au-TTMA nanoparticle stock are suspended in 200 mOsm glucose solution, then vortexed for 1 minute and sonicated for 3-5 minutes. Then, 15 µl of this stock is carefully added to 35 µl of LUVs suspended in 200 mOsm glucose solution, and then very gently agitated for at least two hours to ensure the nanoparticles have sufficiently bound to the LUVs and the system has equilibrated. Each sample is then centrifuged using a Labofuge 400 lab centrifuge (Heraeus Instruments) at 8000 RPM for 60 minutes.

After centrifugation, each sample contains a dense pellet of nanoparticle-laden LUVs. From this, 48 µL is carefully extracted (*i.e.* the supernatant) from each sample with a pipette and set aside separately. 6µL of de-ionized H_2O is added to the remaining 2 µL of solution with each pellet, and then each sample is sonicated for 5 minutes. The extracted supernatants are then dried in an oven until no liquid remains. Then, 8 µL of de-ionized H_2O is added to each one, and sonicated for 5 minutes. The concentration of nanoparticles in both the supernatant and the pellet can then be measured separately using a spectrometer.

UV-Vis Spectrometry

To measure nanoparticle concentration, a spectrometer was used (NanoVue UV-Vis Spectrometer, GM Healthcare). To read the absorbance spectrum of a sample, 2 µL of the sample is inserted into the device, and the resulting spectrum is saved to a computer via USB connection. This data can then be analyzed using MATLAB. In our case, we were interested specifically in algorithmically extracting the nanoparticle concentration from our absorbance data.

To extract nanoparticle concentration quantitatively, we first needed to measure individual absorbance spectra for the two primary species that comprised the samples in our measurements: pure nanoparticles, and hydrated lipids in a 180 mOsm glucose solution. To do so, we measured separate spectra for pure nanoparticle stock (10 mM Au-TTMA nanoparticles in deionized H_2O), and for rehydrated DOPC lipids in deionized H_2O (the same MLV suspension that is created before extruding LUVs).

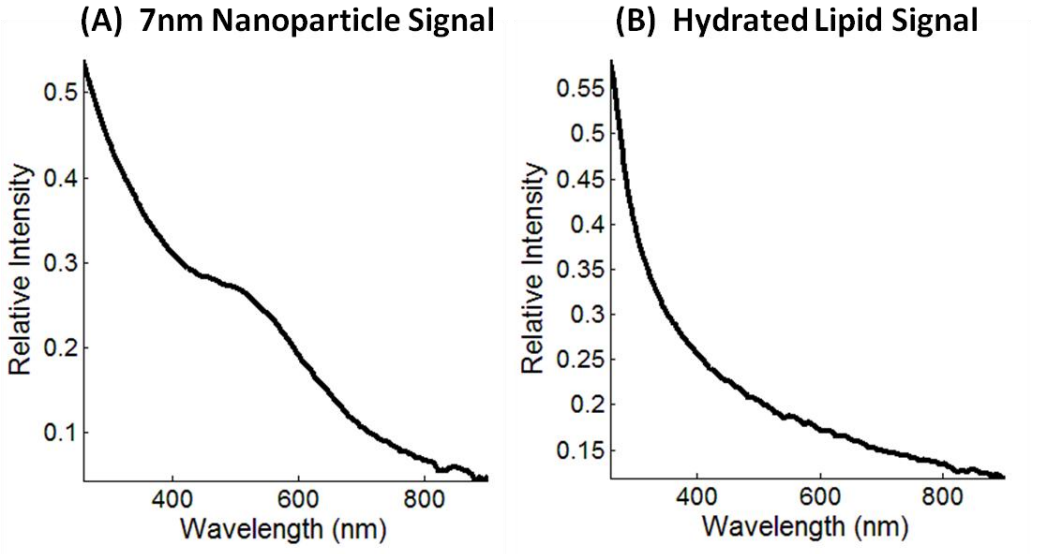

Figure 31. (A) Spectra for pure nanoparticles in water. Specifically, this data was taken from 2 μL of 10 mM Au-TTMA nanoparticles. (B) Spectra for hydrated and vortexed re-suspended lipid in deionized H_2O. The concentration of lipid in this sample is not critical; it is only important that these two signals can easily be distinguished.

The signal from the gold nanoparticles produces a characteristic 'hump' shape near 550 nm corresponding to the surface Plasmon resonance,[7] as evident in Figure 35a. This signal is distinguishable from the power-law decay comprising the signal from the lipids, corresponding to Rayleigh scattering and evident in Figure 35b. In principle, any sample we measure ought to contain a linear combination of the signals from these two characteristic sources. Thus, we can fit to the spectra of our samples by finding the optimal linear combination of these two source signals that best matches our measured sample spectra. What's more, since the intensity of signal from the nanoparticles directly corresponds to the concentration, the amplitude of the nanoparticle component of this best fit can be used to calculate the concentration of nanoparticles in the sample.

To verify the accuracy of this analysis method, we prepared a control sample containing both nanoparticles and lipids, in order to test whether or not our algorithm could correctly recover the concentration of nanoparticles in the sample. To make this sample, 1 μL of 10 mM nanoparticle stock was added to 4 μL of re-hydrated DOPC lipid, giving us a total nanoparticle concentration of 2 mM. This sample was vortexed for 1 minute, sonicated for 2 minutes, and then 2 μL was recorded using the spectrometer. The absorbance spectrum of the sample was then analyzed using the algorithm described above, and the results are shown below in Figure 36.

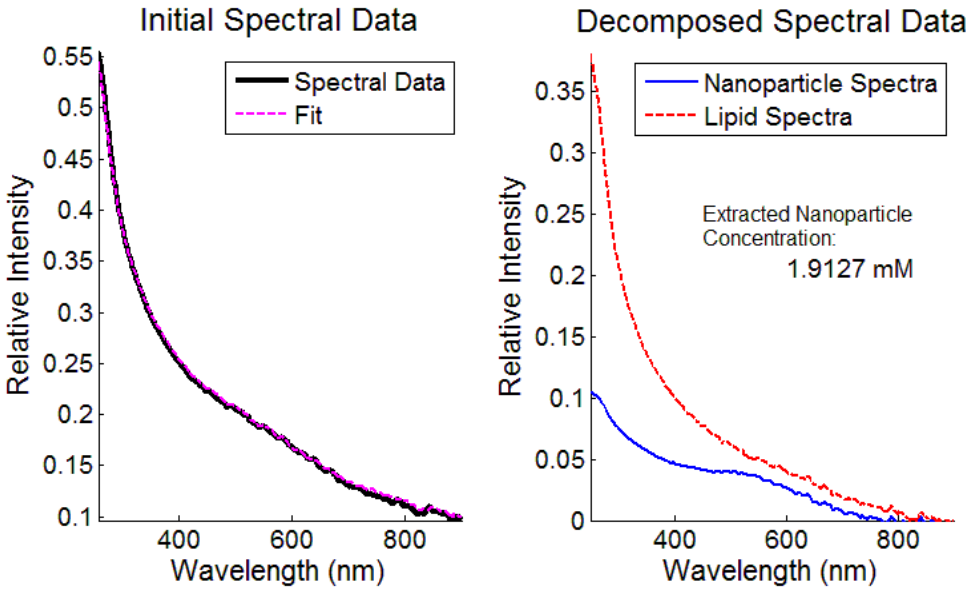

Figure 32. Spectra taken for a control sample with a total of 2 mM of nanoparticles and an unknown concentration of lipids. On the left is the initial signal along with the best fit line, on the right are the individual decomposed components of the sample spectra. Our fitting algorithm determined the nanoparticle concentration of the sample to be 1.91 ± 0.06 mM.

The fit matched our spectral data very well. We found that the amplitude of the nanoparticle component of the spectral fit was 0.19127 times weaker than the source nanoparticle spectrum measured in Figure 35a; since the concentration of that sample was 10 mM, and since we expect the spectral intensity of the nanoparticles to scale linearly with the concentration, we find that the nanoparticle concentration of this sample must also be 0.19127 times 10 mM, or 1.9127 mM. This measured value is outstandingly close to the actual nanoparticle concentration of 2 mM.

Finally, it is useful also to establish the minimum concentration of nanoparticles in solution that can be accurately detected using our algorithm. To directly test this, we produced several samples containing nanoparticles diluted in deionized water to various

concentrations, ranging from 10 mM to 50 μM. We then ran each of these samples through the spectrometer, extracted the nanoparticle concentrations using our detection algorithm, and then compared these values with the actual concentrations of our samples. These results are shown below in Figure 37, and they indicate that our algorithm cannot accurately determine (or that the spectrometer is not sufficiently sensitive to) the concentration of any sample containing less than about 200 μM.

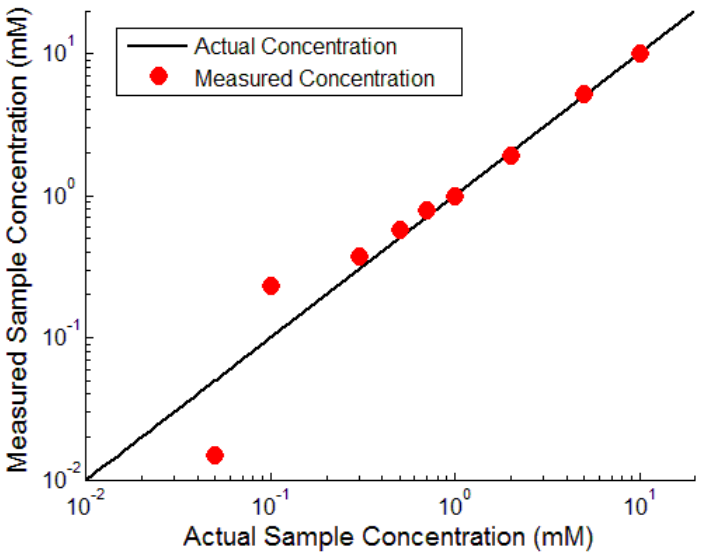

Figure 33. A plot of the measured concentration of a sample of 7nm Au-TTMA nanoparticles versus the actual concentration. Below a concentration of about 200 μM, the nanoparticles produce too weak of a spectral signature to be detected using this method.

Notes

[1] D. Needham and D. Zhelev, in *Perspectives in Supramolecular Chemistry* (John Wiley & Sons, Ltd., 2007), p. 102.

[2] M. I. Angelova, S. Soléau, P. Méléard, F. Faucon, and P. Bothorel, in *Trends in Colloid and Interface Science VI*, edited by C. Helm, M. Lösche, and H. Möhwald (Steinkopff, Darmstadt, 1992), p. 127.

[3] C. Herold, G. Chwastek, P. Schwille, and E. P. Petrov, Langmuir **28,** 5518 (2012).

[4] B. Mui, L. Chow, and M. J. Hope, in *Methods in Enzymology*; *Vol. Volume 367* (Academic Press, 2003), p. 3.

[5] J. B. Hutchison, A. P. K. K. Karunanayake Mudiyanselage, R. M. Weis, and A. D. Dinsmore, Soft Matter **12,** 2465 (2016).

[6] N. Rodriguez, F. Pincet, and S. Cribier, Colloids Surf B Biointerfaces **42,** 125 (2005).

[7] W. Haiss, N. T. K. Thanh, J. Aveyard, and D. G. Fernig, Analytical Chemistry **79,** 4215 (2007).

CHAPTER 6

NANOPARTICLE BINDING ON GUVS: FROM VESICLE GELS TO TOTAL VESICLE DISRUPTION

This chapter reports on the development of a well-defined lipid membrane and nanoparticle system that allows for tuning the interaction strength between the two. We use this to study how the interaction strength between a bilayer membrane and a solid object (in this case a functionalized gold nanosphere) can affect the shape of the membrane. In doing so, we hope to learn how to guide the assembly of novel functional materials.

We exposed giant lipid bilayer vesicles (GUVs, 50-100μm) to 7nm cationic Au-TTMA nanoparticles and observed the results. The adhesion strength of the nanoparticles to the vesicles was controlled by varying the ratio of the two lipid species composing them: zwitterionic DOPC and anionic DOPS. When the mole fraction of DOPS exceeded 4%, the membrane was highly disrupted by the nanoparticles and the vesicles were destroyed. When the mole fraction of DOPS was 4% or less, the nanoparticles caused the vesicles to adhere to one another and form a rigid liposome gel. These two behaviors can be explained by a transition from a partial wrapping of the nanoparticles to their complete envelopment by the membrane when the DOPS content exceeds roughly 4.5%. By contrast, when polymers bound to the vesicle, we found adhesion and gel formation, and not vesicle disruption, for 0-10% DOPS, showing that the rigid shape of the particles is necessary for the membrane disruption. These findings could be used to create cargo-carrying liposomes with the ability to rupture on trigger, or to engineer new solid, semi-permeable materials that can encapsulate cargo.

Methods and materials

In these experiments, DOPC GUVs were prepared using the electroformation technique described in Chapter 6. In order to adjust the adhesion energy between the cationic nanoparticles and the zwitterionic membrane surface, several sets of vesicles were prepared; these samples ranged from 100% mole fraction DOPC with 0% DOPS (0.5mg DOPC), to 85% mole fraction DOPC with 15% mole fraction DOPS (0.425mg DOPC with 0.075mg DOPS. All GUVs were formed in a 175 mOsm sucrose solution and then diluted with 180 mOsm glucose solution to a 1:1 volume ratio. During these experiments, the vesicles were exposed to 7 nm Au-TTMA cationic nanoparticles; these same nanoparticles are described in greater detail in Chapter 7 (Figure 34).

Sample Preparation

First, nanoparticles must be diluted in the same solution as the GUVs. To accomplish this, 2 μL of 7-nm Au-TTMA nanoparticles (10 mM nanoparticles in H_2O) were diluted with 10 μL of 175 mOsm sucrose and 10 μL of 180 mOsm glucose. This serves two purposes; first, it dilutes the stock concentration of nanoparticles to the desired concentration, and second, it adjusts the osmolarity of the nanoparticle solution to approximately match the osmolarity of the GUV solution, and avoids rupturing the GUVs on contact due to osmotic shock. This stock sugar/nanoparticle solution was vortexed at high speed for 2 minutes to ensure an even mixing of all species, then sonicated for 90 seconds to break apart nanoparticle aggregates.

Because we would like to examine the effects of nanoparticle adsorption onto the membrane while the adhesion is actually taking place, it is necessary to mix nanoparticles with the GUVs and then examine the mixture under a microscope as they mix. To this end, we first add GUVs into a long, narrow perfusion chamber (Grace Bio Labs), place the chamber on the microscope, and wait a few minutes to allow the GUVs to settle onto the coverslip. Then, we add 5 μL of the stock nanoparticle solution described above into one end of the perfusion chamber (Figure 38).

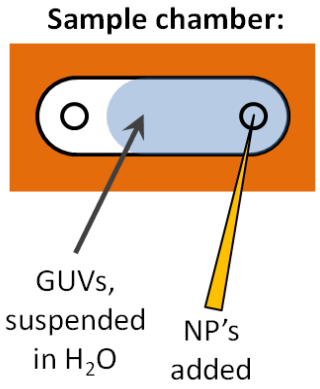

Figure 34. Top-down schematic of GUV sample chamber setup. Nanoparticles are added from the right, and slowly diffuse towards the left into the sample. This slows the addition of nanoparticles to aid in imaging adhesion events.

This method limits the rate of diffusion of the nanoparticles into the sample of GUVs, making it easier to gather information on the effects of the adhesion process. As the nanoparticles diffuse from one end of the sample chamber to the other, it creates a visible 'front' of adhesion events that can be tracked across the sample with relative ease. Focusing the microscope a few millimeters to the left of where the nanoparticles were

added into solution, it typically took about 10 minutes before the effects of the nanoparticles would become apparent.

Microscopy of GUVs

All samples were imaged on a Zeiss Axiovert 200 microscope using a Zeiss 63× Plan Neofluar oil-immersion objective. Images were recorded digitally using a CoolSnap HQ2 CCD camera (Photometrics Scientific), which has a linear response to intensity. In nearly all cases, GUVs were imaged using bright field techniques. However, dark field microscopy was employed to verify that the cationic Au-TTMA nanoparticles could properly adhere to the surface of the vesicles (Figure 39). This technique was also used to examine specific nanoparticle adhesion sites during some experiments (described in a later section of this chapter). With dark field microscopy, only the light reflected from the sample is imaged on the camera. Using this technique, the highly reflective gold-core nanoparticles appear brightly against an otherwise dark background, so that they appear with greater contrast.

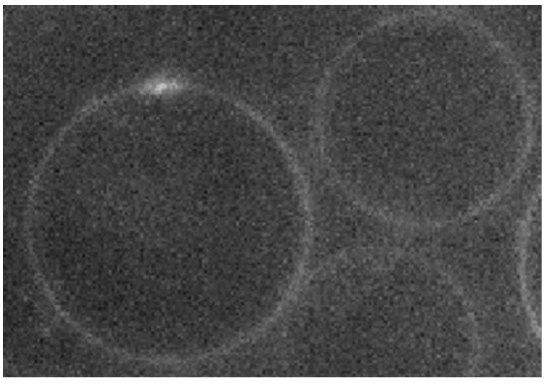

Bare GUVs

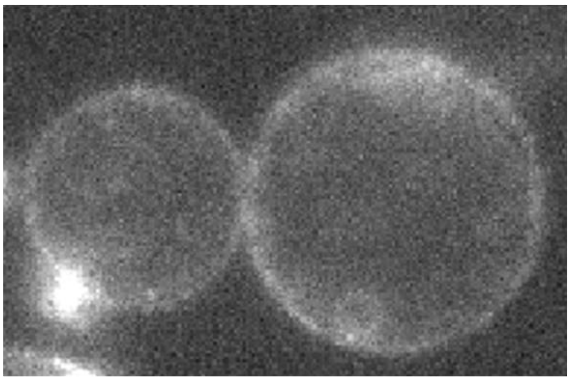

GUVs with gold nanoparticles

Figure 35. Vesicles imaged using dark field microscopy. On the left is an image of vesicles with no nanoparticles in solution; they appear only very faintly. On the right are vesicles that have nanoparticles added in solution. The brightness of the surface of the GUVs implies that the gold nanoparticles have adhered to the vesicles.

Overview of results

The head group of the DOPS lipid is cationic, and it therefore binds more strongly to the cationic nanoparticles than does the zwitterionic DOPC (even though DOPC is slightly negative in charge[1]). By adjusting the DOPS content of the vesicles, we can change the average surface charge of the GUVs, and adjust the adhesion energy between the particles and the lipid bilayer. Consequently, we also adjust the shape of the deformation made by the nanoparticles on the membrane, changing how the adsorbed particles interact with each other and, by extension, how they reshape the membrane surface.[2-4]

To examine this effect systematically, several batches of GUVs were prepared with an incrementally increasing mole fraction of DOPS (between 0% and 15%). Identical concentrations of nanoparticles were added to samples from each of these batches of GUVs, and the effects were documented. Strikingly, only two different types of behaviors were observed, separated by a sharp crossover near an average DOPS content of 4.5%. (Figure 40)

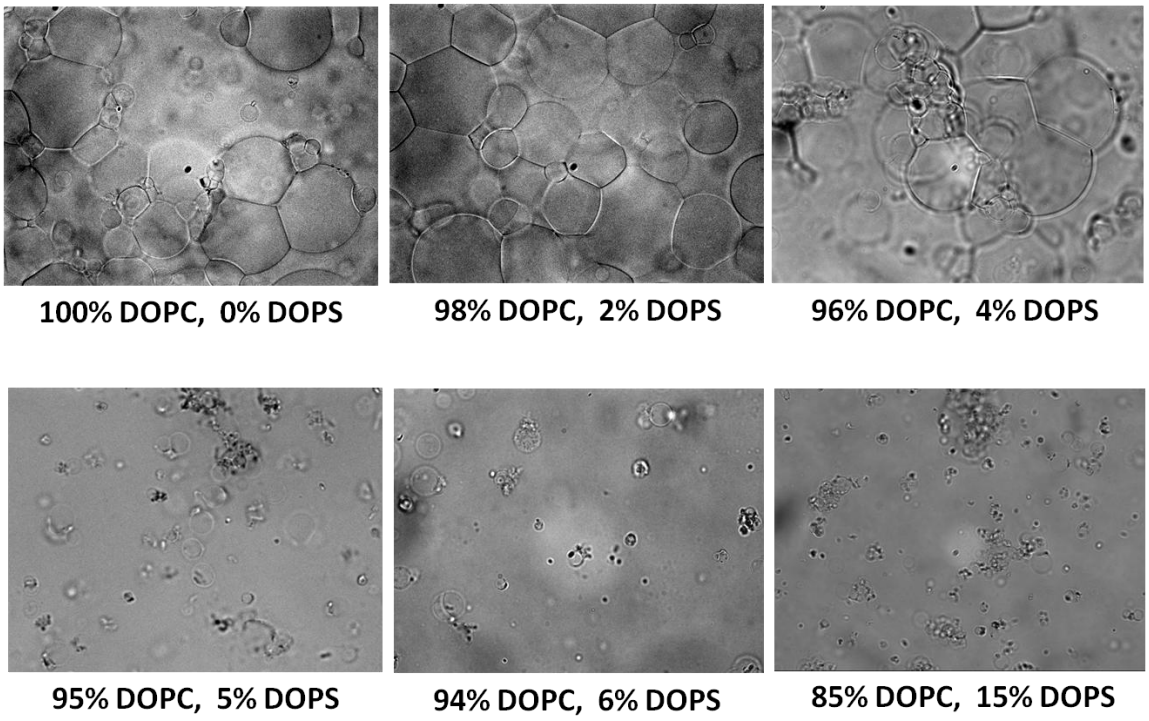

Figure 36. Each image shows the steady-state conformation taken by the vesicles after the nanoparticles have adsorbed to their surface. When the DOPS content of the vesicles ≤ 4%, the vesicles stick together, forming a gel structure resembling soap foam. When the DOPS content > 4%, all of the vesicles are simply destroyed.

Apparently, when the DOPS content is less than or equal to 4%, the vesicles adhere to one another. This adhesion leads to the formation of a cohesive gel network of vesicles; the overall appearance of the vesicle-gel is visually similar to a dry soap foam (where the air in the foam is replaced by water in the vesicle gel). The unique, cell-like structure allows it to fully encapsulate a large volume of liquid within a series of robust interior partitions, making it a potentially useful delivery vehicle for topical drugs, dyes, or other substances. Conversely, when the DOPS content is greater than 4%, the adsorption of the nanoparticles causes the vesicles to be completely disrupted. Such behavior potentially has use in controlled-release applications, and could also serve as a

useful experimental model for cell lysis. The specific behaviors observed in these two different regimes are robust and highly repeatable, and are far outside the realm of normal behavior for ordinary GUVs.

Before we examine the phenomenology of these two regimes in greater detail, we conjecture on the physical mechanism underlying this behavior. Motivated by the findings of Deserno *et al.*,[5,6] we speculate that the increase in adhesion energy leads to a critical change in the conformation assumed by the adsorbed nanoparticles on the membrane surface (Figure 41). In the case where the DOPS content is ≤ 4%, the nanoparticles may be only partially wrapped by the membrane; however, in the case where the DOPS content > 4%, we speculate that the particles are instead completely enveloped by the membrane. The existence of a transition between these two configurations was suggested by calculations made by Deserno *et al*,[5,6] who also predict that increasing the binding energy between the particles and the bilayer ought to lead to a crossover from one regime to the other (Figure 8).

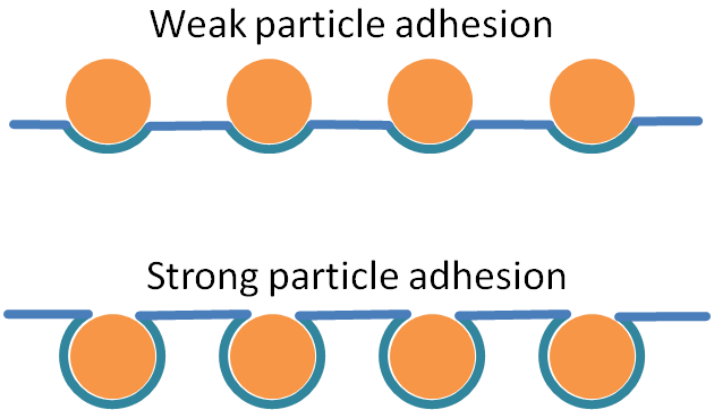

Figure 37. Cross-sectional illustration of the difference between the deformation of the membrane in the weak adhesion regime (top panel, DOPS ≤ 4%) and the strong adhesion regime (bottom panel, DOPS > 4%). The blue line represents the shape of the membrane, the orange circles represent nanoparticles.

Let us conceptually examine the two different cases presented in Figure 41 in order to understand how these behaviors could lead to the phenomenology described in Figure 40. First, in the case of weak adhesion, nanoparticles adsorb only to the surface of each vesicle. If a nanoparticle-laden vesicle happens to make contact with the surface of a bare vesicle, the exposed nanoparticles on the first vesicle can potentially bind onto the bare surface of the second vesicle, thereby creating an adhesive bridge and effectively binding the two vesicles together. We propose that this mechanism leads to gel formation in the weak-adhesion case, where the DOPS content of the vesicles ≤ 4%. In other words, the adsorption of the nanoparticles creates a patchy surface charge on the otherwise weakly dipolar surface of the vesicles, making them 'sticky' to one another and driving aggregation. (Figure 40, top row.)

On the other hand, in the strong adhesion regime, nanoparticles are fully engulfed by the membrane, such that no part of the nanoparticle is exposed at the outer surface of the bilayer. In this regime, vesicles ought not to adhere to one another. However, even when the membrane is fully loaded with enveloped nanoparticles, these nanoparticles are fully covered by the bilayer, and thus even more nanoparticles can still bind onto the bare surface of the vesicle. This process of continuously recruiting nanoparticles into the surface can lead to enormous in-plane strains, causing the membrane to rupture in a surprisingly complex but reproducible way. (Figure 40, bottom row.)

DOPS > 4%: Vesicle disruption

In the regime where the DOPS content of vesicles exceeds a molar fraction of 4% with DOPC, the vesicles are completely disrupted by the Au-TTMA nanoparticles. In this section, we will examine the phenomenology of the disruption mechanism in greater detail. Before each vesicle actually ruptures, it passes through a series of stages that seem to be quite robust, appearing for nearly every vesicle examined in these experiments. These stages are exemplified below in Figure 42.

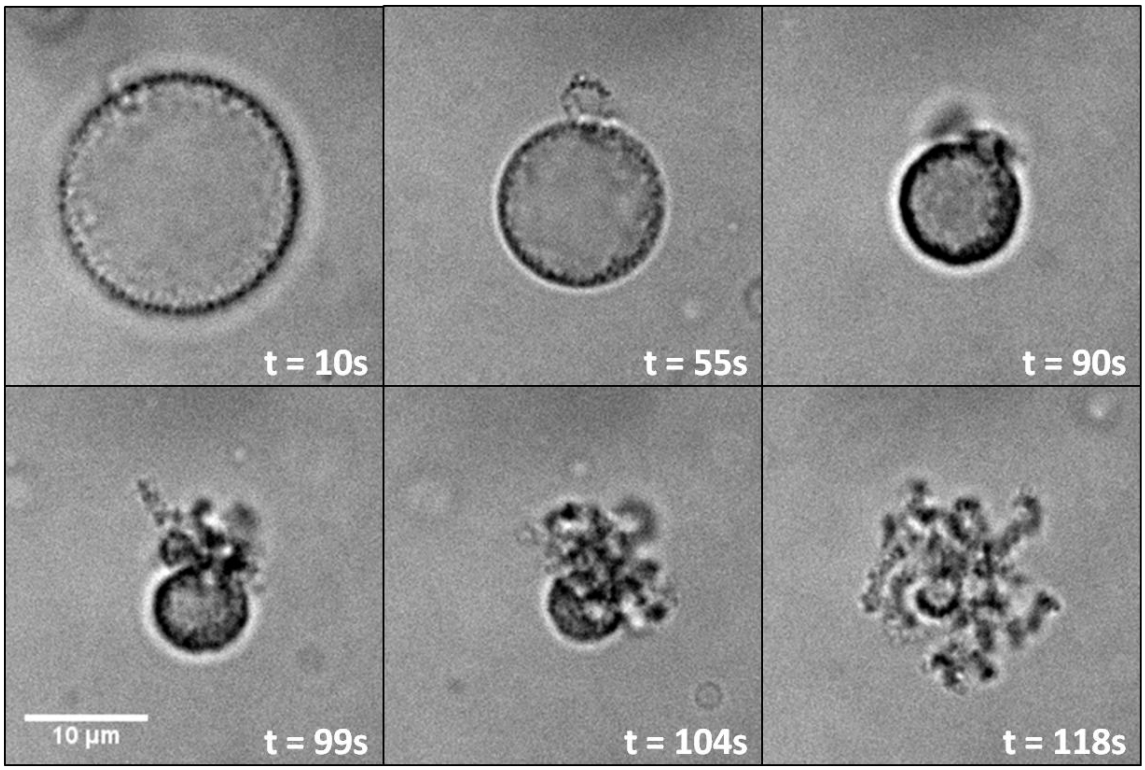

Figure 38. A series of still frames showing the time evolution of a vesicle leading up to complete nanoparticle-induced disruption. The vesicle in these images contained 6% DOPS. Images were taken using DIC optics.

The process of disruption on a unilamellar vesicle proceeds in the following manner: first, the diameter of the vesicle steadily and noticeably decreases as the membrane becomes loaded with enveloped nanoparticles. During this stage, the vesicle becomes covered in dark 'spots' that diffuse across its surface, and in some cases also develops a stable, large pore in the membrane (Figure 48). Remarkably, this pore has a size of more than a micron, much larger than the size of an individual particle. Finally, the vesicle does a complete inversion, where the interior of the vesicle is forced outwards through the pore that developed in the previous stage (or, if a pore did not form, its surface suddenly and violently ruptures), revealing a tube-like structure—presumably composed of folded lipid bilayers and saturated with nanoparticles (Figure 52). If the vesicle is multilamellar, the outer layers of the vesicle are peeled off one by one as they rupture from the nanoparticles, until only one inner layer remains. In the following subsections, we will examine each of these phenomena more closely.

The overall occurrence of this disruption process depends on the molar fraction of DOPS, but not the concentration of nanoparticles in suspension. In one experiment, nanoparticle suspension was prepared using 150 μL of 175 mOsm sucrose solution, 150 μL of 180 mOsm glucose solution, and 2 μL of 10 mM Au-TTMA nanoparticles—or 0.07x the concentration of nanoparticles used in all other experiments. We added 5 μL of this dilute stock to vesicles with 6% DOPS content, and we still observed the same behavior. The disruption process simply happened much more slowly, with one vesicle being tracked for nearly an hour without fully rupturing, after which point the vesicle was carried by convection outside the viewable area of the perfusion chamber. Although a complete disruption of this vesicle was not observed, its diameter visibly decreased by

more than a factor of 2. Additionally, other fully disrupted vesicles were visible elsewhere in the same sample. This result implies that it is unlikely for there to be a minimum concentration necessary for the disruption phenomenon to occur.

Furthermore, the critical molar ratio of 4.5% DOPS marking the crossover between these two regimes was not observed to depend on the osmotic pressure imbalance between the vesicle interiors and the solution. One might expect that, since the osmotic pressure in the vesicle affects the mechanical tension, and the tension is directly involved in determining the equilibrium wrapping of the particle (Equation 4), we ought to be able to change the behavior of the nanoparticle interaction with the membrane by adjusting the osmotic pressure . To test this hypothesis, four samples of vesicles were prepared; vesicles with 4% DOPS electroformed in 175 mOsm sucrose and diluted in 185 mOsm glucose with a 1:1 volume ratio (negative osmotic pressure, -10 mOsm), the same vesicles instead diluted with 165 mOsm glucose with a 1:1 volume ratio (positive osmotic pressure, 10 mOsm), and finally two more samples identical to the previous two but prepared with 5% DOPS instead. Because these samples are just above and just below the crossover concentration of DOPS, we would expect that a large change in osmotic pressure in the vesicles should measurably change the critical concentration of DOPS required for nanoparticles to be engulfed by the membrane. However, each of these 4 samples was exposed to an identical concentration of nanoparticles and let sit for 1 hour, and in all cases the results matched those reported in Figure 40 regardless of the vesicles' osmotic pressure. (Even though the vesicles under positive osmotic pressure were clearly stiffer and rounder than the ones under negative pressure, indicating that there was indeed an osmotic pressure difference between the samples.) This finding

echoes the apparent non-effect of osmolarity on the binding of the nanoparticles observed in our LUV experiments, detailed in Appendix A (Figure 68).

One possible explanation for this result is that the adhesion of the nanoparticles may form extremely small nanopores in the membrane, which allow solute exchange across the membrane. This phenomenon has previously been reported for cationic nanoparticles bound on DOPC membranes (Figure 43).[7] In these experiments, 20 nm diameter cationic amidine-modified polystyrene particles were exposed to lipid vesicles composed of an equi-molar mixture of DOPC, DPPC, and cholesterol. The authors reported that the adhesion of the nanoparticles caused leakage of a high molecular weight, rhodamine-labeled dextran from the vesicle interior, and estimated these pores to be a maximum of 18-27 nm in diameter. They suggested that the poration was caused by increased surface tension imposed by a steric pressure from packing the surface with bound nanoparticles; it has previously been shown that an imposed surface tension can form transient pores in a bilayer membrane.[8]

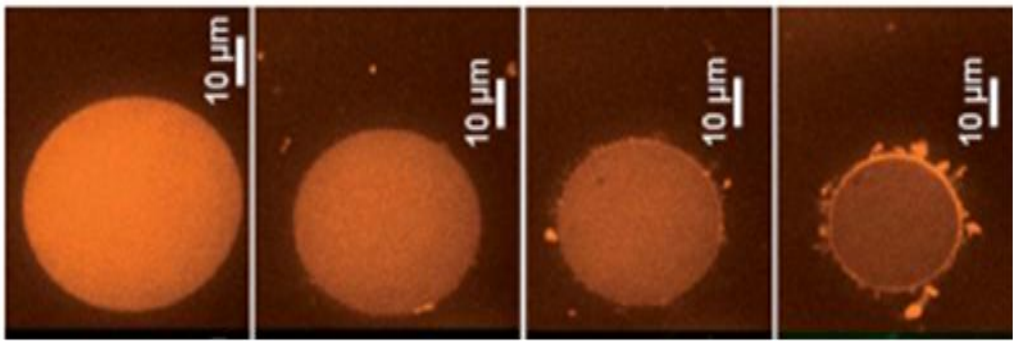

Figure 39. Florescent dye escaping from a vesicle due to adhesion of cationic nanoparticles. The total elapsed time is 140 minutes. Image reproduced from (Li et al., 2013).[7]

If this is indeed the case, pores in the membrane created by the nanoparticles could effectively equalize the osmotic pressure of the membrane as soon as the nanoparticles adhere, negating any possible contribution to the overall phenomenology.

Vesicle shrinking

At the start of the disruption process, the diameter of the vesicle steadily decreases. This aspect of the disruption process is likely the most immediately related to the adhesion and envelopment of the cationic nanoparticles. Assuming the interior volume is not fixed (owing to the previously mentioned nanoparticle-induced nanopore formation phenomenon[7]), when a single nanoparticle is engulfed by the membrane, the effective outer surface area of the vesicle ought to be reduced by an amount roughly equal to the total surface area of the nanoparticle. Thus, as more of the surface is involved in the wrapping adhered particles, the total diameter of the vesicle decreases.

We can indirectly test this hypothesis by noting that the rate at which the diameter of the vesicle decreases should be directly related to the rate of adhesion of nanoparticles, which itself is related to the local concentration of nanoparticles. Thus, the average rate of shrinking of the vesicles ought to be directly proportional to the concentration of nanoparticles in solution. Due to the method used to observe the disruption process however (Figure 38), a direct test of the relationship between the local nanoparticle concentration and the rate of change of the diameter of the GUVs is extremely difficult because the local nanoparticle concentration is not known. Nevertheless, it is circumstantially supported by the previous observation that GUVs in an environment

with an extremely low concentration of nanoparticles showed a significantly slower rate of shrinking.

Additionally, we note that vesicles in immediate proximity to one another tend to shrink at nearly identical rates. As demonstrated in Figure 44, in both examples of GUVs shrinking in close proximity to one another, the radius of the vesicles decreased at nearly the same rate as the nearby vesicle. And, even though all four vesicles had the same 5% DOPS content, the GUVs in the top row shrank at a far slower pace than did the GUVs in the bottom row (from a different sample). Moreover, for the vesicles shown in the bottom row, nanoparticles had been added about 5 minutes prior to the start of the video, and in the top row the nanoparticles had been added about 50 minutes prior. Due to the way the nanoparticles are added into solution (Figure 38), this observation implies the local concentration of nanoparticles was likely to be much higher for the vesicles in the bottom row than in the top row, further supporting the conclusion that nanoparticle concentration is a critical factor in determining the rate of shrinking of the vesicles.

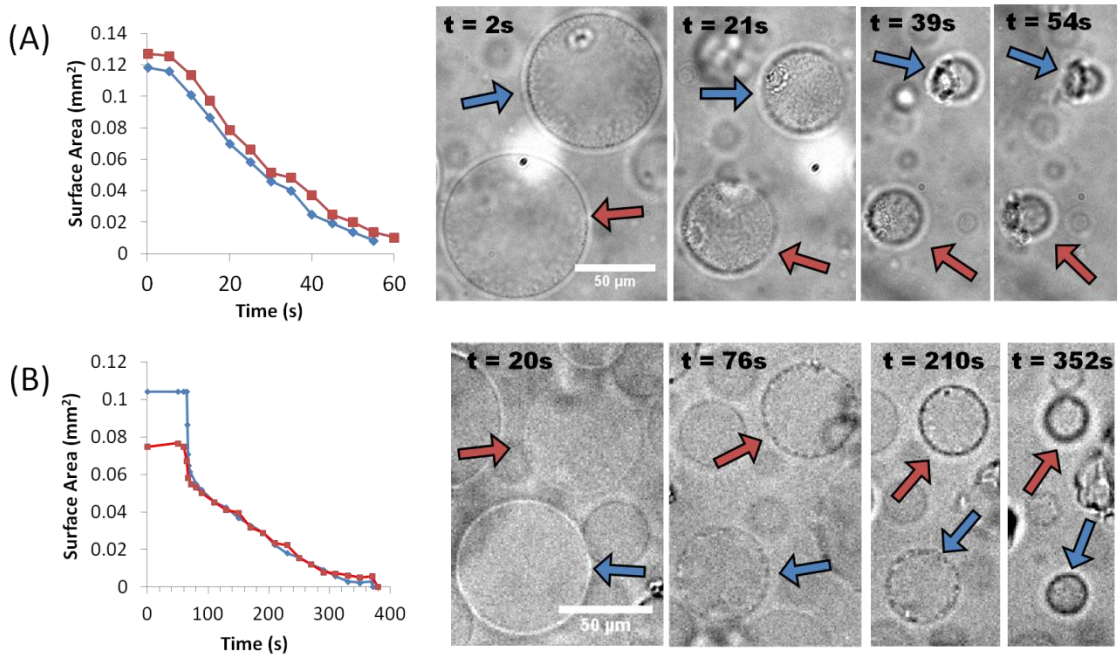

Figure 40. Rate of collapse of vesicles. The initial concentration of added nanoparticles was the same in both experiments; in the bottom plot, nanoparticles were added roughly 50 minutes prior to the start of the clip, and in the top plot nanoparticles were added roughly 5 minutes prior. In both cases, the two nearby vesicles shrink at nearly identical rates. In both plots, vesicles have 5% DOPS and 95% DOPC. In the bottom plot, the vesicles do not develop a surface pore, and simply rupture at the end of the video; in the top plot, both vesicles develop a surface pore, and slowly invert through the pore as they shrink.

This data also reveals some information about the way the vesicles collapse. They often initially collapse extremely quickly, taper to a linear decrease in the surface area of the vesicle with time, then slowly taper to a sublinear descent before finally rupturing. The sharp initial decrease in radius observed for the vesicles in the top row of Figure 44 is observed frequently, but not always; the initial rate of collapse of these vesicles is 50 times faster than their overall average, and nearly 5 times faster than the average rate of collapse of the vesicles in the bottom row of the figure. We have not yet determined a cause of this effect. Surprisingly, we also have not been able to identify any evidence that

the appearance of a large pore on the surface of the vesicle has any impact the rate of decrease of the radius of the vesicle (as discussed below).

Surface spotting

As the diameter of the vesicle shrinks, dark spots noticeably develop on the surface of the vesicle (Figure 45). This effect is as universal as the shrinking phenomenon. Because they are dark, we conclude that they are enriched in Au-TTMA particles, in which these clusters imply that there is an attractive interaction between particles mediated by the deformed membrane.

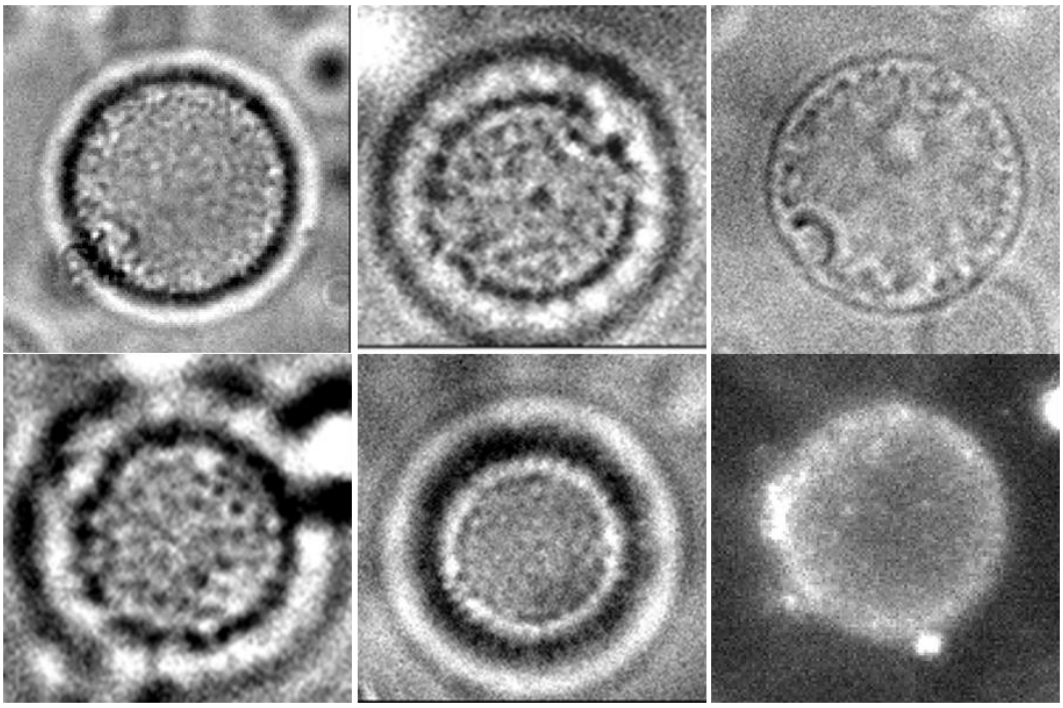

Figure 41. Several different GUVs showing surface spotting. Each image was taken from a sample of vesicles with 6% molar fraction DOPS and 94% DOPC. The bottom right image was taken using dark-field illumination. Each image has been resized separately.

We note a few key observations. First, although these small dark spots are close to (if not just beyond) the resolution limit of our microscope, their visibility and size indicate they are likely clusters of many particles and not individual adhesion sites. Second, as more nanoparticles bind and the vesicle shrinks, these dark spots visibly increase in number, but they do not increase in size. In fact, the size of these dark spots is remarkably consistent from one vesicle to the next. Finally, the spots appear to diffuse freely on the vesicle surface, but their mobility noticeably decreases as the vesicle becomes small and the surface becomes packed with such spots.

Because of the technical difficulty involved with imaging these small dark spots on the spherical surface of the GUVs, experiments designed to measure the size, number, and diffusion of these spots were unsuccessful. However, the observations listed above imply that particles bound to the membrane surface form some type of cluster with a characteristic size. Additionally, from dark field imaging it is clear that not all of the adsorbed particles are involved in forming these spots (Figure 45, bottom right). Although isolated bright spots are visible, we can see that the overall surface is still reflective, indicating the presence of the reflective gold nanoparticles.

The existence of a similar nanoparticle-clustering phenomenon was reported in an experiment with Au-TTMA nanoparticles adhering to the surface of *E. coli* cells.[9] In these experiments, the authors showed that adhered 6nm nanoparticles formed small clusters on the bacteria, while 2 nm particles cooperatively deformed the membrane

surface to produce cone-shaped protrusions (Figure 46). Without performing TEM or Cryo-EM on our samples however, it is impossible to tell whether the spot-like features that form in our experiments match either of the structures found on their *E. coli* cells.

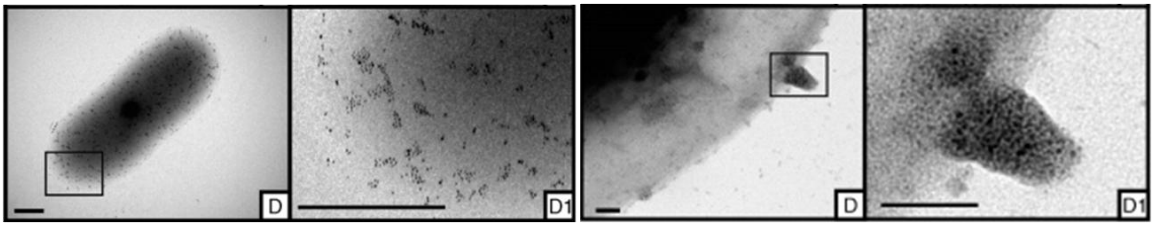

Figure 42. Nanoparticle behavior on the surface of an *E. coli* cell membrane. In the left panels, adhered 6nm Au-TTMA nanoparticles cluster together, causing particles to form patches on the surface; scale bars are 200 nm. In the right panels, adhered 2 nm Au-TTMA nanoparticles cooperatively deform the membrane, leading to cone-shaped protrusions; scale bars are 50 nm. Image reproduced from (Hayden et al., 2012).[9]

Additionally, similar formations have been predicted to form based on simulations of particle adhesion onto membranes. Simulations of a tension-free patch of a bilayer membrane with bound hemispherical caps by Reynwar *et al*. show that the adsorbed particles can cooperatively deform the membrane and create a large invagination on the surface (Figure 47).[10] Several other recent studies have reported similar results.[11-14]

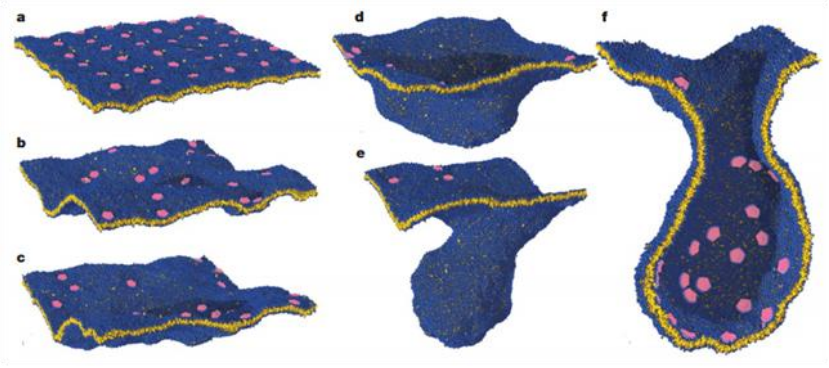

Figure 43. Simulations of adhesive nanoparticle caps onto a tension-free membrane. The formations are similar to those found by Hayden *et al.*,[9] but are directed inward rather than outward. Image reproduced from (Reynwar *et al*., 2007).[10]

However, none of the simulations listed above fully explain the apparent characteristic size of the features we observe on the GUVs. However, simulating interactions between particles adsorbed to a bilayer membrane is a very difficult. This is largely due to the number of parameters involved with predicting the exact shape and behavior of the deformations created by the nanoparticles (as outlined in Chapter 5). A sufficiently complete simulation using all of these parameters and including several hundred adsorbed particles may be a prohibitively complex undertaking. Still, it is not unlikely the interactions between the adsorbed particles include a combination of long-ranged repulsion and short-ranged attraction (as predicted by Reynwar *et al*.[3]), and clustered particle phases have indeed been reported in such cases.[15,16]

Macroscopic pore formation

The formation of a stable, macroscopic pore in the vesicle bilayer is a feature that, to our knowledge, is heretofore unreported in the literature. As stated in the previous

sections, in most instances the vesicle ruptures only as an immediate precursor to the inversion phenomena. However, in some cases, a pore visibly develops concurrent with the shrinking phenomenon (Figure 48). In these cases, instead of violently rupturing, the interior of the vesicle is slowly pushed outwards through the large open pore.

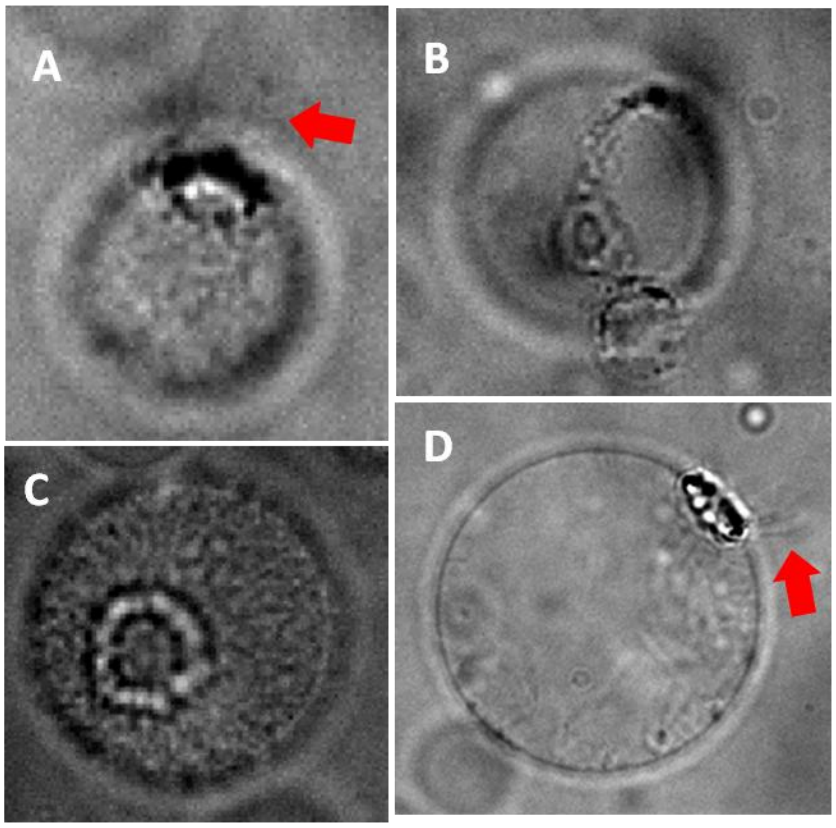

Figure 44. Images showing unilamellar vesicles that have developed a stable, macroscopic pore in their surface. In these cases, the pore develops well before the vesicle inverts itself. In images A and D, fluid can be seen escaping the pore (indicated with red arrows). In image B, a large pore has opened in the outermost bilayer of a multi-lamellar vesicle.

Evidence that these features are truly an open pore can be seen in Figure 48, panels A and D. Since the encapsulated fluid (175 mOsm sucrose) has a different index

of refraction than the exterior fluid (87.5 mOsm sucrose + 90 mOsm glucose, the encapsulated fluid produces a noticeable fingering effect as it escapes through the pore. Several attempts were made to visualize this effect directly by producing vesicles that encapsulate florescent dye (fluorescein), but these experiments were not successful due to the difficulty in finding and capturing such an event given the rapidity with which fluorescein photobleaches.

Additional evidence that these features are indeed large stable pores comes from the fact that we can observe interior features of multi-lamellar vesicles escaping through these pores, as seen in Figure 49. We also note that there appears to be a characteristic 'pearl necklace' shape to the outer rim of each pore (Figures 48 and 49), likely formed by excess membrane material as the pore opens.

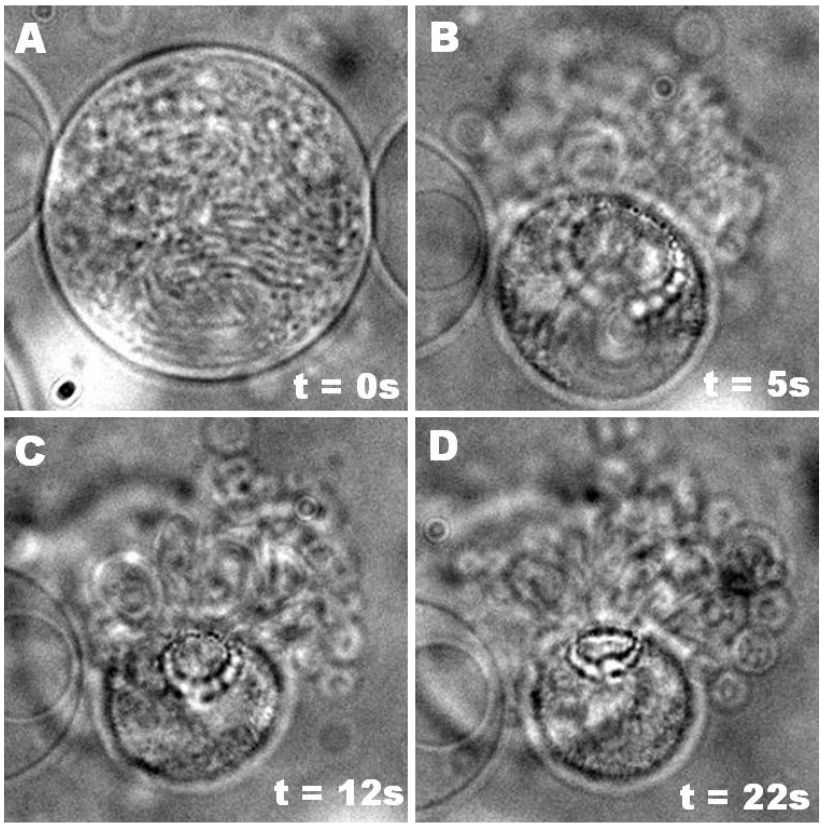

Figure 45. Interior contents of a multi-lamellar vesicle spilling out through a pore on the vesicle's outer surface. The vesicle did not outright rupture after this point, and continued to be disrupted by the nanoparticles. The vesicle has 5% DOPS and 95% DOPC by mole fraction.

We next conjecture on the nature of these pores and their underlying formation mechanism. First, we can assume that their formation has an energy barrier, because a maximum of one pore has ever been observed on each vesicle. If the pore formation were a product only of single-nanoparticle adhesion (as is the case with the nanopores described in a previous section[7]), we would expect to see at least one vesicle with multiple pores, but this is not the case. It therefore seems likely that the pores form in response to tension in the membrane caused by the rapid adhesion and engulfment of the nanoparticles (Figure 50).

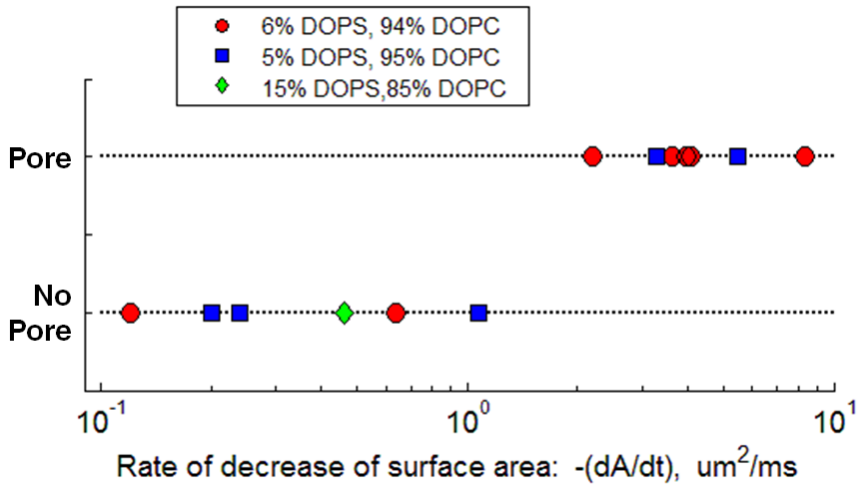

Figure 46. A plot of the rate of decrease of surface area for 13 unilamellar vesicles as they are disrupted by adhered nanoparticles. The vesicles that appeared to form a pore are plotted on the top line, vesicles that did not appear to form a pore (and instead burst just before inversion) are plotted on the bottom line. This data makes it clear that the shrink rate of the vesicles is closely related to pore formation, whereas the DOPS content is not. Unfortunately the local nanoparticle concentration is difficult to discern in most of these cases, as the total time elapsed was not recorded for several of these trials.

As Figure 50 makes clear, only vesicles whose surface area decreases faster than a rate of approximately 1.5 μm^2/ms form a visible pore, regardless of the DOPS content of the vesicle. But why should this be? As was explained previously, the adhesion of the nanoparticles reduces the exposed surface area of the vesicle, but it does not reduce the encapsulated volume of liquid, creating stress in the plane of the membrane. Although it is likely that adhesion opens nanopores to equalize the interior solute concentration and reduce osmotic pressure,[7,8] if the surface area is reduced rapidly it may build stress in the membrane faster than diffusion of liquid through the nanopores can reduce it. This, in turn, could cause the membrane surface to rupture (or 'lyse'). Normally lysis destroys the vesicle entirely, but if the bilayer is already loaded with enveloped nanoparticles, the

matrix of strongly adhered particles may prevent the vesicle from outright collapse. We note that stable pores have only been observed on nanoparticle-loaded vesicles; nanoparticle-sparse vesicles that form a pore all immediately lyse (Figure 51). Once a large, stable pore has formed, it essentially eliminates the volume constraint on the shape of the vesicle, thereby preventing the need to develop additional pores.

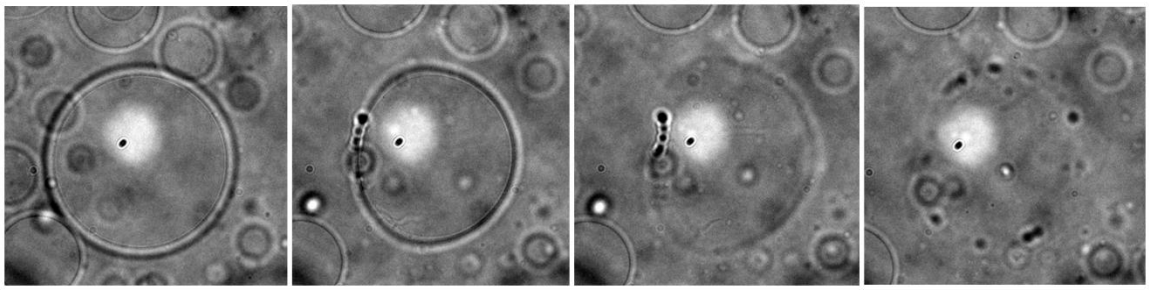

Figure 47. A vesicle whose surface is not visibly loaded with nanoparticles develops a pore, and immediately bursts. The pore expands outwards as the vesicle collapses.

Vesicle inversion

The final stage of the disruption process is the complete inversion of the GUV (Figure 52). The inversion of the vesicle reveals a tube-like structure; it is not clear whether this structure is already existent on the inside of the disrupted vesicle and is formed by the adhesion of the nanoparticles, or whether the feature is created during the inversion process itself. Any evidence of tubulation of the interior is not immediately visible from the outside of the disrupted vesicle, but this does not rule out the possibility.

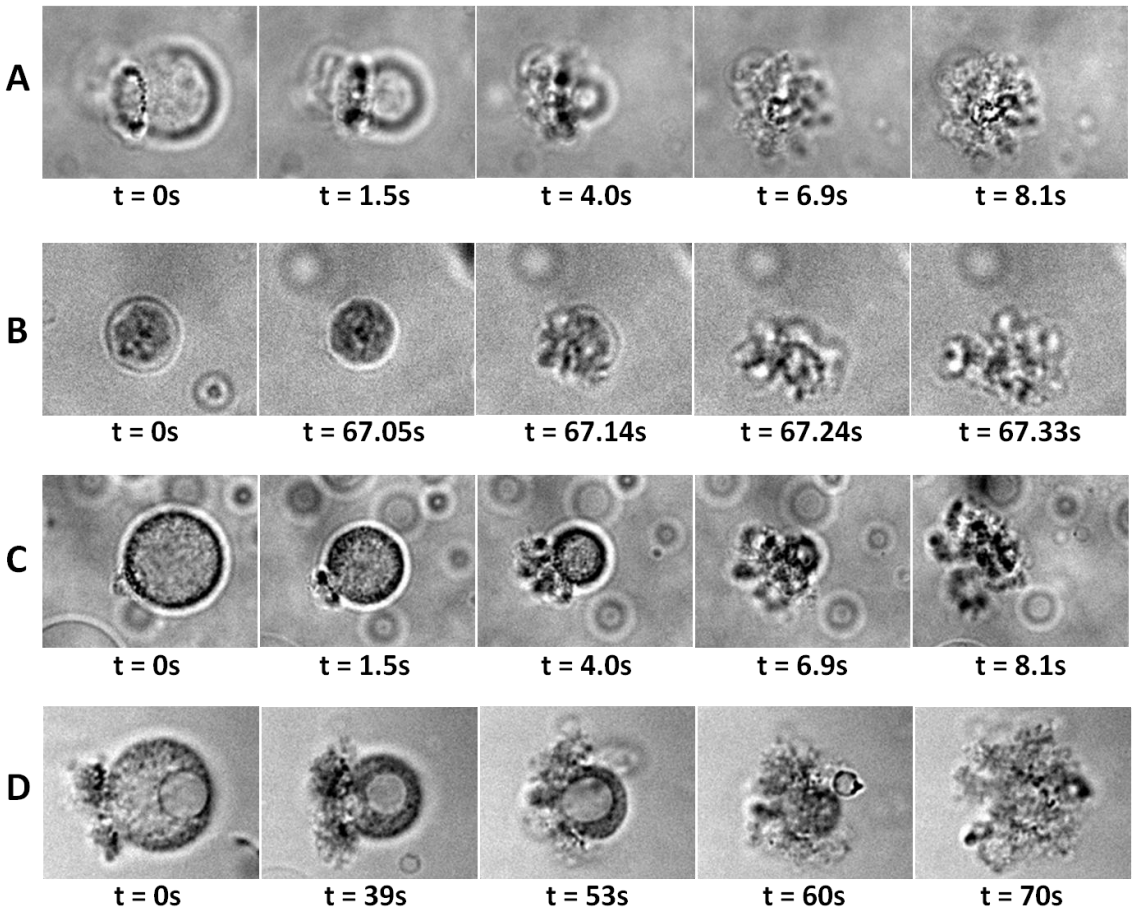

Figure 48. Inversion of various GUVs. (A) 6% DOPS; interior is quickly pushed out through a very large pore. (B) 15% DOPS; a fast, violent rupture of a vesicle without a surface pore. (C) 6% DOPS; inversion through a small pore on the surface, revealing long protruding tentacle-like formations. (D) 6% DOPS; very slow inversion of a vesicle encapsulating many smaller vesicles. In this particular case, the pore formation was likely related to its highly multilamellar interior rather than to the rate of adhesion of nanoparticles.

Although perhaps the most visually striking step in the disruption process, it is the one we can discern the least about from analyzing video alone. In other aspects of the disruption process, we can make educated guesses about what precisely is the cause or mechanism, but in this case we can only speculate. The tube-like features that emerge

from the disrupted vesicle somewhat resemble the ones reported by Yu *et al.* (Figure 6),[17] but to our knowledge this overall phenomenon has not yet been reported in literature.

Using image analysis, we found that the tubules have a typical diameter between 1 and 2 μm, although occasionally we observed vesicles with much smaller tubules (the ones in Figure 52d, for instance, have an average diameter of 0.3 μm). We do not yet know which properties of the disrupted vesicle (if any) determine the diameter of the tubules. In our experiments, we did not find the tubule diameter to have any particular dependence on the DOPS content of the vesicles, the initial size of the vesicles, or the rate of shrinking of the vesicles. Interestingly however, the tubules created by GUVs exposed to larger 12 nm gold nanoparticles were smaller in diameter (Figure 51), a fact discussed in a later section.

It is difficult to draw any conclusions about the structure or composition of these tubules using our existing data. The tubules are presumably composed of folded lipid bilayers and saturated with nanoparticles, but without performing Cryo-EM, there are few conclusions we can draw. It is possible that the exterior of the tubules are coated with nanoparticles, based on video showing a tubule adhering to—and subsequently destroying—an otherwise apparently bare vesicle (Figure 53). It is also plausible that more nanoparticles immediately adhered to the outside of the nanoparticle-saturated tubules ad soon as the vesicle was inverted; since this is the only instance of this particular phenomenon we have observed, it is difficult to say for sure.

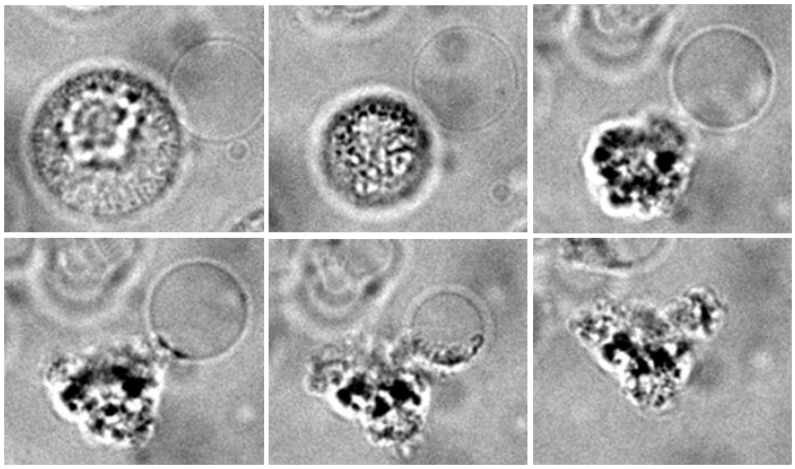

Figure 49. An inverted vesicle making contact with another vesicle, and immediately causing that vesicle's disruption.

Conclusions

Although there are many details about the disruption process we do not understand, there are several conclusions we can draw. The disruption process is a direct result of the envelopment of adsorbed nanoparticles by the membrane surface; the envelopment causes a reduction of surface area of the vesicle, causing the vesicle to decrease in radius at a rate that is likely proportional to the rate of adhesion of nanoparticles. If this rate of surface reduction is greater than about 1.5 $\mu m^2/ms$, the vesicle develops a large stabilized pore in its surface to relieve osmotic pressure. Finally, the vesicle is turned inside-out through this pore, revealing tendril-like tubular formations.

While highly destructive to the vesicles, there may be a number of uses for this phenomenon in controlled-release applications. Specifically, since the rate of disruption of the membrane is demonstrably related to the concentration of nanoparticles in solution,

it may be possible to tune the rate of release of the vesicles' cargo by adjusting the number of added nanoparticles.

DOPS ≤ 4%: Vesicle gel formation

In the regime where the DOPS content of vesicles is less than 4%, the vesicles adhere together, forming a macroscopic, semi-rigid soft gel network. Compared with the complex disruption process described in the previous section, this phenomenon is relatively straightforward. In this regime, nanoparticles bind only to the surface of the GUVs, creating an adhesive bridge when two vesicles come into contact. This ultimately leads to the formation of a macroscopic, gel-like aggregate of vesicles (Figure 54). In this section, we use image analysis to measure several physical properties of the gel, and also examine ways to produce this material in bulk quantities.

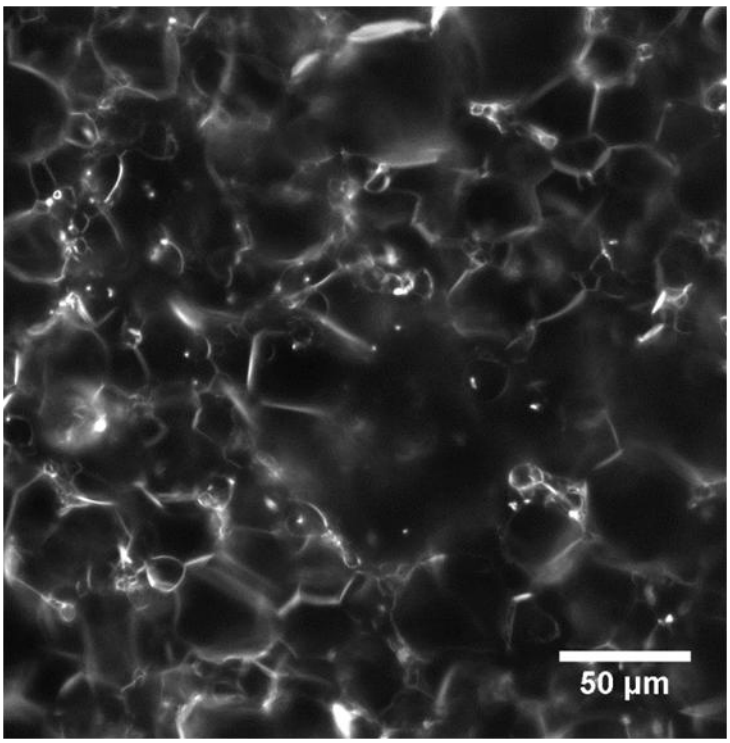

Figure 50. Dark-field image of a vesicle gel network. The highly reflective gold nanoparticles can clearly be seen at the interfaces between neighboring vesicles in the gel. Formed on a microscope coverslip, this gel is only about 50µm thick (the diameter of one GUV), but is nearly 1cm x 1cm in width.

Analysis of gel network formation

Figure 55 illustrates a typical time-lapse of nanoparticles being added into solution with GUVs. In these images, the vesicles were composed of pure DOPC, and nanoparticles diffused inwards from the right side of each frame. As more nanoparticles adhered to the vesicles, more vesicles began to adhere to one another, until nearly all the GUVs in frame had been incorporated into a single large gel network.

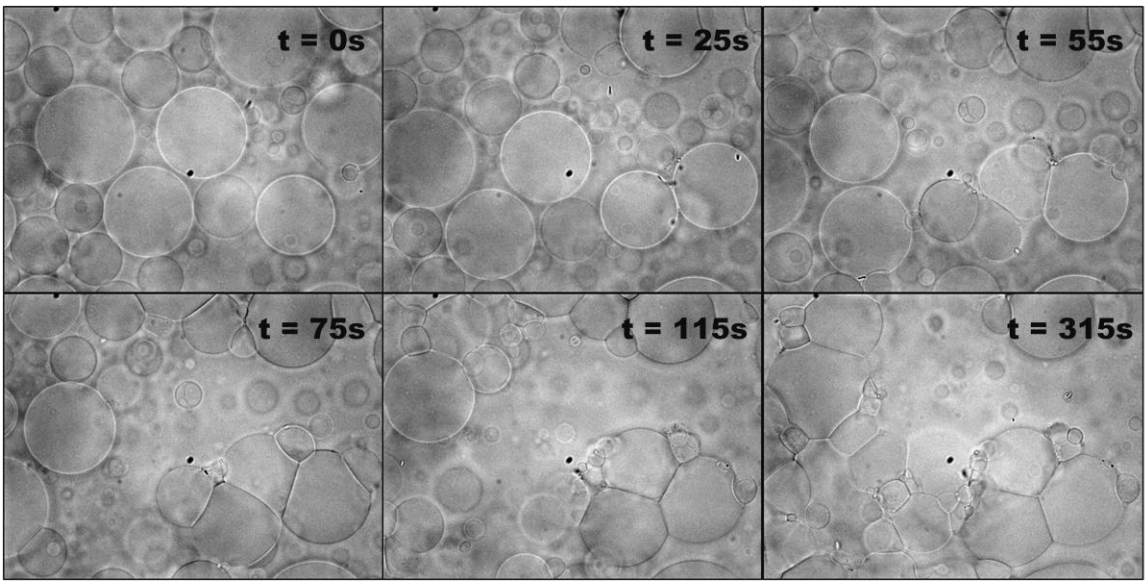

Figure 51. Time lapse illustrating the adhesion process on DOPC vesicles. Nanoparticles diffuse into frame from the right as time elapses (as indicated in Figure 38).

To better understand the growth kinetics of the gel, we analyzed video featuring two large vesicles slowly joining together (Figure 56). In this video, the total contact area between the two adhered vesicles slowly increased over the course of about two minutes, after which point one of the vesicles burst. We measured the contact area between the two vesicles by first measuring the length L between the two points of contact of the GUVs (these points are indicated in Figure 56 by small red dots in each frame). The approximate contact area between the vesicles was then calculated as $A_{appx} = \pi (L/2)^2$, and is plotted as a function of the elapsed time in Figure 56.

Apparently, the contact area between the adhered GUVs grows linearly with Log(t), meaning the rate of increase in contact area between the vesicles is inversely proportional to the elapsed time.

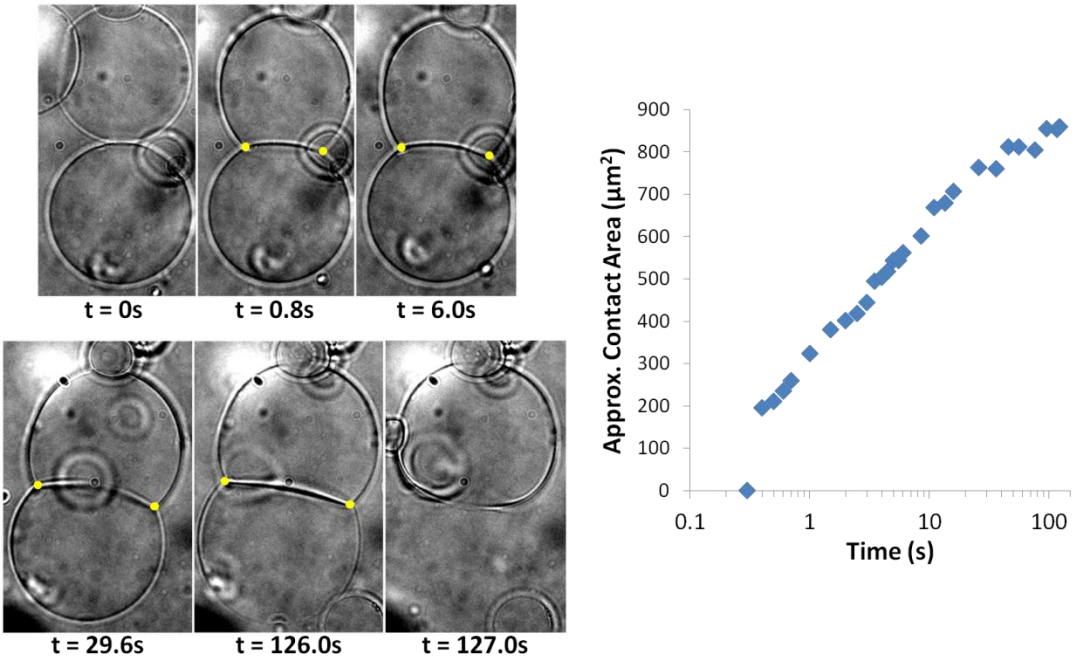

Figure 52. Adhesion kinetics for two vesicles. The total contact area between the two vesicles (measured via the distance between the two yellow dots in each image) appears to increase linearly with Log(t). After 126 seconds, one of the adhered vesicles suddenly burst, leaving the other vesicle stuck in an oblong shape.

Interestingly, once one of the vesicles burst, the neighboring vesicle retained an oblong, non-spherical shape for about 7 seconds (at which point it burst as well). This phenomenon may have been caused by adhesion of the vesicle to the glass cover slip; the cationic nanoparticles adhere to the slightly anionic charge of the glass, and hence the nanoparticles adhered to the surface of the GUV could have adhered the vesicle to the glass and forced it to retain an oblong shape.

Bulk production of gel networks using lecithin vesicles and cationic polymer

The reason for investigating methods of producing large quantities of vesicle gel networks is twofold. First, making any useful rheological measurement of the gel

stiffness typically requires tens of milliliters of material, whereas electroformation produces at most a few hundred microliters per batch (and is quite labor intensive). Secondly, being able to test and use this material in any practical or commercial sense demands the ability to scale up production immensely. This entire section will be devoted to the method we devised for producing this gel inexpensively in large quantities.

In order to produce our vesicle gel inexpensively, we search for alternative, cheaper component materials. Particularly, the expensive ultra-high-purity DOPC and DOPS lipids sold by Avanti Polar Lipids are ideal for creating highly uniform vesicles, but in this case our needs are for high volume and low cost; uniformity is not necessary. A convenient, lower-purity source of lipid is soy lecithin powder, a nutritional supplement derived from soybeans and commonly found at many health stores. Unpurified soy lecithin powder contains about 30% phosphatidylcholine (PC) lipids;[18] the polar head of these lipids matches DOPC, but the length of the fatty hydrophobic chain varies from lipid to lipid. It also contains up to 30% soybean oil, which can become emulsified in water by the lipids and can thus potentially disrupt the vesicle gel. Luckily, purified soy lecithin is a widely available substance used in food manufacturing. We received a sample of Phospholipon 85G from the American Lecithin Company, which contains 91.5% PC lipid, 2.8% Lyso-PC lipid, 1% unspecified nonpolar lipids, 0.3% PE lipid, and trace amounts of other non-lipid species. This waxy yellow substance can be dissolved in chloroform and electroformed in a manner identical to the DOPC lipids (explained in detail in Chapter 6). An image of these lecithin vesicles is provided below, in Figure 57.

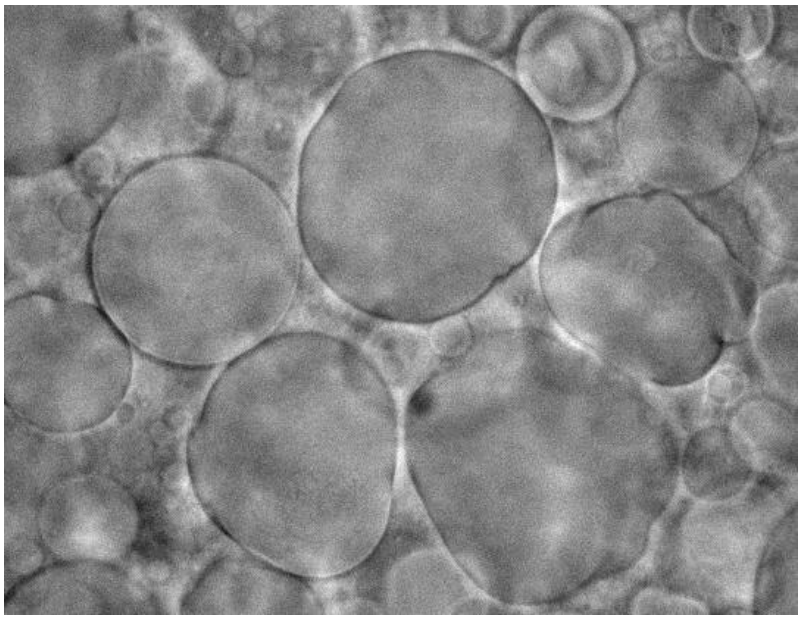

Figure 53. Lipid vesicles electroformed using purified PC lecithin powder from the American Lecithin Company. Imaged using a 40x microscope objective.

The vesicles produced this way are highly polydisperse in size, shape, and composition. They are also stable in solution for only 4-5 days, after which nearly all of the vesicles produced will have lysed—this shorter lifespan is likely a consequence of the polydispersity of the lipids. Importantly though, the Phospholipon lipids are approximately 1/2000th the cost of the purified DOPC lipids from Avanti (by weight).

Furthermore, the gold nanoparticles used in our experiments are a highly specialized material fabricated in a scientific laboratory. However, in principle most any cationic polymer can be used to drive the vesicle aggregation instead. As we previously identified, aggregation is caused when the vesicle surface is sparsely populated with adhered charged objects, and thus the charged object used to accomplish this task need not be such a costly material. We examined several different cationic polymers as a potential substitute to the nanoparticles, including TTMA polymer (identical to the

polymer ligand on the gold nanoparticles, fabricated by YiWei Lee and Li-Sheng Wang, poly-L-lysine (molecular weight = 70,000, from Sigma Aldrich, #P4707), spermine (Sigma Aldrich, #S4264-1G), and spermidine (Sigma Aldrich, #S0266-1G).

In these experiments, we first exposed lecithin PC GUVs (produced via electroformation) to low concentrations of each type of polymer in order to gauge which (if any) species could generate a vesicle gel network. We found that only poly-L-lysine and TTMA accomplished this; the other polymers did not. Next, to determine the optimal concentration of polymer to form a gel, we exposed samples of lecithin vesicles to a wide range of concentrations of TTMA and poly-L-lysine. The results of these tests are pictured in Figure 58.

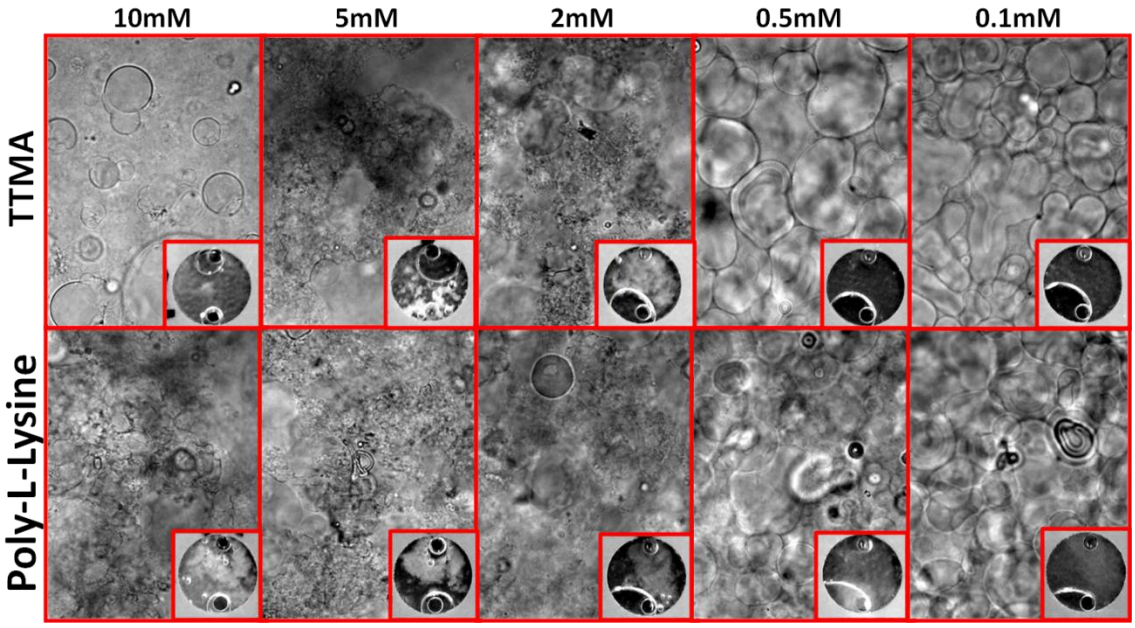

Figure 54. Vesicles exposed to varying concentrations of TTMA (top row) and poly-l-lysine (bottom row). The overall concentration of polymer in each sample is indicated above. Once added, the samples were allowed to sit for 1 hour to reach a steady state configuration. For reference, an image of the entire sample chamber is also provided in each case (inset). In many samples, the gel spans the entire system and is visible with the naked eye.

Using this data, we find that an optimal concentration of poly-L-lysine in solution is around 5 mM, and an optimal concentration of TTMA polymer in solution is around 2 mM. Surprisingly, we also find that in both cases there is a minimum concentration of polymer below which a gel does not form. Ultimately, we found that poly-L-lysine produced the largest gel over the widest range of concentrations, and decided to use this polymer as the primary binding agent in our gels.

These replacements greatly reduce the overall cost of the material, but the process of electroformation has a prohibitively low yield (only a few hundred microliters). Instead, we use a gentle hydration method that has been tailored for high-yield production (detailed in Chapter 6). In this procedure, lipid dissolved in chloroform was dried onto a 10ml glass test tube, and the tube was then filled with the sugar solution and placed in a 35-40º oven for 24-48 hours. Using this method, several identical test tubes could be coated with lipid and dried in tandem with little additional effort; depending on the number of test tubes used, the total volume of GUVs produced can easily exceed 10ml for a single batch. Ultimately, the amount of vesicles produced is directly proportional to the total surface area of glass that is coated with dried lipid. These vesicles were then diluted with a 180 mOsm glucose solution, and allowed to sit for up to 1 day; this allowed the vesicles to settle at the bottom of the glass, and the excess solution could be removed if desired.

Using this new preparation method in combination with our replacement materials, we can produce milliliter quantities of our vesicle gel material. The optimal procedure for mixing the high-volume vesicle suspension with the poly-L-lysine solution was determined through extensive trial and error by undergraduate student Ian Torres. In order to make the gel, we mixed a solution containing 1ml of 0.1% wt/vol poly-L-lysine, 5 mL of 175 mOsm sucrose, and 5 mL of 215 mOsm glucose. (The higher molarity glucose was to ensure the solution was osmotically matched with the GUVs.) This solution was added drop-wise into the bulk of a 15 mL sample of lecithin GUVs, gently stirring up the entire solution for a few seconds after each drop was added. Mixing the poly-L-lysine into the vesicle suspension took some degree of care; we needed to agitate the liquid enough for the poly-L-lysine to adhere to vesicles within the bulk of the fluid, but we also must avoid mixing with enough force to rupture any already-formed gel. Once the two solutions are combined, the gel is then allowed to settle for 24 hours. The results of this procedure can be seen in Figure 59; the resulting material is noticeably more opaque than the pure lecithin vesicles alone.

Figure 55. Several milliliters of vesicle gel in a glass vial, formed with PC lecithin vesicles with a poly-L-lysine solution. Image taken by student Ian Torres.

Once our procedure for forming large quantities of the gel had been developed, we could take real measurements of the mechanical properties of the vesicle gel. Our early experiments indicate that the stiffness of the material is in the range of ~1 Pa. For comparison, the stiffness of Jell-o is about 400 Pa. Additional work is still needed to determine which factors determine this stiffness value; indeed, the rheological properties of the gel are potentially dependent on the way the gel was formed. Factors such as the charge density and length of the binding polymer, the osmotic pressure of the vesicles, the concentration of polymer added, or the average size of vesicles in the gel.

We can also get a general idea about the stability of the gel; experiments show that the gel structure remains stable for roughly 5 to 6 days, suggesting it may actually prolong the stability of the lecithin-derived vesicles.

Conclusions

We have successfully developed a novel soft material with potentially highly customizable rheological properties: a macroscopically large aggregate of vesicles, forming a cohesive and semi-permeable gel network. In order to form the gel, we added a small volume of charged polymers into a suspension of vesicles formed using purified soy lecithin.

Its resulting cell-like structure is unique and distinct from other gel materials, and allows it to fully encapsulate a large volume of liquid within a series of robust interior

partitions. This feature makes it a potentially useful delivery vehicle for topical drugs, dyes, or other substances.

Interactions with 12nm nanoparticles

The interaction between nanoparticles and a lipid bilayer is fundamentally dependant on the diameter of the nanoparticles. As explained in Chapter 5, it costs less elastic energy per unit area for the membrane to wrap a large (low curvature) nanoparticle than it does to wrap a small (high curvature) one. From Equation 5, it is evident that the total contact energy required for a particle to be envelopment by a bilayer ought to decrease if the diameter of the adhered particle is increased (see also Figure 8).

To test this prediction, we performed a set of experiments with 12 nm Au-TTMA nanoparticles fabricated by students YiWei Lee and Li-Sheng Wang. These new particles are identical to the nanoparticles used in the previous experiments, except that they are slightly larger in diameter. Our 7 nm Au-TTMA nanoparticles required at least a 4.5% DOPS content in the membrane to be enveloped by it, and so it is likely that a lower DOPS content is required to wrap the 12nm particles. By explicitly mapping the transition point for these larger particles, we can learn a great deal about the relationship between the theoretical phase diagram in Figure 8 and real-world experiments.

Results

In practice, however, this turned out to be a particularly difficult experiment. The results from our early work are summarized in Figure 60. These results were not as clear-

cut as the results for the 7 nm Au-TTMA nanoparticles, as there were no obvious signs of a transition between the two different types of behaviors. Instead, both vesicle gels and vesicle disruption seemed to appear in every trial. We define the critical DOPS content marking the transition between vesicle gelation and vesicle disruption as the smallest mole fraction of DOPS for which the vesicle disruption behavior is observed to occur (specifically, the behavior documented in Figure 42). Using this definition, all the samples observed were above this threshold; both vesicle gels and burst vesicles were found in each sample tested (a few examples can be seen in Figure 60). However, for reasons outlined below, additional work is needed to positively identify this transition.

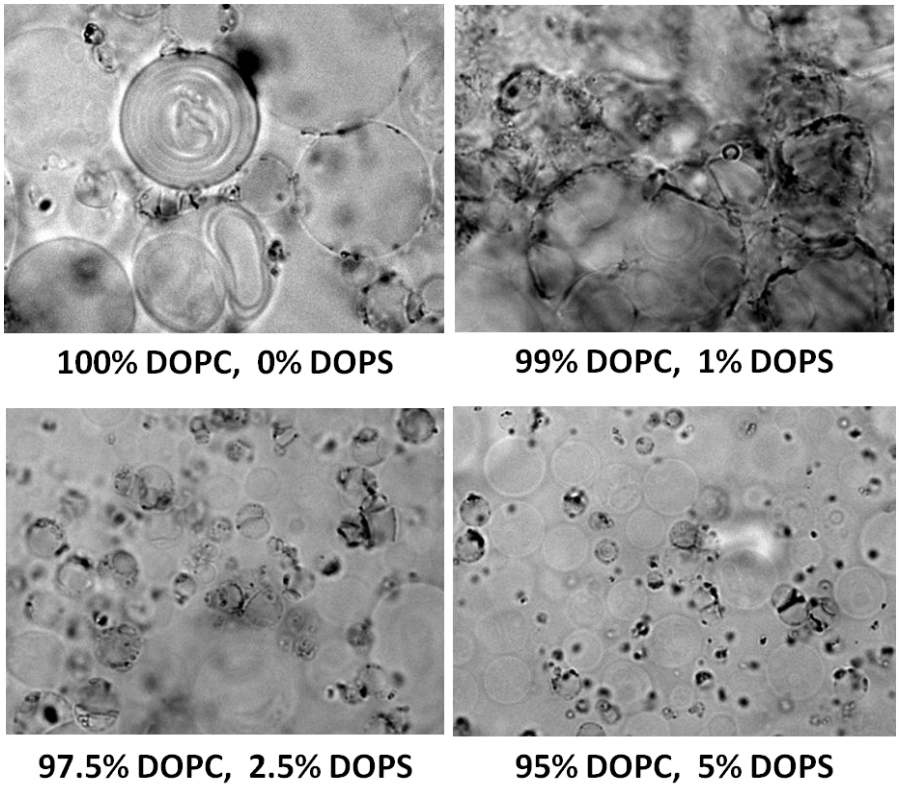

Figure 56. Adhesion of 12nm AU-TTMA nanoparticles as a function of the DOPS content of the vesicles, each viewed under a 40x objective lens.

A major issue in these experiments was caused by the avid binding of our 12nm nanoparticles with the surface of the glass coverslip at the bottom of the sample chamber during imaging. This adhesion was so strong, any nanoparticle-covered vesicle making contact with the coverslip was invariably destroyed; the nanoparticles seek to maximize their contact with the glass, forcing the vesicle to spread out thinner and thinner along the glass surface until the membrane ruptures. This fact makes it especially difficult to reliably identify which samples the disruption phenomena appear in; in the future, the glass used in these experiments will need to be treated to have a weakly cationic surface charge.

Despite these difficulties, in a few cases we were successfully able to observe the vesicle disruption phenomena. This behavior was nearly identical to the phenomena observed for the 7 nm nanoparticles, and is shown in Figure 61.

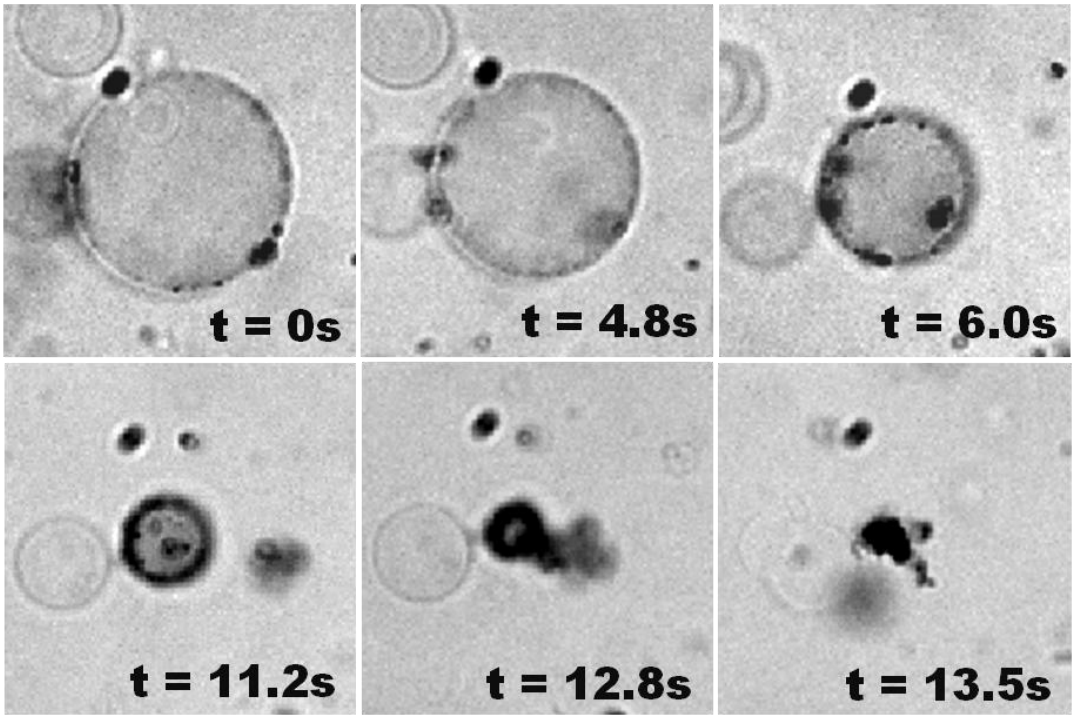

Figure 57. Disruption of 6% DOPS GUVs, caused by adsorption of 12nm Au-TTMA nanoparticles.

There are a few small differences between this data and the data in Figure 42. The disrupted vesicles exposed to the 12 nm particles still undergo the 'shrinking' phenomenon, where the radius of the vesicle steadily decreases until it fully ruptures. Of the 5 or 6 vesicles that unambiguously displayed this behavior, none appeared to have formed a pore on their surface. Dark clusters do seem to form on the surface of the vesicles. These vesicles also appear to form tubular structures after inversion, though the tubules are visibly shorter and narrower than the tubules formed by the 7 nm particles (Fig 61); the tubules formed by the 12 nm particles have an average diameter of 0.4 μm, compared to an average diameter of 1.5 μm for the 7 nm nanoparticles. Nevertheless,

significantly more data is needed before any quantitative comparison between the phenomenology of the two systems can be made.

Conclusions

Although the 12 nm particles are far more visible under dark field, their behavior is far less consistent than the 7 nm particles, making it more difficult to form a complete picture of their interactions with the membrane. They are, however, observably more destructive to the bilayer.

Notes

[1] D. Needham and D. Zhelev, in *Perspectives in Supramolecular Chemistry* (John Wiley & Sons, Ltd., 2007), p. 102.

[2] X. Chen, F. Tian, X. Zhang, and W. Wang, Soft Matter 9, 7592 (2013).

[3] B. J. Reynwar and M. Deserno, Soft Matter 7, 8567 (2011).

[4] A. Šarić and A. Cacciuto, Soft Matter 7, 1874 (2011).

[5] M. Deserno, Physical Review E 69 (2004).

[6] M. Deserno and W. M. Gelbart, The Journal of Physical Chemistry B 106, 5543 (2002).

[7] S. Li and N. Malmstadt, Soft Matter 9, 4969 (2013).

[8] O. Sandre, L. Moreaux, and F. Brochard-Wyart, Proceedings of the National Academy of Sciences 96, 10591 (1999).

[9] S. C. Hayden, G. Zhao, K. Saha, R. L. Phillips, X. Li, O. R. Miranda, V. M. Rotello, M. A. El-Sayed, I. Schmidt-Krey, and U. H. Bunz, J Am Chem Soc 134, 6920 (2012).

[10] B. J. Reynwar, G. Illya, V. A. Harmandaris, M. M. Muller, K. Kremer, and M. Deserno, Nature 447, 461 (2007).

[11] A. H. Bahrami, R. Lipowsky, and T. R. Weikl, Physical Review Letters 109 (2012).

[12] R. N. Frese, J. C. Pamies, J. D. Olsen, S. Bahatyrova, C. D. van der Weij-de Wit, T. J. Aartsma, C. Otto, C. N. Hunter, D. Frenkel, and R. van Grondelle, Biophys J 94, 640 (2008).

[13] R. Matthews and C. N. Likos, Physical Review Letters 109 (2012).

[14] A. Šarić and A. Cacciuto, Soft Matter 9, 6677 (2013).

[15] M. D. Haw, Physical Review E 81, 031402 (2010).

[16] R. P. Sear, S.-W. Chung, G. Markovich, W. M. Gelbart, and J. R. Heath, Physical Review E 59, R6255 (1999).

[17] Y. Yu and S. Granick, J Am Chem Soc 131, 14158 (2009).

[18] C. R. Scholfield, Journal of the American Oil Chemists Society 58, 889 (1981).

CHAPTER 9

SUMMARY AND FUTURE WORK

The work described in this thesis provides new insights into the ways that surface shape, elasticity, and morphology affect the assembly and interaction of adsorbed spherical particles. Our simulations of the self-assembly and the mechanical stiffness of colloidal cylinders uncovered geometric scaling laws relating the structure and stiffness of the lattice with the physical dimensions of the cylinder and the interactions between colloid particles. The relative simplicity of these simulations enabled us to explore the effects of a wide range of different particle and lattice types, and a more sophisticated approach could potentially continue to probe new questions beyond the scope of this thesis. Additionally, our experiments with adhesion of gold nanoparticles to unilamellar vesicles uncovered new and potentially useful behaviors, yet we have explored only two parameters of this highly multidimensional arena. Significantly more work is needed in order to build a complete description of the surface-reshaping effects caused by adhered particles.

This chapter provides an overview of the results of this thesis, as well as new and unanswered questions that arose during our experiments. We also suggest new experiments to further explore our findings.

Assembly and elasticity of cylindrical crystals

Cylindrical crystal self-assembly

We examined spherical particles constrained to the surface of a cylinder as a model system for understanding how frustration created by the incommensurability of the preferred packing with the available area can influence the stable solid structures found there. We found that a finite interaction length substantially broadens the range of cylinder radii over which stable and uniform crystals are found compared to hard spheres. In such cases, we found that that the cylinder stabilizes an oblique lattice structure, which is not found in equilibrium on a planar surface. We also found finite ranges of cylinder size that induce "line-slip phases," which are characterized by a helical defect that separates two regions with the same crystal lattice and orientation. The line-slip phase resembles structures previously found with hard spheres.[1,2] When the range of attraction was decreased relative to the sphere size, the area in parameter space over which stable and uniform crystals are found decreased and the line-slip structures became more prevalent. We found that these behaviors could be predicted with surprising accuracy using a simple one-dimensional model. The simplicity of this model allowed us to understand the basic mechanism at work in this geometry—an understanding which might be extended into the more general problem of self-assembling particles in strongly confined spaces.

Our work addresses the question of self-assembly of attractive particles with a hard-core repulsion and no net interaction when separated by a distance $r >> d$, but it did not address the more general problem of assembly of spheres with arbitrary types of interactions. This includes particles with purely repulsive interactions, purely harmonic

interactions, or more complex combinations thereof. Purely repulsive particles (eg. electrostatic interactions) in particular are potentially a quite useful avenue for study, but self-assembly of repulsive particles is dependent on the available surface area of the substrate they are confined to.[3-5] In other words, both the length *and* the circumference of the cylinder are important parameters when interactions are purely repulsive, implying our one-dimensional model is not applicable in this case. However, the general approach we have taken for examining the assembly of attractive particles—namely, that we simulated a wide variety of cylinder sizes and interaction potentials, categorized each of the resulting lattice types, then employed an energy minimization argument to describe their occurrence—may be similarly effective in this case. Conversely, describing the assembly of particles with mixed attractive/repulsive interactions may prove to be too complex for this strategy to be effective, since previous studies have shown these systems to be rather complicated.[6,7]

Additionally, the straightforwardness of our results suggests a potential practical application as a novel method for producing crystalline media of desired symmetry and orientation on cylindrical surfaces (Figure 62). Specifically, one should be able to tune both the structure and orientation of a developing crystal lattice by adjusting the ratio C/d. In doing so, one may be capable of producing crystalline fibers with a variety of desired properties, such as stiffness (as explored in Chapter 4) or even conductivity (a stretched oblique lattice has fewer contacts between neighboring spheres compared to the hexagonal case, hence the electrical resistance of these configurations ought to be higher). In practice, such crystals might spontaneously assemble more readily due to the

existence of the line-slip phase, through which crystals that nucleate in a metastable structure can reorganize into a more stable configuration.

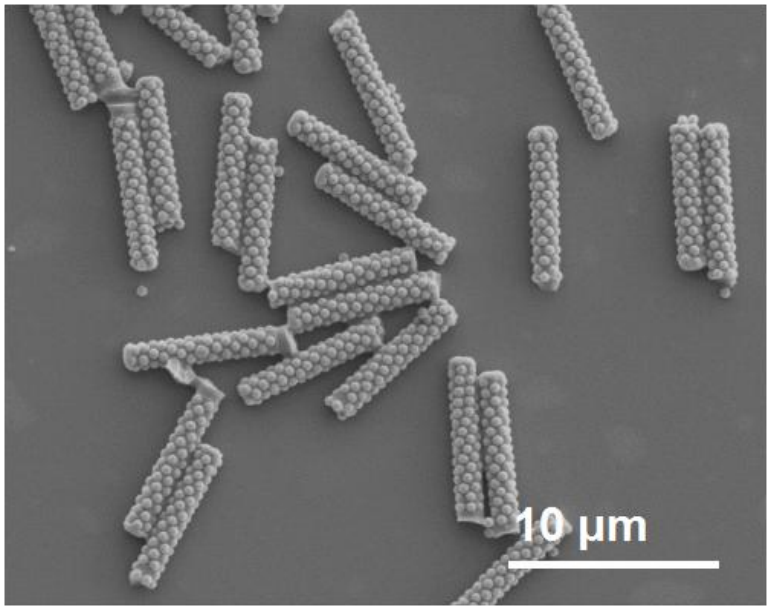

Figure 58. Image of fibers formed by depositing nanoparticles inside of a PDMS tube, then crosslinking into a solid object. These fibers display similar types of lattice structures to the ones found in our simulations. Furthermore, the symmetry of the lattice composing the fiber was found to depend directly on the diameter of the channel nanoparticles have been deposited into. Image taken by Gaoxiang Wang at the University of Pennsylvania, and part of an upcoming work under the direction of Prof. Shu Yang.

Experimental verification of the primary findings of our work—such as experiments with colloidal spheres adhered to a micropipette tip *via* depletion interactions, or experiments pulling a cylinder through a sphere-laden air/water interface—would be an important contribution in this avenue, particularly within the context of our investigations on the mechanical properties of these cylindrical lattices. Some early work has been undertaken by student Nabila Tanjeem, under Prof. Vinothan Manoharan at Harvard. In these experiments, 700 nm polystyrene spheres are made to

adhere to a tapered optical fiber *via* depletion. Early experiments show evidence of potential observation of a line-slip defect.

Cylindrical crystal stiffness

We next used MD simulations to explore the relationship between the bending elasticity of a cylindrical crystal and several of its other physical characteristics, including its diameter, the interactions between the particles in the lattice, the crystallographic angle θ, and the overall type of crystal lattice. The overall relationship between these quantities and the stiffness of the cylinder was summarized by an analytic equation of Young's modulus that captured nearly all of the relevant trends observed in our simulations.

We found that the Young's modulus, $Y^{(2D)}$, scales linearly with the second derivative of the interaction potential between the particles, evaluated at the potential minima *d*. Additionally, we found that thin cylindrical crystals have a lower Young's Modulus than large ones; this finding is unusual, because material properties such as stiffness are typically intrinsic to the material, and do not depend on physical size. We showed that the increase in elastic modulus is an intuitive consequence of the geometric arrangement of the particles in the crystal. A similar trend has been reported (both theoretically and experimentally) in single-walled carbon and boron-nitride nanotubes,[8-14] though the physical origin of this phenomenon had until now remained unexplored.

We also found that when a hexagonal cylinder is bent to a radius of curvature smaller than the critical value $R_c = \sqrt{3C^2 \cdot V"(d)/\epsilon}$, the stiffness of the cylinder is greatly

reduced. Though consistent for hexagonal lattices, this value was found to be different for hexagonal and line-slip lattices; the same behavior was observed in oblique and line-slip lattices, however not at the same critical value. Additionally, lattices with a line-slip structure undergo a dramatic and unusual structural change when the cylinder is bent beyond R_c, where the entire line-slip seam migrated to the inner bend of the lattice, toward the region with the most negative Gaussian curvature.

There is still much to explore in this work; more simulations still need to be performed in order to fully understand the nature of the crossover curvature R_c, especially to understand whether it's value can be predicted analytically. We would also like to further explore the idea that the appearance of locally-strained bonds between neighboring particles can act as an indicator of nonlinear elastic response. Specifically, it would be useful to carefully examine deformed lattices in other geometries (such as a stretched sheet or cone) for the appearance of similar features. Traditionally, one uses the appearance of topological defects as a reporter for plastic deformation, but if locally strained bonds consistently precede the formation of disclinations in the lattice—especially for stiff inter-particle interactions, where such behavior was most prominent—it could turn out to be a useful metric that has heretofore gone overlooked.

We would also like to perform simulations that include a nonzero Poisson's ratio. Throughout our work we assume the cross-section of the cylinder is unaffected by deformations, but this is quite untrue of most real materials. Since the cross-section of the cylinder is one of the most important parameters that determine the steady-state structure of the lattice, allowing this value to change dynamically during our simulations may reveal surprising results.

Similarly, it would be useful also to perform simulations that allow the rod to buckle as it is bent—a feature that would allow us to establish a realistic range of applicability to many of our findings for highly bent rods. For instance, we find that a system of Lennard-Jones spheres, when bent to a very high curvature, forms disclination pairs that separate into isolated 5-fold and 7-fold defects and migrate to regions of highest and lowest Gaussian curvature, respectively (Figure 63). This observation is quite interesting on its own, but if we were to find that a rod of Lennard-Jones particles will tend to buckle out of plane at curvatures far below the curvature where this behavior is observed, then it may not be physically significant.

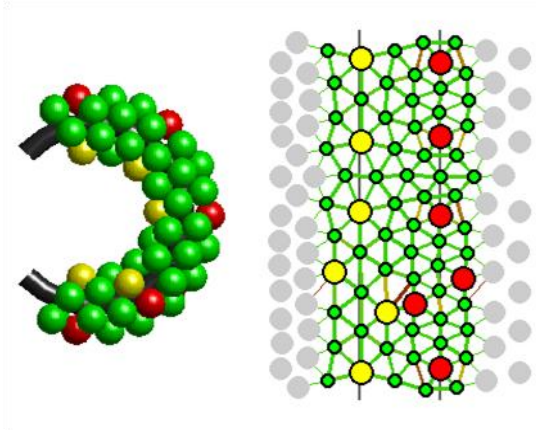

Figure 59. A [5,0] lattice of Lennard-Jones particles, bent to a curvature of $(C/4\pi R)^2 V''(d) \approx 2.5$. The particles with a 5-fold defect are labeled red, and 7-fold defects are labeled yellow. At this curvature, the defects migrate away from each other and line up on the inner and outer bend of the cylinder.

Effects of nanoparticle adhesion on a bilayer membrane

In these experiments, we exposed lipid bilayer membranes to cationic nanoparticles in an effort to understand how nanoparticle adhesion can reshape the

bilayer surface, a mechanism that could potentially be used to design novel responsive materials. To explore the phase space of this problem, we formed giant unilamellar vesicles, and adjusted their surface charge (and by extension, the adhesion energy of the nanoparticles) by tuning the molar ratio of zwitterionic DOPC lipids to the anionic DOPS lipids composing them. We also exposed them to nanoparticles of two different diameters.

Our primary finding in these experiments is that, at a critical threshold of roughly 4.5% mole fraction DOPS, the conformation of the nanoparticles adsorbed to the bilayer between undergo a phase transition. At DOPS concentrations below this critical value, nanoparticles weakly deform the vesicle surface, creating a patchy surface charge and leading to aggregation of the vesicles into a gel. At DOPS concentrations above this critical value, nanoparticles are fully enveloped by the membrane, causing the vesicle membrane to become loaded with adhered nanoparticles, ultimately leading to the destruction of the vesicle. We next discus each of these two cases separately, then reflect on further experimentation that could be performed to learn more.

Strong nanoparticle adhesion

In this regime, the strong adhesion energy between the particles and the membrane ostensibly defeats the energetic cost associated with deforming the bilayer around the particle, so adsorbed particles get enveloped by the membrane. This envelopment in turn causes the diameter of the vesicle to decrease, at a rate that is directly related to the rate of adhesion of free particles onto the bilayer. If the rate of adhesion is very high, the vesicle develops a large pore to equalize the rapidly changing

osmotic pressure, which then remains a stable feature on the nanoparticle-loaded vesicle surface. The diameter of the vesicle continues to decrease, until it reaches a point where it completely inverts itself, and the vesicle interior is forced out through the pore on its surface, or, if no pore has developed, the surface violently ruptures beforehand. As the vesicle is inverted, it reveals long tendril-like tubules, presumably completely loaded with nanoparticles.

This process of disruption is highly repeatable, but much of the information we have gathered on its features has been through qualitative extrapolation from video sources. A great number of experiments would be helpful in collecting qualitative data about this process. In particular, cryo-EM experiments on samples of vesicles exposed to nanoparticles (at any stage of the disruption process) would be enormously informative. First, it would help to shed light on the arrangement of the nanoparticles on the vesicle surface, which form dark clusters that are just beyond the range of resolution of our microscope optics. It may also help explain how and why the vesicle tubulation occurs—it is unclear at this point if the tubules exist inside the vesicle prior to inversion, or whether they form as a product of the nanoparticle-laden bilayer being forced through a small opening on the vesicle surface. We also do not yet fully understand the structure of these tubules, and cryo-EM may help shed light on their appearance on the nanometer scale.

Additionally, through our analysis in Chapter 6 we have been able to make many inferences about the impact of the nanoparticle adsorption rate on the vesicle disruption process, but without knowing the ambient nanoparticle concentration it is hard to draw any quantitative conclusions. Therefore, experiments where the ambient nanoparticle

concentration is well-controlled would be very informative for verifying that the rate of vesicle collapse is indeed related to the nanoparticle adhesion rate, as well as further exploring our finding that the pore formation is directly related to the rate of decrease of the vesicle radius. Experimentally, this can be accomplished in a few ways. First, our experiments could essentially be repeated using fluorescently labeled particles in place of our Au-TTMA particles. In such an experiment, the ambient nanoparticle concentration could be approximately calculated by measuring the background fluorescence in each image. Secondly, nanoparticle concentration could be controlled through micropipette aspiration, by aspirating a vesicle in a nanoparticle-free environment, and depositing it into a new sample chamber with a known concentration of nanoparticles.

Weak nanoparticle adhesion

In this regime, the nanoparticles only weakly deform the membrane, remain on the surface of the vesicles once they adsorb, and act as an adhesive bridge once two nanoparticle-laiden vesicles come into contact with one another. The rate of adhesion of two vesicles (once they have come into contact) can be quantified by total contact surface area between the two, and increases at a rate that is inversely proportional to the time elapsed since the vesicles first made contact. Over time, many adhered vesicles join together to make a gel network of adhered vesicles.

We can leverage this behavior to our advantage to design a new material, consisting of a very large, macroscopically sized, continuous vesicle gel network. By using a charged polymer such as poly-L-lysine in place of the nanoparticles, and PS-enriched soy lecithin powder to fabricate large volumes of vesicles, we were able to make

several tens of milliliters of this gel material at once. More work can be done towards optimizing the production of this material, however; for one, the rate of production of the lecithin-derived vesicles depends on the total surface area of glass that the dissolved lecithin powder is deposited on (Figure 64, more detail on this process is found in Chap. 5 and 6). Potentially, one could maximize this surface area by instead depositing the lecithin in bulk on a large number of glass spheres, and suspending all the spheres at once in sucrose buffer. Additionally, in its current state, actually depositing the lecithin onto the glass surface is by far the most labor-intensive step in the process, and it may be possible to rapidly speed up this step by designing a more efficient process.

Figure 60. Large vesicle gels. *Left panel:* PC lecithin vesicles formed by gentle hydration, in a container that holds several glass slides in an effort to scale up production. *Right panel:* the same vesicles, extracted and placed in a 25 mL glass jar. Images taken by student Ian Torres.

This new material is potentially very useful, but there are still experiments that should be done to learn which factors determine its physical properties—its stiffness, for example, likely depends on the concentration and charge density of polymer added into suspension, and on the average size and composition of the vesicles. If we can understand how these factors contribute to its stiffness, then we can potentially tune the stiffness of the gel as desired. Doing so requires performing many rheological measurements on different sets of gels, varying each of the above parameters. Some early work performed by student Ian Torres suggests that the stiffness of the material can be greatly enhanced by using highly charged cationic polymer Polydiallyldimethylammonium chloride (PolyDADMAC), enough that it is strong enough to be removed from solution and support its own weight when placed on a glass slide (Figure 65). Gel could also be fabricated using polymersomes rather than lipid vesicles for additional robustness and customization.

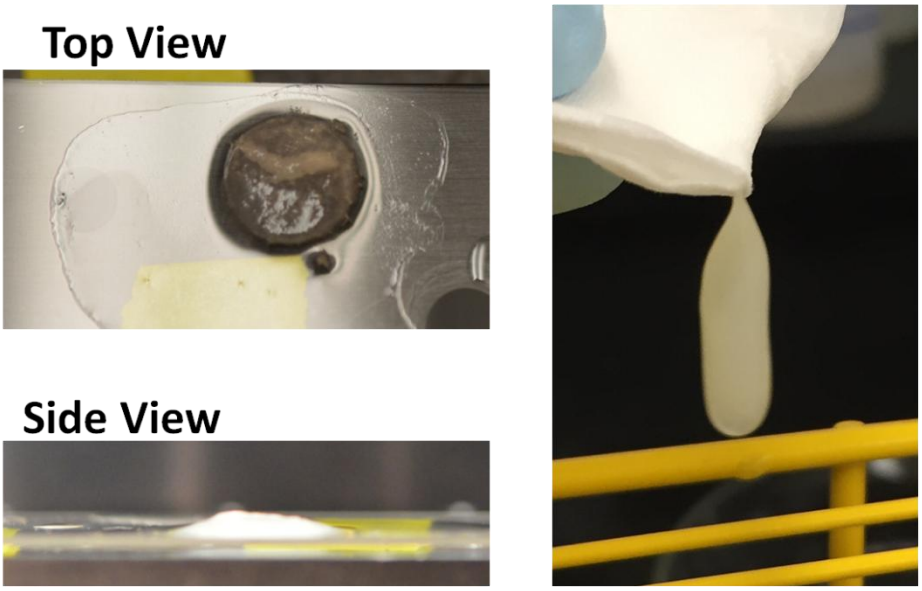

Figure 61. PC lecithin vesicles, adhered into a gel by adding the cationic polymer PolyDADMAC into solution, then removed from solution and placed onto a glass slide. The right panel shows the same gel droplet stuck to a Kimwipe, illustrating its apparent rigidity. All images taken by student Ian Torres.

Furthermore, there is still experimental work to be done to explore the potential novel functionality of our liposomal gel material. Since the individual vesicles remain intact within the gel, in principle they are capable of fully encapsulating multiple different species in solution inside the gel. One could imagine forming two different sets of vesicles, each one encapsulating a different reactant polymer. The vesicles could then be dialyzed, mixed, and then made to form a vesicle gel. The two different species of polymer would not react with one another until the gel was ruptured in some way, causing their release and mixture.

Further experimentation

Finally, additional work may be useful in better understanding how nanoparticle adhesion can reshape a bilayer membrane in general. More data and careful experimentation is necessary to understand how the 12 nm Au-TTMA nanoparticles affect the membrane, and whether or not the difference in nanoparticle size lowers the critical concentration of DOPS lipids required for the bilayer to envelop the adsorbed particles. It may also be useful to test the effects of other factors as well, such as using anionic nanoparticles on a cationically charged membrane, or repeating our experiments with different types of lipids entirely. Lastly, although our attempt to quantify the adhesion energy between the nanoparticles and the bilayer proved unsuccessful, they may be repeated with larger or more weakly charged nanoparticles—both factors that make the nanoparticles less likely to disrupt the vesicles, making the success of these tests more feasible.

Notes

[1] A. Mughal, H. Chan, and D. Weaire, Physical Review Letters **106** (2011).

[2] A. Mughal, H. Chan, D. Weaire, and S. Hutzler, Physical Review E **85** (2012).

[3] K. L. Kohlstedt, G. Vernizzi, and M. Olvera de la Cruz, Physical Review E **80,** 051503 (2009).

[4] E. C. Oğuz, R. Messina, and H. Löwen, EPL (Europhysics Letters) **94,** 28005 (2011).

[5] F. J. Solis, G. Vernizzi, and M. Olvera de la Cruz, Soft Matter **7,** 1456 (2011).

[6] K. L. Kohlstedt, G. Vernizzi, and M. Olvera de la Cruz, J Phys Condens Matter **21,** 424114 (2009).

[7] S. Srebnik and J. F. Douglas, Soft Matter **7,** 6897 (2011).

[8] P. A. B. I. Yakobson, Carbon Nanotubes, Topics Appl. Phys **80,** 287 (2001).

[9] T. Chang and H. Gao, Journal of the Mechanics and Physics of Solids **51,** 1059 (2003).

[10] E. Hernández, C. Goze, P. Bernier, and A. Rubio, Applied Physics A **68,** 287 (1999).

[11] L. Jiang and W. Guo, Journal of the Mechanics and Physics of Solids **59,** 1204 (2011).

[12] C. Li and T.-W. Chou, International Journal of Solids and Structures **40,** 2487 (2003).

[13] A. E. Tanur, J. Wang, A. L. Reddy, D. N. Lamont, Y. K. Yap, and G. C. Walker, J Phys Chem B **117,** 4618 (2013).

[14] J. R. Xiao, B. A. Gama, and J. W. Gillespie, International Journal of Solids and Structures **42,** 3075 (2005).

APPENDIX A

NANOPARTICLE BINDING ON LUVS

In order to learn more about the parameters that govern how nanoparticles adhere onto and reshape bilayer membranes, we would like to directly measure the contact energy between an individual nanoparticle and the membrane itself. Particularly, we would like to understand how the contact energy is affected by the lipid content and osmotic pressure in the vesicle. To accomplish this, we perform experiments exposing large unilamellar vesicles (LUVs, 10-50 nm in diameter) to cationic gold nanoparticles (7 nm in diameter, including TTMA ligand as described in Ch. 5). By carefully measuring the fraction of nanoparticles that bind to the vesicles, we hoped to use the Langmuir adsorption equation to estimate the nanoparticle adsorption energy. By adjusting the lipid content and osmolarity of the vesicles, we aimed to quantitatively measure how these parameters affect nanoparticle adhesion. This information might subsequently be used to estimate how the nanoparticles deform and reshape the bilayer membrane. As part of the thesis, a method of analyzing the bound fraction of nanoparticles was successfully developed (Ch. 5). Ultimately, however, these experiments were not successful because we found that particle binding led to major changes in vesicle shape, and so the results were difficult to interpret. These studies spurred another series of studies that will be examined in greater detail in Chapter 6.

Methods and Materials

In these experiments, we prepare LUVs by extrusion, and then expose these vesicles to nanoparticles. Vesicles with bound nanoparticles are significantly heavier than anything else in solution, and they can be separated out by centrifugation. Once the LUVs with bound nanoparticles are removed, we can re-suspend these in a small amount of liquid, and then measure the total concentration of bound nanoparticles using absorption spectroscopy as described in Chapter 6. We then repeat this experiment for LUVs with different lipid composition and osmotic pressures to build a picture of how the bound fraction of nanoparticles varies with these parameters.

All of our experiments were performed using the same batch of nanoparticles; 7 nm diameter nanoparticles with a 2 nm gold core, coated with cationic TTMA ligands, as illustrated in Figure 34. This stock nanoparticle solution was produced by YiWei Lee and Li-Sheng Wang in Prof. Vincent Rotello's laboratory, and had a concentration of 10 mM of nanoparticles, suspended in water.

LUV Formation

We prepare LUVs by extrusion using the procedure detailed in Chapter 5. The lipids used in these experiments are DOPC and DOPS (Figure 4). The hydrophilic head group of DOPS is anionic, meaning we can adjust the surface charge of the LUVs by adding a small percentage of DOPS to the zwitterionic DOPC lipids before formation. In these experiments, the lipid composition of the extruded vesicles ranged between 0% mole fraction DOPS with 100% DOPC, to 20% DOPS and 80% DOPC. The DOPS lipids have a negative intrinsic curvature and cannot form a stable bilayer by themselves, and adding more than even 15-20% DOPS with DOPC severely limits the stability of the

extruded vesicles.[1] This ratio served as the upper limit to the amount of anionic charge that could be added to the LUVs during our experiments.

All of our LUVs were extruded in 1 mL of a solution of 200 mOsm glucose, and then let sit for 24 hours before use to allow the glucose concentration in each LUV fully equilibrate and reach a uniform osmotic pressure.[2,3] To adjust the osmolarity of the LUVs in the solution, the extruded LUVs can then be diluted with a 1:1 ratio of glucose/sucrose solution with a different concentration of glucose; a concentration lower than 200 mOsm makes the vesicles stiff and taught, and a concentration greater than 200 mOsm makes them loose and floppy. More specifically, the osmotic pressure in the LUVs can be calculated as the difference between the difference in osmolarity between the fluid encapsulated by the vesicles and the bulk fluid they are suspended in,

$$\Delta c = c_{\text{internal}} - c_{external}, \qquad \text{(Eq. 32)}$$

where c_{internal} = 200 mOsm. Once diluted, the vesicles must be used within 4-6 hours, otherwise the diffusion of glucose across the bilayer membrane will slowly return the osmotic pressure of the vesicles to zero. In principle the osmolarity of the LUVs can be adjusted to a value of ±60 mOsm L^{-1}, beyond which they will simply rupture (or 'lyse'). By combining the preceding two techniques, we can adjust both the osmotic pressure and the surface chemistry of our LUVs before exposing them to nanoparticles.

Binding energy measurement

In general, many properties of the system are already known: the bending energy of a DOPC vesicle (κ) is well known, and the average osmotic pressure (σ) of the vesicle can be calculated from Equation 32, and is known accurately for a finite period of time

after preparation. The contact energy of the particles with the surface, on the other hand, is a quantity we would like to measure experimentally. Although tricky to determine, knowing this parameter is necessary in order to quantitatively compare any results with theory (as outlined in Chapter 1 and illustrated in Figure 8). It can be done, however, using the Langmuir adsorption equation.

We derive this equation quickly by using a drastically simplified model of our system; namely, we assume the membrane has N_S independent binding sites, and that there is some bulk concentration c of nanoparticles diffusing around as a gas in suspension. If a nanoparticle and binding site have a total energy E= ϵ when a particle is adsorbed and an energy of E=0 when separated, we can write down the probability that a single adhesion site on the membrane surface will be occupied as

$$P_{occupied} = \frac{(0)\cdot 1+(1)\cdot e^{-\beta(\epsilon-\mu)}}{1+e^{-\beta(\epsilon-\mu)}}, \qquad \text{(Eq. 33)}$$

where μ is the chemical potential of the adsorbed state. In equilibrium, μ must be equal to the chemical potential of the nanoparticle gas. We next approximate μ as being equivalent to the chemical potential of an ideal gas;

$$\mu = \mu_0 + k_b T \cdot \ln(c)\,. \qquad \text{(Eq. 34)}$$

Here, μ_0 is used to describe the specific features of the particular nanoparticles in solution, and is assumed to be a complicated function depending on many of the system parameters. Because we have expressed the probability of a single site being occupied, we can write the expected density of bound particles, n, as

$$n = \frac{c\cdot e^{-\beta\epsilon}}{A+c\cdot e^{-\beta\epsilon}}, \;\; where \;\; A = e^{-\mu_0}\,. \qquad \text{(Eq. 35)}$$

Thus, by measuring the fraction of particles bound to the membrane as a function of the concentration of particles, we ought to be able to estimate the binding energy ϵ.

Such a measurement will tell us the total contact energy of the nanoparticles with the membrane, but it will *not* tell us the contact energy density, ω. Recall that, as defined in Eq. 1, the total contact energy between the particle and the membrane, ϵ, is written as $\epsilon = (2\pi a^2 z)\omega$, where a is the diameter of the particle and z is the penetration depth of the particle in the membrane (Figure 7). In theory we can use this equation for ϵ to calculate ω, but we unfortunately do not have a good way of experimentally measuring the penetration depth of the particle, z. If, however, we assume that z is equal to its approximate equilibrium value z_{eq} (Equation 4), we can insert this value into our expression for ϵ in Equation 1, and find that

$$\epsilon \approx \frac{2\pi\omega}{\sigma}(\omega a^2 - 2\kappa). \qquad \text{(Eq. 36)}$$

In principle, the stiffness κ and tension σ in the membrane are known quantities, and hence we can calculate ϵ by repeating the experiment described above with groups of LUVs having varying values of ω and σ. Once all parameters of the system are known, we can begin to compare our experimental results with existing theoretical predictions.

Sample preparation and centrifugation

For each different sample being examined, three identical samples were simultaneously prepared for centrifugation and analysis. This practice allowed us to calculate the average concentration of bound nanoparticles across all three samples to increase the accuracy of our results. However, the language used in the following sections will describe the preparation and analysis of one single sample, even though in each case three identical samples are being used.

To prepare one single sample, 35 μL of LUVs (this volume includes the 1:1 dilution with solution from the previous step) was first pipetted into an Eppendorf tube. Next, stock nanoparticle solution is mixed. The osmolarity of this solution must match the overall concentration of the LUV solution, and so it is useful to prepare 1 mL or so of the correct sugar solution—we mix 500 μL of 200 mOsm glucose with 500 μL of whichever concentration of glucose was used to dilute the LUVs with, then vortex for 1 minute. We next add 1 μL of nanoparticles with enough glucose/sucrose solution to reach the desired concentration of nanoparticles, typically between 30 and 100 μL. We chose 1 μL as the standard volume of nanoparticles to add into the solution because it is the smallest volume that could be reliably measured with our micropipettes. We next vortex the nanoparticle suspension for 1 minute, then sonicate for an additional minute.

We then added and mixed 15 μL of nanoparticle solution to our single LUV sample. This was done very slowly and gently, adding first from the bottom of the Eppendorf and moving the micropipette upwards through the LUV sample as the nanoparticles were added, then repeatedly gently sucking up more liquid from the sample and adding it back in to mix the two together. This was found to be the least destructive way to mix the nanoparticles with the LUVs. Finally, once all samples were prepared, we placed all the samples onto a shaker at minimum speed for about 2 hours, to gently agitate the sample and allow it to quickly reach a steady state.

Next, the sample was centrifuged at 8000 RPM for 60 minutes using a Labofuge 400 centrifuge (Heraeus Instruments). Afterward centrifugation, the nanoparticle-covered LUVs have pelleted to the bottom of the Eppendorf, and the supernatant containing the unbound nanoparticles can be removed. To do so, 48μl was carefully removed from the

sample using a micropipette, making sure not to disturb the pellet. The supernatant was then pipetted into a new Eppendorf, and placed into an oven at 40 ºC for several hours to evaporate the water. This was done to increase the nanoparticle concentration in the re-suspended supernatant, which is otherwise much too low to detect. Once all the supernatant liquid had evaporated away, we added 8µl of deionized H_2O, then vortexed at high speed for 1 minute and sonicated for 3-5 minutes.

We then added 6µl of deionized H_2O to the pellet (this bursts any remaining LUVs), and sonicated for 3-5 minutes to break up the pellet. This gave us two 8 µL samples; one of the pellet, and the other of the supernatant. We next determine the nanoparticle concentration in each using the spectrographic analysis technique explained in detail in Chapter 6.

Results and analysis

Measuring the contact energy

We specifically wanted to measure the way that the osmotic pressure and surface charge of a vesicle will dictate the contact energy between a nanoparticle and the bilayer. To first measure the contact energy of one particular type of vesicle with the nanoparticles, we made use of the Langmuir adsorption equation; this required us to measure the fraction of nanoparticles that bind onto a fixed volume of LUVs as a function of the concentration of nanoparticles in solution. As an initial benchmark, we measured this value for pure DOPC LUVs with no applied osmotic pressure (i.e., with 200 mOsm glucose in both the interior and exterior of the LUVs).

To do so, we first prepared a batch of LUVs by extrusion in a 200 mOsm glucose solution, and then diluted them in the same solution by a factor of 4. (This roughly corresponds to a total of 1.7×10^9 LUVs/μL.) We then prepared a set of 6 samples of these LUVs of 35 μL each, then added a different concentration of nanoparticles to each sample (detailed in Table 1). We then centrifuged these samples as explained in the previous section and in Chapter 5.

Sample #	μL NPs	μL glucose solution	NP stock conc. (mM)	μL NP stock added	NP:LUV ratio
1	1	140	0.07	15	1
2	1	56	0.18	15	25
3	1	28	0.34	15	50
4	1	14	0.67	15	100
5	2	13	1.33	15	200
6	5	10	3.33	15	500

Table 1. Concentration of Nanoparticles exposed to each set of LUVs. The volume of nanoparticles and volume of 200 mOsm glucose solution used to make each stock nanoparticle suspension is given in the 2nd and 3rd columns. Once mixed, a total of 15 μL of this stock solution was added to 35 μL of LUVs in each case. The approximate ratio of nanoparticles to LUVs is given in the final column. Assuming the LUV's have an average diameter of 50 nm, a total of about 200 nanoparticles adhered to a single LUV roughly corresponds to the surface being fully packed with particles.

After centrifugation, a small dark brown spot was clearly visible at the bottom of most of these samples, indicating that the nanoparticles had bound to the LUVs and formed a pellet during centrifugation. Each pellet was re-suspended in water and analyzed using a spectrometer. The results from this analysis indicated that, perplexingly, none of the re-suspended supernatant pellets had any nanoparticles in them (Figure 66).

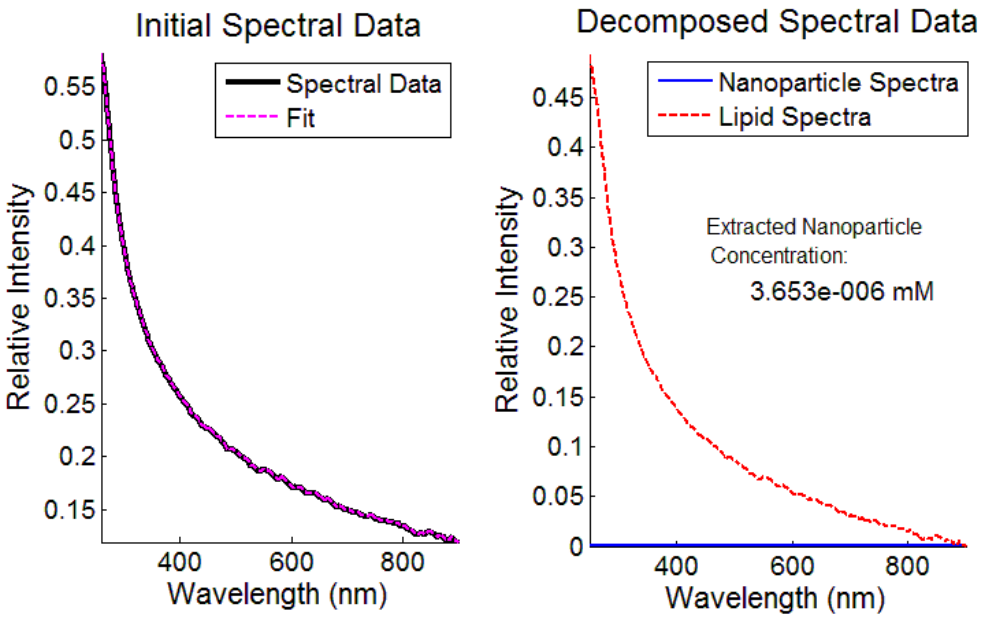

Figure 62. Analysis of one sample spectra from sample #4 in Table 1. Our analysis indicated that it did not contain a detectable concentration of nanoparticles.

This result was pervasive throughout all of our samples. Despite the fact that the re-suspended pellet visibly contained nanoparticles, no spectral trace could be measured. In each case the absorbance spectra from the sample was found to perfectly match the characteristic signature of the rehydrated lipids. We are unsure why this should be the case, since the minimum detectable concentration of nanoparticles was previously found to be close to 200 μM (as detailed in Chapter 5). This value roughly corresponds to a nanoparticle-to-LUV ratio of 25; for comparison, an LUV with 200 adsorbed nanoparticles corresponds to a fully packed surface. Thus, the concentration of nanoparticles in the pellet ought to have been detectable by our methods. In addition, after repeating this experiment several times it became clear that there was an issue with repeatability, insofar as identical samples frequently did not consistently form a pellet.

Although these particular experiments did not work, in principle the method used to determine the contact energy is sound. It may be useful for future students to reattempt such measurements with larger (say, 20-40nm) gold nanoparticles, which are much easier to detect at far lower concentrations.[4] As was explained in Chapter 6, adhesion also triggers lateral interactions among particles as well as deformation of the vesicle shape, which complicate the use of the Langmuir adsorption equation—which is of limited applicability when particles are bound to more than one vesicle, or when the adhesion of particles decreases the number of available binding sites in a nonlinear fashion.

Mapping adhesion strength with osmotic pressure and DOPS content

Although our quantitative measurements were not successful for the reasons explained in the previous section, since the actual nanoparticle pellet is visible by eye once the samples have been centrifuged, we can still make some qualitative observations about how osmotic pressure and surface charge affect the binding rates.

Sample #	µl LUVs	µl 200 mOsm solution	µl 600 mOsm solution	µl H2O	Δp (mOsm)
1	20	5	0	5	30
2	20	8	0	2	10
3	20	10	0	0	0
4	20	5	2	3	-10
5	20	8	2	0	-30

Sample #	µl NPs	µl 200 mOsm solution	µl 600 mOsm solution	µl H2O	Δp (mOsm)
1	1	2	2	5	30
2	1	3	2	4	10
3	1	8.5	0.5	0	0
4	1	1	3	5	-10
5	1	2	3	4	-30

Table 2. Table of the applied osmolarity of each LUV sample. 10ul of solution was mixed and vortexed before being gently added to 20 μL samples of LUVs (top). To match the osmolarity of each sample, 10μl of nanoparticles and solution were mixed, vortexed, and sonicated (bottom). When deciding how to mix the sugar solution, the quantities of each species were chosen to avoid needing to measure out volumes less than 1 μL.

We first examine the effects of osmotic pressure. We prepared a sample of LUV's composed of 95% DOPC lipids and 5% DOPS lipids (measured by mole fraction) in 200mOsm glucose solution, and diluted them in an identical 200 mOsm glucose solution with a 2:3 ratio. We then prepared several 20 μL samples of these LUVs, and each sample was diluted in 10 μL of a different concentration glucose solution (Table 2, top). We then added 1 μL of nanoparticles to 9 μL solutions of solution, matching the osmotic pressure of each sample (Table 2, bottom). These were then vortexed for 1 minute and sonicated for 3 minutes, and then 10 μL of each nanoparticle solution was added to its corresponding LUV sample. This works out to a ratio of about 120 nanoparticles per LUV. After centrifugation, an image was taken of each sample pellet using a cell phone camera (Figure 67). Each of these samples was also analyzed spectroscopically, but just as before, no nanoparticles could be detected.

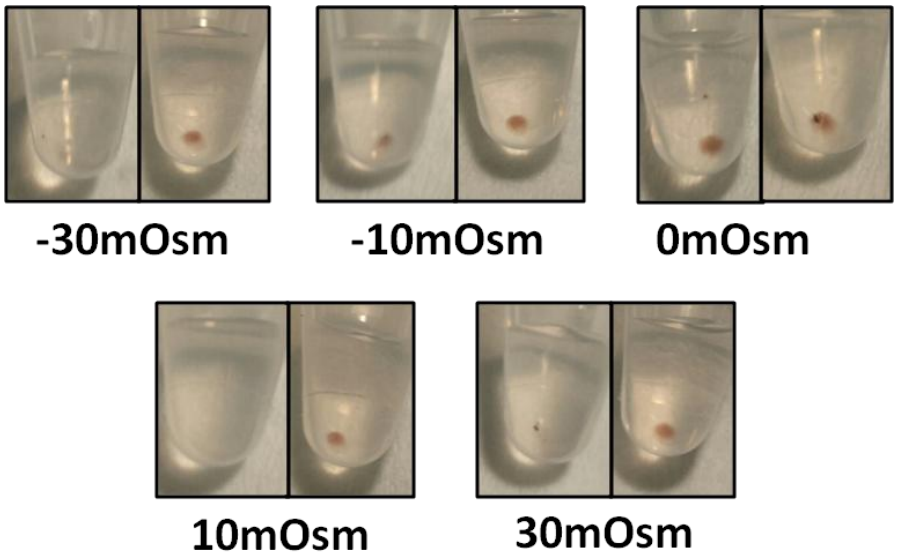

Figure 63. Centrifuged pellets containing DOPC LUVs of different osmolarity with adhered Au-TTMA nanoparticles. Two separate samples are pictured for each osmolarity. There does not appear to be any discernible trend linking the osmolarity of the LUVs with the adhesion of the nanoparticles.

As can be seen from Figure 67, there does not appear to be any clear relationship between the osmolarity of the LUVs with the size or the opacity of the pellet. This experiment was repeated several additional times with no observable difference in result. As you will see, the finding that osmolarity does not impact nanoparticle adhesion was corroborated by additional experiments discussed in the next chapter.

We next examine the effects of surface charge on the LUVs. To do so, we add a small amount of anionic DOPS lipid to the vesicles; higher DOPS content leads to stronger adhesion from the cationic Au-TTMA nanoparticles. We extruded 4 different sets of LUVs, each containing a different mole fraction of DOPS.

Following the same basic procedure as in the previous experiment, we prepared 35 μL samples of these LUVs in 200 mOsm glucose solution. We then added 1 μL of

nanoparticles to 15 μL solutions of 200 mOsm glucose solution, then vortexed for 1 minute and sonicated for 3 minutes. 15 μL of each nanoparticle solution was added to each LUV sample. Once more, an image was taken of each sample pellet using a cell phone camera after centrifugation (Figure 68).

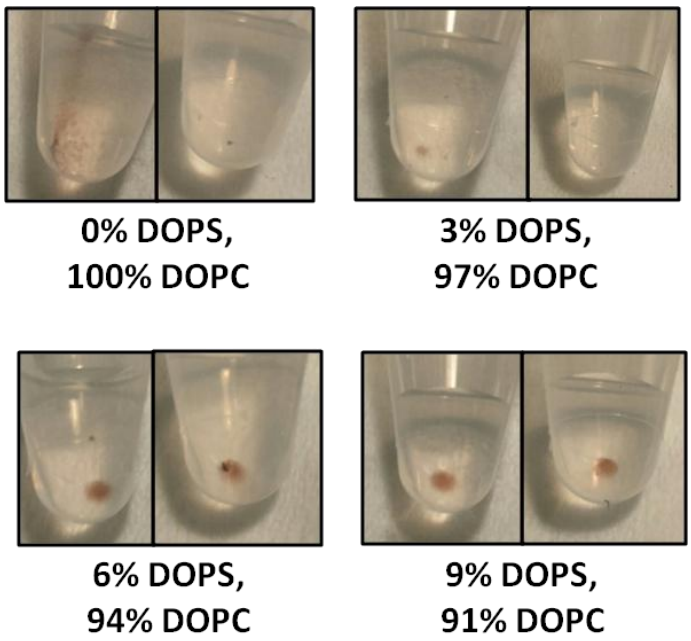

Figure 64. Centrifuged pellets containing LUVs of different anionic surface charge, with adhered cationic Au-TTMA nanoparticles. The two samples with a higher DOPS content have a significantly larger and more obvious pellet.

Unlike the osmolarity of the LUV, the amount of DOPS lipid in the vesicles has an unambiguous and measurable impact on the binding of the nanoparticles. Interestingly however, there appears to be a threshold value of DOPS composition needed for a pellet to form, since the samples with 0% and 3% DOPS did not for a pellet whereas the samples with 6% and 9% did. This particular observation is a primary focus of discussion in Chapter 6.

To get a better idea of what the impact of the increased DOPS content might be, we imaged a similar set of samples using dark-field microscopy. Using dark-field illumination, only the light that scatters off of the sample is imaged with the camera, appearing brightly against a dark background. With this method, highly reflective objects appear quite brightly in image. Although individual 7 nm gold nanoparticles are too small (and individual LUVs are too transparent) to see using dark field, a single LUV that is coated in adhered gold nanoparticles ought to be both large and reflective enough to be visible (Figure 69).

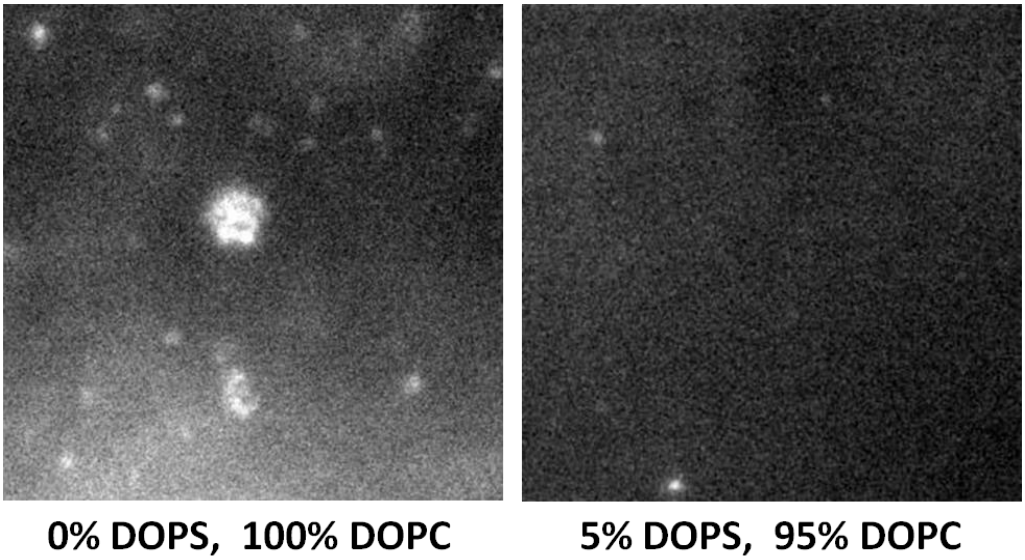

Figure 65. Dark-field image of LUVs with adhered nanoparticles. In the left panel, with no DOPS in the vesicles, large clumps of aggregated LUVs are visible. In the right panel, with a high amount of DOPS in the vesicles, LUVs with nanoparticles are just barely visible.

Paradoxically, even though no pellet formed for the 0% DOPS LUVs, large nanoparticle-laden aggregates of vesicles were visible. It is unknown why these

aggregates did not sediment; even when centrifuged for over 2 hours no visible pellet ever formed. Conversely, the 5% DOPS LUVs formed an obvious pellet, despite there being no indication of adhesion when viewed under dark field illumination. At the very least, these observations (particularly the existence of aggregates) strongly imply that the conditions needed to apply the Langmuir adsorption equation to analyze our results—namely, that the binding is not co-operative and that each nanoparticle binds onto one well-defined binding site—is likely not to be the case.

In order to better understand this strange behavior, we next attempted to duplicate these experiments using much larger vesicles (50-100 μm), so that the effects of the adhesion of the nanoparticles could be both clearer and observable under bright-field microscopy. The outcome of these experiments is detailed in Chapter 6.

Conclusions

For reasons we did not anticipate, the interactions between the lipid bilayer and the LUVs were strong enough to deform the membranes and frustrate quantitative analysis of bound fraction. However, in principle the spectroscopic techniques outlined in this chapter and in Chapter 6 ought to still be a viable method for quantitatively measuring the interactions between nanoparticles and a membrane, provided that the particles do not substantially change the membrane morphology. Experiments were not successful for our 7 nm Au-TTMA nanoparticles, but perhaps larger cationic nanoparticles with a weaker charge density would be more successful.

More importantly however, the unusual behavior observed for LUVs exposed to these nanoparticles prompted us to repeat our experiments using giant unilamellar

vesicles (GUVs). Because these investigations showed vesicle morphology, they were successful and they led us to a more complete understanding of why the results of our experiments with LUVs turned out the way that they did. In the next chapter, we detail all of our findings for these experiments.

Notes

[1] C. Herold, G. Chwastek, P. Schwille, and E. P. Petrov, Langmuir **28,** 5518 (2012).

[2] B. Mui, L. Chow, and M. J. Hope, in *Methods in Enzymology*; *Vol. Volume 367* (Academic Press, 2003), p. 3.

[3] J. B. Hutchison, A. P. K. K. Karunanayake Mudiyanselage, R. M. Weis, and A. D. Dinsmore, Soft Matter **12,** 2465 (2016).

[4] P. K. Jain, K. S. Lee, I. H. El-Sayed, and M. A. El-Sayed, The Journal of Physical Chemistry B **110,** 7238 (2006).

REFERENCES

Alberts, B. (2002). Molecular biology of the cell. New York, Garland Science.

Amir, A. and D. R. Nelson (2012). "Dislocation-mediated growth of bacterial cell walls." Proceedings of the National Academy of Sciences **109**(25): 9833-9838.

Anderson, V. J. and H. N. W. Lekkerkerker (2002). "Insights into phase transition kinetics from colloid science." Nature **416**(6883): 811-815.

Angelova, M. I., et al. (1992). Preparation of giant vesicles by external AC electric fields. Kinetics and applications. Trends in Colloid and Interface Science VI. C. Helm, M. Lösche and H. Möhwald. Darmstadt, Steinkopff**:** 127-131.

B. I. Yakobson, P. A. (2001). "Mechanical Properties of Carbon Nanotubes." Carbon Nanotubes, Topics Appl. Phys **80**: 287–327.

Bahrami, A. H., et al. (2012). "Tubulation and Aggregation of Spherical Nanoparticles Adsorbed on Vesicles." Physical Review Letters **109**(18).

Becalska, A. N., et al. (2013). "Formation of membrane ridges and scallops by the F-BAR protein Nervous Wreck." Mol Biol Cell **24**(15): 2406-2418.

Bowick, M. J., et al. (2000). "Interacting topological defects on frozen topographies." Physical Review B **62**(13): 8738-8751.

Brangwynne, C. P., et al. (2006). "Microtubules can bear enhanced compressive loads in living cells because of lateral reinforcement." J Cell Biol **173**(5): 733-741.

Cahn, J. W. (1969). "The Metastable Liquidus and Its Effect on the Crystallization of Glass." Journal of the American Ceramic Society **52**(3): 118-121.

Camerino, D. C., et al. (2007). "Ion channel pharmacology." Neurotherapeutics **4**(2): 184-198.

Champion, J. A. and S. Mitragotri (2006). "Role of target geometry in phagocytosis." Proc Natl Acad Sci U S A **103**(13): 4930-4934.

Chan, H.-K. (2011). "Densest columnar structures of hard spheres from sequential deposition." Physical Review E **84**(5).

Chang, T. and H. Gao (2003). "Size-dependent elastic properties of a single-walled carbon nanotube via a molecular mechanics model." Journal of the Mechanics and Physics of Solids **51**(6): 1059-1074.

Chaudhuri, A., et al. (2011). "The effect of interactions on the cellular uptake of nanoparticles." Phys Biol **8**(4): 046002.

Chen, X., et al. (2013). "Internalization pathways of nanoparticles and their interaction with a vesicle." Soft Matter **9**(31): 7592.

de Pablo, P. J., et al. (2003). "Deformation and Collapse of Microtubules on the Nanometer Scale." Physical Review Letters **91**(9): 098101.

Deriu, M. A., et al. (2007). "Tubulin: from atomistic structure to supramolecular mechanical properties." Journal of Materials Science **42**(21): 8864-8872.

Deserno, M. (2004). "Elastic deformation of a fluid membrane upon colloid binding." Physical Review E **69**(3).

Deserno, M. (2004). "When do fluid membranes engulf sticky colloids?" Journal of Physics: Condensed Matter **16**(22): S2061-S2070.

Deserno, M. and W. M. Gelbart (2002). "Adhesion and Wrapping in Colloid−Vesicle Complexes." The Journal of Physical Chemistry B **106**(21): 5543-5552.

Elbaum, M., et al. (1996). "Buckling Microtubules in Vesicles." Physical Review Letters **76**(21): 4078-4081.

Erickson, R. O. (1973). "Tubular packing of spheres in biological fine structure." Science **181**(4101): 705-716.

Farsad, K., et al. (2001). "Generation of high curvature membranes mediated by direct endophilin bilayer interactions." J Cell Biol **155**(2): 193-200.

Frese, R. N., et al. (2008). "Protein shape and crowding drive domain formation and curvature in biological membranes." Biophys J **94**(2): 640-647.

Frost, A., et al. (2009). "The BAR Domain Superfamily: Membrane-Molding Macromolecules." Cell **137**(2): 191-196.

Goga, N., et al. (2012). "Efficient Algorithms for Langevin and DPD Dynamics." Journal of Chemical Theory and Computation **8**(10): 3637-3649.

Govindjee, S. and J. L. Sackman (1999). "On the use of continuum mechanics to estimate the properties of nanotubes." Solid State Communications **110**(4): 227-230.

Haiss, W., et al. (2007). "Determination of Size and Concentration of Gold Nanoparticles from UV−Vis Spectra." Analytical Chemistry **79**(11): 4215-4221.

Harris, W. F. and R. O. Erickson (1980). "Tubular arrays of spheres: geometry, continuous and discontinuous contraction, and the role of moving dislocations." J Theor Biol **83**(2): 215-246.

Haw, M. D. (2010). "Growth kinetics of colloidal chains and labyrinths." Physical Review E **81**(3): 031402.

Hayden, S. C., et al. (2012). "Aggregation and interaction of cationic nanoparticles on bacterial surfaces." J Am Chem Soc **134**(16): 6920-6923.

Henne, W. M., et al. (2007). "Structure and analysis of FCHo2 F-BAR domain: a dimerizing and membrane recruitment module that effects membrane curvature." Structure **15**(7): 839-852.

Hernández, E., et al. (1999). "Elastic properties of single-wall nanotubes." Applied Physics A **68**(3): 287-292.

Herold, C., et al. (2012). "Efficient electroformation of supergiant unilamellar vesicles containing cationic lipids on ITO-coated electrodes." Langmuir **28**(13): 5518-5521.

Hutchison, J. B., et al. (2016). "Osmotically-induced tension and the binding of N-BAR protein to lipid vesicles." Soft Matter **12**(8): 2465-2472.

Hutchison, J. B., et al. (2012). "Change of line tension in phase-separated vesicles upon protein binding." Langmuir **28**(11): 5176-5181.

Jain, P. K., et al. (2006). "Calculated Absorption and Scattering Properties of Gold Nanoparticles of Different Size, Shape, and Composition: Applications in Biological Imaging and Biomedicine." The Journal of Physical Chemistry B **110**(14): 7238-7248.

Jiang, L., et al. (2002). "Potential of mean force for protein–protein interaction studies." Proteins: Structure, Function, and Bioinformatics **46**(2): 190-196.

Jiang, L. and W. Guo (2011). "A molecular mechanics study on size-dependent elastic properties of single-walled boron nitride nanotubes." Journal of the Mechanics and Physics of Solids **59**(6): 1204-1213.

Khlobystov, A. N., et al. (2005). "Molecules in Carbon Nanotubes." Accounts of Chemical Research **38**(12): 901-909.

Kikkawa, M., et al. (1994). "Direct visualization of the microtubule lattice seam both in vitro and in vivo." J Cell Biol **127**(6 Pt 2): 1965-1971.

Kikumoto, M., et al. (2006). "Flexural Rigidity of Individual Microtubules Measured by a Buckling Force with Optical Traps." Biophys J **90**(5): 1687-1696.

Kis, A., et al. (2002). "Nanomechanics of Microtubules." Physical Review Letters **89**(24): 248101.

Klug, A. (1999). "The tobacco mosaic virus particle: structure and assembly." Philos Trans R Soc Lond B Biol Sci **354**(1383): 531-535.

Kohlstedt, K. L., et al. (2009). "Electrostatics and optimal arrangement of ionic triangular lattices confined to cylindrical fibers." Physical Review E **80**(5): 051503.

Kohlstedt, K. L., et al. (2009). "Surface patterning of low-dimensional systems: the chirality of charged fibres." J Phys Condens Matter **21**(42): 424114.

Koltover, I., et al. (1999). "Membrane Mediated Attraction and Ordered Aggregation of Colloidal Particles Bound to Giant Phospholipid Vesicles." Physical Review Letters **82**(9): 1991-1994.

Landau, L. D., et al. (1986). Theory of elasticity. Oxford Oxfordshire ; New York, Pergamon Press.

Le, M.-Q. (2014). "Prediction of Young's modulus of hexagonal monolayer sheets based on molecular mechanics." International Journal of Mechanics and Materials in Design **11**(1): 15-24.

Li, C. and T.-W. Chou (2003). "A structural mechanics approach for the analysis of carbon nanotubes." International Journal of Solids and Structures **40**(10): 2487-2499.

Li, S. and N. Malmstadt (2013). "Deformation and poration of lipid bilayer membranes by cationic nanoparticles." Soft Matter **9**(20): 4969.

Liu, L., et al. (2011). "Loop formation of microtubules during gliding at high density." J Phys Condens Matter **23**(37): 374104.

Lohr, M. A., et al. (2010). "Helical packings and phase transformations of soft spheres in cylinders." Physical Review E **81**(4): 040401.

Luque, A. and D. Reguera (2010). "The structure of elongated viral capsids." Biophys J **98**(12): 2993-3003.

Margolin, G., et al. (2012). "The mechanisms of microtubule catastrophe and rescue: implications from analysis of a dimer-scale computational model." Mol Biol Cell **23**(4): 642-656.

Marsh, D. (2006). "Elastic curvature constants of lipid monolayers and bilayers." Chem Phys Lipids **144**(2): 146-159.

Matthews, R. and C. N. Likos (2012). "Influence of Fluctuating Membranes on Self-Assembly of Patchy Colloids." Physical Review Letters **109**(17).

Mattila, P. K., et al. (2007). "Missing-in-metastasis and IRSp53 deform PI(4,5)P2-rich membranes by an inverse BAR domain-like mechanism." J Cell Biol **176**(7): 953-964.

Mellor, H. (2010). "The role of formins in filopodia formation." Biochimica et Biophysica Acta (BBA) - Molecular Cell Research **1803**(2): 191-200.

Molodtsov, M. I., et al. (2005). "A molecular-mechanical model of the microtubule." Biophys J **88**(5): 3167-3179.

Mughal, A., et al. (2011). "Phyllotactic Description of Hard Sphere Packing in Cylindrical Channels." Physical Review Letters **106**(11).

Mughal, A., et al. (2012). "Dense packings of spheres in cylinders: Simulations." Physical Review E **85**(5).

Mui, B., et al. (2003). Extrusion Technique to Generate Liposomes of Defined Size. Methods in Enzymology, Academic Press. **Volume 367:** 3-14.

Müller, M. M., et al. (2005). "Geometry of surface-mediated interactions." Europhysics Letters (EPL) **69**(3): 482-488.

Needham, D. and D. Zhelev (2007). Use of Micropipet Manipulation Techniques to Measure the Properties of Giant Lipid Vesicles. Perspectives in Supramolecular Chemistry, John Wiley & Sons, Ltd.**:** 102-147.

Oğuz, E. C., et al. (2011). "Helicity in cylindrically confined Yukawa systems." EPL (Europhysics Letters) **94**(2): 28005.

Paasonen, L., et al. (2007). "Gold nanoparticles enable selective light-induced contents release from liposomes." J Control Release **122**(1): 86-93.

Pickett, G. T., et al. (2000). "Spontaneous Chirality in Simple Systems." Physical Review Letters **85**(17): 3652-3655.

Pilhofer, M., et al. (2011). "Microtubules in Bacteria: Ancient Tubulins Build a Five-Protofilament Homolog of the Eukaryotic Cytoskeleton." PLOS Biology **9**(12): e1001213.

Plimpton, S. (1995). "Fast Parallel Algorithms for Short-Range Molecular Dynamics." Journal of Computational Physics **117**(1): 1-19.

Prusinkiewicz, P. and A. Lindenmayer (1990). The Algorithmic Beauty of Plants. The Algorithmic Beauty of Plants, Springer**:** 109-118.

Rafiee, R. and R. Pourazizi (2014). "Evaluating the influence of defects on the young's modulus of carbon nanotubes using stochastic modeling." Materials Research **17**: 758-766.

Ramos, L. (1999). "Surfactant-Mediated Two-Dimensional Crystallization of Colloidal Crystals." Science **286**(5448): 2325-2328.

Reddy, A. S., et al. (2012). "Effect of membrane tension on the physical properties of DOPC lipid bilayer membrane." Biochim Biophys Acta **1818**(9): 2271-2281.

Rein ten Wolde, P. and D. Frenkel (1999). "Homogeneous nucleation and the Ostwald step rule." Physical Chemistry Chemical Physics **1**(9): 2191-2196.

Reynwar, B. J. and M. Deserno (2011). "Membrane-mediated interactions between circular particles in the strongly curved regime." Soft Matter **7**(18): 8567.

Reynwar, B. J., et al. (2007). "Aggregation and vesiculation of membrane proteins by curvature-mediated interactions." Nature **447**(7143): 461-464.

Rodriguez, N., et al. (2005). "Giant vesicles formed by gentle hydration and electroformation: a comparison by fluorescence microscopy." Colloids Surf B Biointerfaces **42**(2): 125-130.

Ruiz-Herrero, T., et al. (2012). "Mechanisms of budding of nanoscale particles through lipid bilayers." J Phys Chem B **116**(32): 9595-9603.

Sachse, C., et al. (2007). "High-resolution Electron Microscopy of Helical Specimens: A Fresh Look at Tobacco Mosaic Virus." Journal of Molecular Biology **371**(3): 812-835.

Sandre, O., et al. (1999). "Dynamics of transient pores in stretched vesicles." Proceedings of the National Academy of Sciences **96**(19): 10591-10596.

Šarić, A. and A. Cacciuto (2011). "Particle self-assembly on soft elastic shells." Soft Matter **7**(5): 1874.

Šarić, A. and A. Cacciuto (2012). "Fluid Membranes Can Drive Linear Aggregation of Adsorbed Spherical Nanoparticles." Physical Review Letters **108**(11).

Šarić, A. and A. Cacciuto (2013). "Self-assembly of nanoparticles adsorbed on fluid and elastic membranes." Soft Matter **9**(29): 6677.

Schaap, I. A. T., et al. (2006). "Elastic Response, Buckling, and Instability of Microtubules under Radial Indentation." Biophys J **91**(4): 1521-1531.

Scholfield, C. R. (1981). "Composition of soybean lecithin." Journal of the American Oil Chemists Society **58**(10): 889-892.

Sear, R. P., et al. (1999). "Spontaneous patterning of quantum dots at the air-water interface." Physical Review E **59**(6): R6255-R6258.

Sept, D. and F. C. MacKintosh (2010). "Microtubule Elasticity: Connecting All-Atom Simulations with Continuum Mechanics." Physical Review Letters **104**(1).

Solis, F. J., et al. (2011). "Electrostatic-driven pattern formation in fibers, nanotubes and pores." Soft Matter **7**(4): 1456.

Srebnik, S. and J. F. Douglas (2011). "Self-assembly of charged particles on nanotubes and the emergence of particle rings, chains, ribbons and chiral sheets." Soft Matter **7**(15): 6897.

Su, Y.-C. and J. Z. Y. Chen (2015). "A model of vesicle tubulation and pearling induced by adsorbing particles." Soft Matter **11**(20): 4054-4060.

Sui, H. and K. H. Downing "Structural Basis of Interprotofilament Interaction and Lateral Deformation of Microtubules." Structure **18**(8): 1022-1031.

Tanur, A. E., et al. (2013). "Diameter-dependent bending modulus of individual multiwall boron nitride nanotubes." J Phys Chem B **117**(16): 4618-4625.

Tian, F., et al. (2010). "Curvature modulates the self-assembly of amphiphilic molecules." J Chem Phys **133**(14): 144701.

Tristram-Nagle, S. and J. F. Nagle (2004). "Lipid bilayers: thermodynamics, structure, fluctuations, and interactions." Chem Phys Lipids **127**(1): 3-14.

van Meer, G., et al. (2008). "Membrane lipids: where they are and how they behave." Nature reviews. Molecular cell biology **9**(2): 112-124.

Vanapalli, S. A., et al. (2008). "Fluidic Assembly and Packing of Microspheres in Confined Channels." Langmuir **24**(7): 3661-3670.

VanBuren, V., et al. (2005). "Mechanochemical Model of Microtubule Structure and Self-Assembly Kinetics." Biophys J **89**(5): 2911-2926.

Wang, B., et al. (2008). "Nanoparticle-induced surface reconstruction of phospholipid membranes." Proc Natl Acad Sci U S A **105**(47): 18171-18175.

Wood, D. A., et al. (2013). "Self-assembly on a cylinder: a model system for understanding the constraint of commensurability." Soft Matter **9**(42): 10016.

Xiao, J. R., et al. (2005). "An analytical molecular structural mechanics model for the mechanical properties of carbon nanotubes." International Journal of Solids and Structures **42**(11-12): 3075-3092.

Xu, A., et al. (2012). "A physical model for the size-dependent cellular uptake of nanoparticles modified with cationic surfactants." Int J Nanomedicine **7**: 3547-3554.

Yi, X., et al. (2011). "Cellular Uptake of Elastic Nanoparticles." Physical Review Letters **107**(9).

Yu, Y. and S. Granick (2009). "Pearling of lipid vesicles induced by nanoparticles." J Am Chem Soc **131**(40): 14158-14159.

Zhang, Y., et al. (2012). "Permission to enter cell by shape: nanodisk vs nanosphere." ACS Appl Mater Interfaces **4**(8): 4099-4105.

Zimmerberg, J. and M. M. Kozlov (2006). "How proteins produce cellular membrane curvature." Nat Rev Mol Cell Biol **7**(1): 9-19.